Dynamics and Magnetic Field Generation in Jupiter and Saturn

Von der Fakultät für Elektrotechnik, Informationstechnik, Physik
der Technischen Universität Carolo-Wilhelmina
zu Braunschweig
zur Erlangung des Grades einer
Doktorin der Naturwissenschaften
(Dr.rer.nat.)
genehmigte
Dissertation

von Lúcia Dias de Vasconcelos Duarte
aus Viseu, Portugal

Bibliografische Information der Deutschen Nationalbibliothek

Die Deutsche Nationalbibliothek verzeichnet diese Publikation in der Deutschen Nationalbibliografie; detaillierte bibliografische Daten sind im Internet über `http://dnb.d-nb.de` abrufbar.

1. Referentin oder Referent: Prof. Dr. Karl-Heinz Glaßmeier
2. Referentin oder Referent: Prof. Dr. Andreas Hördt

eingereicht am: 19 Dezember 2013
mündliche Prüfung (Disputation) am: 7 Februar 2014

ISBN 978-3-942171-79-3

uni-edition GmbH 2014
http://www.uni-edition.de

Printed in Germany

Vorveröffentlichungen der Dissertation

Teilergebnisse aus dieser Arbeit wurden mit Genehmigung der Fakultät für Elektrotechnik, Informationstechnik, Physik, vertreten durch die Mentorin oder den Mentor/die Betreuerin oder den Betreuer der Arbeit, in folgenden Beiträgen vorab veröffentlicht:

Publikationen

First author

- Duarte, L. D. V., Gastine, T., Wicht, J., 2012, Anelastic dynamo models with variable electrical conductivity: an application to gas giants. Physics of the Earth and Planetary Interiors 222, 22-34.

Co-author

- Gastine, T., Duarte, L., Wicht, J., 2012, Dipolar versus multipolar dynamos: the influence of the background density stratification. Astronomy & Astrophysics 546, A19.

- Gastine, T., Morin, J., Duarte, L., Reiners, A., Christensen, U. R., Wicht, J., 2013, What controls the magnetic geometry of M dwarfs? Astronomy & Astrophysics 549, L5.

- Morin, J., Gastine, T., Duarte, L., Reiners, A., Christensen, U. R., Wicht, J., 2012, Does inertia determine the magnetic geometry of low-mass stars? SF2A-2012, 415-418.

- Yadav, R. K., Gastine, T., Christensen U. R., Duarte, L. D. V., 2013, Consistent scaling laws in anelastic spherical shell dynamos. Astronomy & Astrophysics 774-779.

Tagungsbeiträge

- AGU Fall Meeting, "Magnetic Field Generation and Zonal Flows in the Gas Giants" (poster), 9–13th December 2013, San Francisco, USA

- Nordita workshop, Differential Rotation and Magnetism across the HR Diagram, "Anelastic dynamo models with variable electrical conductivity: an application to gas giants" (talk), 19th April – 3rd May 2013, Stockholm, Sweden
- IMPRS Seminar, "Anelastic dynamo models with variable electrical conductivity: an application to gas giants" (talk), 19th December 2012, Katlenburg-Lindau, Germany
- AGU Fall Meeting, "Anelastic dynamo models with radially varying conductivity applied to the gas giants" (poster), 3rd–7th December 2012, San Francisco, USA
- 3rd PlanetMag Meeting, "Dynamo models with radially varying conductivity: application to the gas giants" (talk), 24–25th September 2012, Rostock, Germany
- SEDI meeting 2012, "Anelastic dynamo models with radially varying conductivity, an application to the gas giants" (poster), 1st–6th July 2012, Leeds, United Kingdom
- IMPRS Seminar, "Towards more realistic dynamo models of the Gas Giants" (talk), 2nd March 2012, Katlenburg-Lindau, Germany
- AGU Fall Meeting, "Anelastic Dynamo Model with Radially Varying Conductivity - an Application to the Gas Giants" (talk), 5–9th December 2011, San Francisco, USA
- 2nd PlanetMag Meeting, "Anelastic Dynamo Models with Radially Varying Conductivity - an Application to the Gas Giants" (talk), 18th–21st October 2011, Wernigerode, Germany
- Dynamo iGdR meeting, "Anelastic dynamo models with radially varying conductivity - An application to the Gas Giants" (poster), 12–17th September 2011, Cargèse, France
- IMPRS Seminar, "Explaining the simplicity of Saturn's magnetic field" (talk), 2nd March 2011, Katlenburg-Lindau, Germany
- 1st PlanetMag Meeting, "Dynamics and Magnetic Field Generation in Saturn" (poster), 19th–21st January 2011, Tutzing, Germany

Contents

Abstract

The observed surface dynamics of Jupiter and Saturn is dominated by a banded system of fierce zonal winds. The depth of these winds remains unclear but they are thought to be confined to the very outer envelope where hydrogen remains molecular and the electrical conductivity is small. The dynamos maintaining the dipole-dominated magnetic fields of both gas giants, on the other hand, likely operate in the deeper interior where hydrogen assumes a metallic state and the electrical conductivity is therefore high.

Previous models have neglected the density gradient across the metallic layer, which is much smaller than in the outer envelope but still sizeable. To explore the possible effects of stratification, the numerical MHD code MagIC was used. A systematic parameter study shows that dipole-dominated dynamos are rather rare when stronger stratifications are assumed along with stress-free outer boundaries appropriated for modelling gas envelopes. For the larger density stratifications, no dipole-dominated solutions are found. This is attributed to the fact that the focus of convective action moves progressively outward in cylindrical radius when the stratification is intensified. Once the convective columns are mainly confined to a relatively thin outer shell, a non-axisymmetric dynamo mode is preferred that has previously only been observed in mean-field dynamo simulations. This type of dynamo may be referred to as a thin-shell dynamo.

Independently of the density stratification, non-dipole-dominated or multipolar fields are typically weak and allow strong zonal flows to develop. These flows are predominantly axisymmetric and maintained by Reynolds stresses. Thus all jets tend to be geostrophic and therefore reach right through the convective shell. The simulations show that stable dipolar fields and strong zonal flows are mutually exclusive, with solutions either having strong zonal winds and multipolar magnetic fields or weak zonal winds and dipole-dominated magnetic fields.

In the second part of this work, numerical simulations are presented that attempt to model both the zonal winds and the interior dynamo action in an integrated approach, exploring the effects of density stratification and radial electrical conductivity variation simultaneously. The electrical conductivity is mostly assumed to remain constant in the thicker inner metallic region and it decays exponentially towards the outer boundary throughout the molecular envelope.

The results show that the combination of a stronger density stratification and a weaker conducting outer layer is essential for reconciling dipole-dominated dynamo action and a fierce equatorial zonal jet. The particular setup explored here allows a strong equatorial jet to remain confined to the weaker conducting outer region where it does not interfere with the deeper-seated dynamo action. The flanking mid to high latitude jets, on the other hand, have to remain faint to yield a strongly dipolar magnetic field. The fiercer jets on Jupiter and Saturn only seem compatible with the observed dipolar fields when they remain confined to a weaker conducting outer layer.

Some parameters used in numerical simulations are, in general, orders of magnitude away from planetary values. Nonetheless, these simulations are quite successful in reproducing qualitatively the observed features. This suggests that the models operate in the "correct regime" and consistent scaling laws allow to extrapolate magnetic and velocity fields to the planetary situation. The data obtained here was subject to such laws, with an outcome similar to what was previously obtained by other authors. When applying these laws to the new simulation results, the values fall within an acceptable range from the observations.

1 Introduction

1.1 Giant Planets

The outer planets of the Solar System, also known as the four giant planets, differ from the inner four planets not only in size, but also in composition and little is certain about the interior structure of the four giants. The two giant planets closest to the Sun, Jupiter and Saturn (the gas giants), are thought to have a relatively similar structure, being mainly composed of hydrogen and helium, the most abundant element in the protosolar nebula. Quantities like mass, mean radius and gravitational moments provide constraints to the interior structure of these planets and they were first measured by the spacecrafts Pioneer and Voyager in the 70s. In the 90s, the Galileo orbiter was, however, the first to orbit Jupiter and gather data of the Jovian system, whereas its atmospheric entry probe obtained information of the top cloud layer of the planet, down to the 23-bar level (~ 153°C at 150 km below the surface), including important clues about the interior dynamics.

The chemical structure of the gas planets is determined by surface measurements and comparison of these with the solar composition, thought to be an indication of the protosolar nebula's ingredients. For example, it is known that the fraction of helium on the surface of both Jupiter and Saturn is lower than the solar values (lower in Saturn than in Jupiter), which suggests a higher concentration of this element in the deep interior of the planets. Yet the dominating element is hydrogen and the knowledge of its behaviour at high pressure/temperature is a key to understanding the interior.

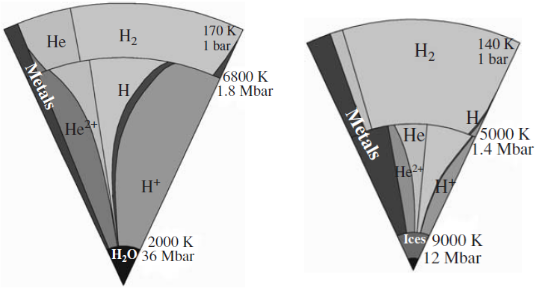

Figure 1.1: Chemical structure of an interior three-layer model for Jupiter (left) and for Saturn (right). The images were taken from Nettelmann et al. (2008b).

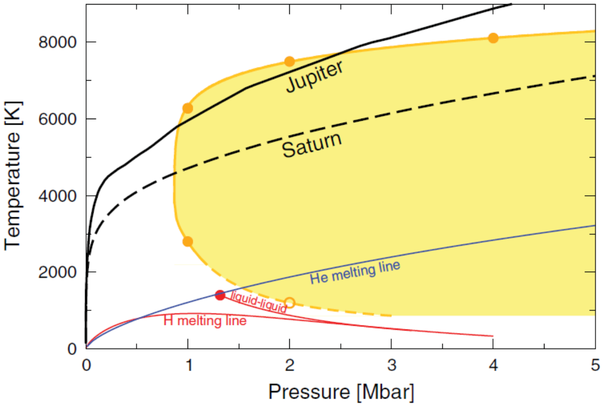

Figure 1.2: Demixing region of hydrogen and helium in the phase diagram. The solid and dashed lines represent the adiabats of Jupiter (Nettelmann et al. 2008a) and Saturn, respectively. The red lines correspond to the phase diagram of hydrogen (Morales et al. 2010, Lorenzen et al. 2010), shown in more detail in Fig. 1.8 of the next section, and the blue line is the melting line of helium (Lorenzen et al. 2009). The image was adapted from Lorenzen et al. (2011).

A strong hypothesis to solve the inconsistency of the absence of helium in the atmospheres of the two gas giants, compared to protosolar values, is a H-He phase separation in the interior of the planets, first suggested by Stevenson (1982). A possible discontinuity between helium-rich and helium-poor layers is the basic assumption for the three-layer interior models of the gas giants (Fig. 1.1), where the third layer is the small rocky inner core (Guillot 2005, Fortney et al. 2010, Lorenzen et al. 2011, French et al. 2012). For Jupiter this discontinuity is much smaller than Saturn's, as the phase diagram of Fig. 1.2 from the studies of Lorenzen et al. (2009, 2011) shows from the crossing of the planets' adiabats through the area of H-He demixing (yellow).

For Saturn, but also for Jupiter, the helium concentration in the interior of both planets is a topic still under investigation (Fortney and Hubbard 2003, 2004, Fortney and Nettelmann 2010). Observations by Galileo and, more recently, Cassini showed a significant depletion of helium in Saturn's and Jupiter's atmospheres, though much less accentuated in the latter. Thermal chemically fully convective evolution models that assume an adiabat are closely consistent with Jupiter's observed heat flow, but such models applied to Saturn show much faster evolution than in reality, i.e. they bring the surface temperature to lower values than observed. Going back to the question about the helium deficit in the atmospheres of the gas giants, helium is extremely difficult to ionize and metallize, which is estimated to happen only around pressures of $20-100\,\mathrm{Mbar}$. Consequently, the He metallization line is out of the range of Fig. 1.2 (see also Stevenson and Salpeter 1977b). Even though helium is miscible with molecular hydrogen, its miscibility is limited in metallic hydrogen. The immiscilibity (or demixing) process happens when, in a certain mixture of hydrogen and helium in the interior of a gas giant (solar abundances

$x_H = 0.736$ and $x_{He} = 0.249$, Fortney and Hubbard 2003), the two elements are not mixable below a critical temperature, so that helium condenses out of the hydrogen in small droplets (Salpeter 1973). Due to the higher density of the droplets in comparison with the surroundings, they condense, grow and gravity pulls them to greater depths in time scales assumed faster than convection, by Stevenson and Salpeter (1977a). Thus demixing is possible in a convective system. Salpeter (1973), Stevenson and Salpeter (1977b) were the first to suggest that the demixing happens in the metallic hydrogen layer, below the molecular-metallic transition. Lorenzen et al. (2009, 2011) concluded that the phase transition (metallization) of hydrogen drives the demixing, at least till the temperature is high enough to favour a mixed state again. This is questionable to happen or not in Jupiter's interior, since only part of the isentrope lies inside the demixing region (Fig. 1.2), while it is expected to happen in most of Saturn's interior, since its adiabat is almost entirely in the demixing region. Furthermore, Jupiter's thermal evolution is fairly well reproduced by an homogeneous model.

Both gas giants, Jupiter and Saturn, emit considerable more energy than they receive from the Sun. The heat flux released from their interiors can be explained with the presence of a fluid convective interior at high temperature. This may be in conflict with an inhomogeneous region where the helium concentration increases with depth, since such region may inhibit convection altogether. In this work, a fully convective interior is considered, though this is an uncertainty for Saturn (Christensen and Wicht 2008, Stanley 2010). Nonetheless, the target of this thesis is to study models without this assumption. Due to the convective motions and consequent mixing in the interior, the hydrogen layers of Jupiter (the inner metallic layer and the outer molecular envelope) are assumed to have a homogeneous composition.

To summarize, in models of planetary evolution of the gas giants, an adiabat and homogeneous interior undergoing convection is not sufficient to explain their present observed effective temperatures (the observed temperatures are much higher, Fortney and Hubbard 2003). Helium sedimentation, is probably the most accepted solution, as gravitational energy is released and transformed into heat. Furthermore, the existence of a layer stable to convection can slow down the cooling of the planets, since energy travels across it either by diffusion or by instabilities that are poorly understood, both much slower processes than convection. This issue concerns both Jupiter and Saturn, but while Saturn emits around 50% more energy than the initial homogeneous models dictated, Jupiter's thermal evolution is fairly well reproduced, thus the helium sedimentation is not taken into account in this thesis.

Hydrogen is a diatomic insulator molecule at low pressure, but shock wave experiments revealed that beyond the threshold of $\sim 100\,\mathrm{GPa}$, dissociated and ionized hydrogen forms a metal. No discontinuities in the liquid-liquid phase transition of hydrogen were detected at the ranges of temperature and pressure of Jupiter and Saturn's interiors, which is also a feature of the recent numerical models from Nettelmann et al. (2012) and French et al. (2012), though such discontinuity exists at lower temperatures (see Fig. 1.8 and next section). This is shown in the findings of Lorenzen et al. (2011) in Fig. 1.3. According to the models of Fig. 1.1, the pressures at the "boundary" between the outer molecular envelope and the inner metallic region are around 1.8 Mbar for Jupiter and 1.4 Mbar for Saturn, thus both in the range $1-2$ Mbar. In Fig. 1.3, the diamonds are the closest value to the helium fraction of the protosolar nebula $x_{He} = 0.249$. The two corresponding lines of

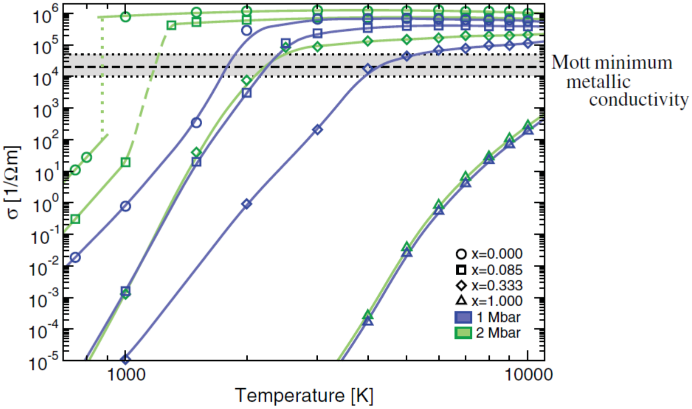

Figure 1.3: Electrical conductivity for different fractions x of helium in H-He mixtures at two different pressures: 1 Mbar in blue and 2 Mbar in green. The grey area corresponds to a possible range of values for the minimum conductivity of a metallic mixture, where the central dashed line is the value obtained by Mott at $T = 0$ K. This area serves to distinguish the metallic behaviour of the H-He mixture from the non-metallic (Lorenzen et al. 2011). The image was adapted from Lorenzen et al. (2011).

pressures 1 Mbar (blue) and 2 Mbar (green) show indeed no discontinuity when crossing the suggested area of transition between the metallic and the non-metallic behaviour of the H-He mixture (Lorenzen et al. 2011). Models such as the ones displayed in Fig. 1.1 provide also consistent information about the gradient of the fluid transport properties with radius, from the centre to the 1-bar pressure level, typically assumed as the surface of a giant planet. This was done for the first time by French et al. (2012) for Jupiter.

The size of the rocky inner core of the gas giants is still poorly constrained today. Saturn is very likely to have one, but this remains uncertain for Jupiter. The inner core of the latter is smaller, if it exists at all, since it is not essential to match the observed gravitational moments J_n (Nettelmann et al. 2008a).The existence of a central core is however preferred, as a high enrichment of heavy-elements and an extreme equation of state would be required otherwise (Guillot 1999). Moreover, in a Solar System formation scenario, the gas giants form by accreting material around a rocky core, which can undergo erosion later on.

To finish this short review on giant planets, it is necessary to briefly talk about the two outer planets as well, known as the ice giants of the Solar System, Uranus and Neptune. Both planets are assumed to have a more complex interior structure than the gas giants. The observed abundance of hydrogen and helium detected in their atmospheres is close to the protosolar values, with trace amounts of heavier elements, mainly CH_4 and possibly NH_3 (Hubbard and Macfarlane 1980, Hubbard et al. 1995). Moreover, both planets have approximately the same mass, but Neptune is denser than Uranus, which can be either due to a larger compression or different composition. To match the poorly constrained

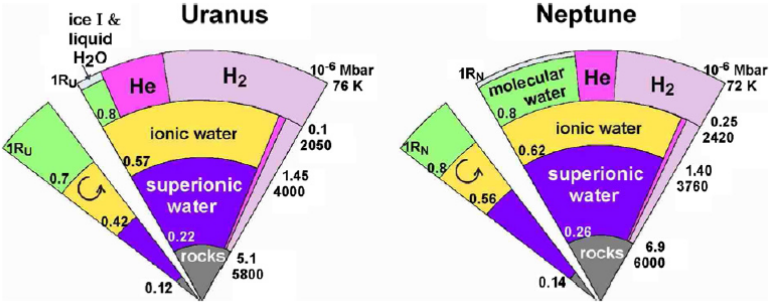

Figure 1.4: Chemical structure of interior models for Uranus (left) and Neptune (right). The images were taken from Redmer et al. (2011).

gravitational moments of the ice giants, the density profiles required are close to the one of ice for most of the bulk, excluding the very outer part which should have a density similar to a mixture of hydrogen and helium. Thus the main constituent in the form of ices of the interior of the ice giants is expected to be H_2O (Redmer et al. 2011), not detected in their atmospheres due to its low vapour pressure (Hubbard et al. 1995), and also CH_4 and NH_3.

A simple three-layer and mostly homogeneous model for Uranus does not reproduce its gravitational moments. This suggests an inhomogeneous interior that could also explain the small heat flux being released from the planet, as it would not be allowed to efficiently escape from the whole interior through convective motions. Instead, the heat would only be able to diffuse or be transferred by other instabilities through possible stably stratified layers, where the molecular weight gradient is high. In Neptune, these stable layers may also be present, but at greater depth, thus allowing faster transport of heat outward.

Redmer et al. (2011) derived interior models based on *ab initio* equations for hydrogen, helium and water, where water was used to represent the heavy elements. At high pressure, the water molecule dissociates along with the increase of electrical conductivity, into the ionic phase. As Redmer et al. (2011) show in Fig. 1.5, beyond pressures of 1.0 Mbar, the ice phases occur only below a temperature of 2500 K, above which water assumes a superionic state consisting of an oxygen lattice where protons can move freely as a conducting fluid. It is then in a thin layer confined between the outer molecular layer and the superionic region (see Fig. 1.4) that convection is most expected to take place and a dynamo would be generated. The role and properties of the superionic layer in this process are still poorly understood.

All four giant planets have distinct magnetic fields. As Fig. 1.6 shows, the gas giants exhibit dipolar fields, while the ice giants' magnetic fields are clearly non-dipolar. Jupiter's field in particular will be discussed in section 1.3. Saturn's field is remarkably axisymmetric, possibly due to a significant stable layer in its interior, formed in the helium density gradient on top of the dynamo region due to the helium sedimentation that depletes this part and enriches the deeper interior with helium. Such a stably stratified

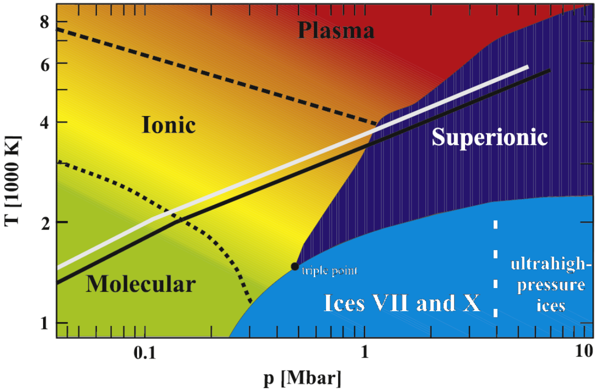

Figure 1.5: Phase diagram of water at high pressures. The two solid lines are the isentropes of Uranus (white) and Neptune (black). The dotted and dashed lines indicate continuous transitions due to dissociation and ionization, respectively. The image was adapted from Redmer et al. (2011).

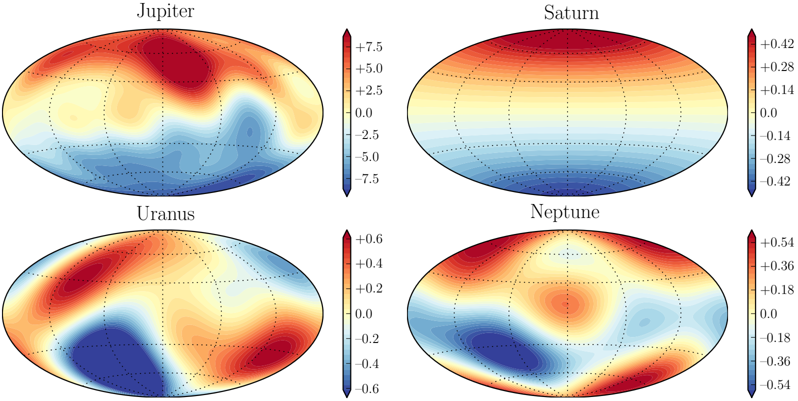

Figure 1.6: Surface maps of the radial component of the magnetic field of the four giant planets (see section 1.3 and Eq. 1.1 on how to determine). The origin of the data is: Jupiter up to $\ell = 7$ from Ridley (2013), Saturn up to $\ell = 5$ from Cao et al. (2012), Uranus and Neptune up to $\ell = 3$ from Holme and Bloxham (1996). The magnetic field values in the colorbars are given in Gauss.

layer is capable of filtering out the non-axisymmetric components, since these have a certain frequency related to the predominantly toroidal motion inside a stable layer. This corresponds to a magnetic skin effect due to electromagnetic induction, where the time-varying magnetic field induces a time-varying electric current which in turn generates another magnetic and electric fields with opposite directions. Thus the magnetic flux decreases exponentially through the stably-stratified layer and the exponential decay is faster for higher frequencies (higher non-axisymmetric modes). As Stevenson (1980) proposed, such layer would also explain the small tilt angle of the dipole in the order of 1° (Cao et al. 2012, alternative model of a spherical Couette dynamo). Recently, the upper bound of the tilt derived from data of the Cassini mission was found to be even smaller, less than 0.1° (Burton et al. 2010). However, models that include a stably stratified layer (Christensen and Wicht 2008, Stanley 2010) have not yet been successful to achieve a tilt of the dipole lower that 0.8°.

Little is known about the magnetic field of the ice giants Uranus and Neptune. Only up to the octupole components were measured so far, by Voyager 2 in the 80s. The degree spectrum of both planets is rather flat and the order spectrum shows a peak in the $m = 1$ mode. In addition, both planets have a very pronounced tilt of the dipolar component of the field, around 50°. Until now, few dynamo models reproduced these observed features: while Stanley and Bloxham (2004, 2006)’s models only reproduce the multipolar magnetic fields in strongly time-dependent multipolar fields, Aurnou et al. (2007) and Soderlund et al. (2013) model the dynamics of the atmosphere which includes a wide equatorial retrograde surface jet, flanked by two prograde jets at higher latitudes, in non-magnetic and magnetic simulations, respectively. The reason may still be the higher complexity of the interior structure of both planets and the uncertainty of where the dynamo action actually takes place.

1.2 Jupiter’s *ab initio* interior model

In the last years, there has been progress made not only with experiments, but also with models that solve *ab initio* equations numerically. The rapid improvement of computational resources has allowed the latter to be particularly effective in achieving regimes that high-pressure experiments have not been able to reach, namely the conditions inside the giant planets.

French et al. (2012) provide a complete study of the interior thermodynamic material and transport properties for Jupiter. Their calculations are done along Jupiter’s adiabat, assuming one of the interior models obtained by Nettelmann et al. (2012), which provides the boundary conditions of the model, such as mass of the core, mass fractions of heavy elements in the two outer envelopes, gravitational moments and the radius and pressure where the transition between the two layers takes place. The most relevant profiles for the present work are shown in Fig. 1.7. The radial density profile has a density decay across the conducting part (from $\sim 0.1\,\mathrm{R}_{♃}$ to $\sim 0.9\,\mathrm{R}_{♃}$, where $\mathrm{R}_{♃}$ is the radius of Jupiter, defined at the 1-bar pressure level) of one order of magnitude and an additional decrease of almost three orders of magnitude in the outer molecular envelope alone.

Morales et al. (2010) showed that a first order liquid-liquid (liquid H_2 – liquid H^+) transition for hydrogen happens for temperature below 2000 K (critical points in Fig. 1.8),

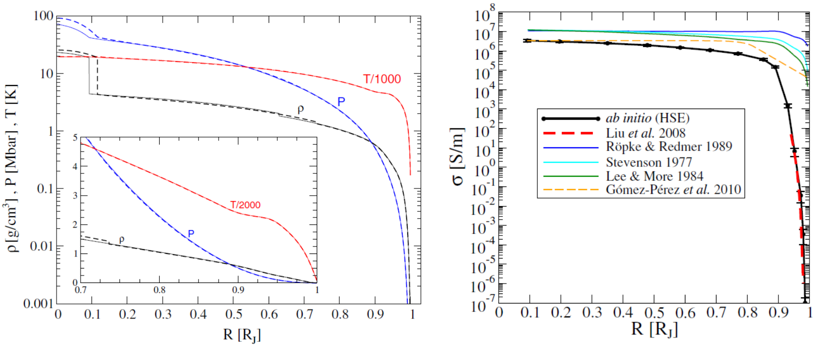

Figure 1.7: Radial profiles of density ρ, temperature T and pressure P on the left panel and electrical conductivity σ on the right panel. The profiles were adapted from French et al. (2012).

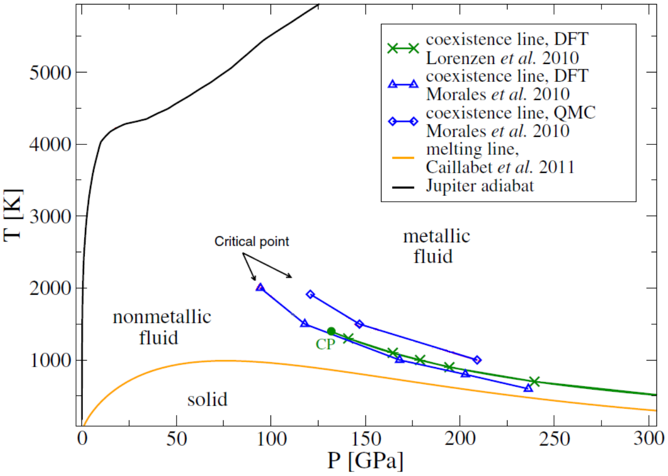

Figure 1.8: Phase diagram of hydrogen. The blue and green symbols/lines correspond to the first-order liquid-liquid transition (LLT). The melting curve is shown in orange and the remaining coloured symbols represent experimental measurements. The critical points are the upper limit for the first-order LLT transition, above which metallization becomes a continuous process with pressure. The image was adapted from French et al. (2012), with results from Morales et al. (2010) in blue, Lorenzen et al. (2010) in green and Caillabet et al. (2011) in orange.

but according to Jupiter's adiabat the metallization of hydrogen onsets around 4500 K, clearly beyond the critical point. This means that there is no first-order plasma phase transition in Jupiter and, instead, it is a continuous transition.

1.3 Jupiter's intrinsic magnetic field

Jupiter's magnetic field is very similar in morphology to the geomagnetic field since both are dipole-dominated with a dipole tilt around 10°. The strength of the field is around ten times larger than the Earth's, which allowed its existence to be discovered back in the 50s by the detection of radio emissions from energetic electrons trapped in its giant magnetosphere (Burke and Franklin 1955).

The magnetic field vector can be obtained at any distance from the dynamo region of the planet r by solving Gauss' law of magnetism that states that the magnetic induction is divergence-free, thus it can be expressed as a potential ($\mathbf{B} = -\nabla\Phi$, where $\Delta\Phi = 0$). In other words, the source of the magnetic field is internal and the magnitude of the potential is determined by the solutions of the Laplace equation of the potential, which are spherical harmonics where the coefficients are also called Gauss coefficients. Furthermore, the Schmidt-normalized Legendre polynomials P_ℓ^m are used, as (Lowes 1966, 1974, Barthelmes 2013)

$$
\begin{aligned}
B_\phi &= \frac{1}{\sin\theta}\sum_{\ell=1}^{\infty}\sum_{m=0}^{\ell}\left\{ m\,\frac{R_{♃}^{\ell+2}}{r}\left[g_\ell^m \sin(m\phi) - h_\ell^m \cos(m\phi)\right] P_\ell^m(\sin\theta)\right\},\\
B_\theta &= \sum_{\ell=1}^{\infty}\sum_{m=0}^{\ell}\left\{\left(\frac{R_{♃}}{r}\right)^{\ell+2}\left[g_\ell^m \cos(m\phi) + h_\ell^m \sin(m\phi)\right]\frac{dP_\ell^m(\sin\theta)}{d\theta}\right\},\\
B_r &= \sum_{\ell=1}^{\infty}\sum_{m=0}^{\ell}\left\{(\ell+1)\left(\frac{R_{♃}}{r}\right)^{\ell+2}\left[g_\ell^m \cos(m\phi) + h_\ell^m \sin(m\phi)\right] P_\ell^m(\sin\theta)\right\},
\end{aligned}
\tag{1.1}
$$

where $R_{♃} \approx 7\times10^7$ m is the radius of Jupiter, typically defined at the 1-bar pressure level. The spatial power spectra of the magnetic field is obtained from the mean square of the magnetic field produced by harmonics ℓ and m, thus the power spectrum R_ℓ (R_m) is a sum of all m (ℓ) contributions for each ℓ (m) and plotted against ℓ (m) (Lowes 1966, 1974),

$$
R(\ell, m, r) = (\ell+1)\left(\frac{R_{♃}}{r}\right)^{2\ell+4}\left[(g_\ell^m)^2 + (h_\ell^m)^2\right]. \tag{1.2}
$$

Tab. 1.1 shows the results of the most recent inversion models to determine the Gauss coefficients of the magnetic field of Jupiter. The second column shows a model based on data of the Galileo spacecraft which orbited the Jupiter system between 1995 and 2003 obtained by Yu et al. (2010). They compare their results with a previous model by NASA based on observations from Pioneer 11 in the mid 70s (O6 model, Connerney 1992) and they found a significant difference in the g_3^1 and h_3^1 coefficients from the Pioneer model, due to the fact that the Galileo measurements were obtained in the equatorial plane of rotation, hence the lack of resolution of g_2^0, g_3^1 and h_3^1. This was because the contribution of these modes is minimum at Galileo's orbit plane. Thereby, they used the g_3^1 and h_3^1 coefficients of NASA's Pioneer model (Tab. 1.1). The third column shows results obtained by Hess et al. (2011) from Voyager and Pioneer data instead, constrained by auroral emissions of Jupiter's moon Io, which allowed them to reach a higher resolution of $(\ell, m) = (5, 5)$. The fourth and fifth columns were inversions done by Ridley (2013) from all the available data to date, including the flyby of the Ulysses spacecraft in the early 90s, which provided the highest number of harmonics so far, of $(\ell, m) = (7, 7)$.

Table 1.1: Spherical harmonics coefficients from: an octupole model by Yu et al. (2010) derived from observations by the Galileo spacecraft (1995-2003) in the second column; a model based on data from the Voyager and Pioneer spacecrafts and constrained by Io's auroral emissions by Hess et al. (2011) in the third column; two models from Ridley (2013) based on all the available data, including the flyby of the Ulysses spacecraft, in the fourth and fifth columns.

g^{ℓ}_{m}, h^{ℓ}_{m}	model Yu et al. (2010)	model Hess et al. (2011)	JTA1 model Ridley (2013)	JTA2 model Ridley (2013)
g^1_0	4.273	4.2	4.0986	4.0943
g^1_1	−0.716	−0.6975	−0.6867	−0.6847
h^1_1	0.235	0.1973	0.2371	0.2375
g^2_0	0.270	0.6441	0.1040	0.0937
g^2_1	−0.593	−0.8672	−0.5711	−0.5758
g^2_2	0.523	0.9598	0.4912	0.4861
h^2_1	−0.442	−0.4041	−0.4480	−0.4538
h^2_2	0.157	0.603	0.1607	0.1581
g^3_0	−0.092	−0.1058	−0.0100	0.0028
g^3_1	−0.155	−0.59	−0.3685	−0.3355
g^3_2	0.274	0.6322	0.2262	0.1754
g^3_3	−0.096	0.4671	0.0374	0.0179
h^3_1	−0.388	−0.231	−0.2156	−0.2049
h^3_2	0.506	0.516	0.3593	0.3302
h^3_3	−0.299	−0.1131	−0.2680	−0.2403
g^4_0		−0.7466	0.0022	−0.1036
g^4_1		0.3282	0.0229	0.0452
g^4_2		−0.338	0.0175	−0.0301
g^4_3		0.1826	−0.1235	−0.1363
g^4_4		−0.1429	−0.2005	−0.2512
h^4_1		0.3283	0.1871	0.2492
h^4_2		−0.2131	0.2449	0.3482
h^4_3		−0.0606	0.0136	−0.0293
h^4_4		−0.0486	0.0613	0.0420
g^5_0		−0.066	−0.0893	−0.1854
g^5_1		0.0737	−0.0395	−0.0807
g^5_2		−0.1711	0.0369	0.0731
g^5_3		−0.1793	−0.0357	−0.0655
g^5_4		−0.0077	−0.0483	−0.0605
g^5_5		−0.0740	0.0236	0.0633

Continued on next page

g_m^ℓ, h_m^ℓ	Galileo model Yu et al. (2010)	model Hess et al. (2011)	JTA1 model Ridley (2013)	JTA2 model Ridley (2013)
h_1^5		0.2065	0.0509	0.1697
h_2^5		−0.1167	−0.0330	−0.0635
h_3^5		−0.0288	0.0420	0.1291
h_4^5		−0.0050	0.1352	0.2193
h_5^5		−0.2279	0.0794	0.1374
g_0^6			−0.0255	−0.0922
g_1^6			−0.0251	−0.0682
g_2^6			0.0174	0.0174
g_3^6			0.0254	0.0323
g_4^6			0.0044	0.0274
g_5^6			0.0058	0.0616
g_6^6			−0.0071	−0.0315
h_1^6			−0.0118	−0.0262
h_2^6			−0.0075	−0.0142
h_3^6			−0.0238	−0.0522
h_4^6			0.0384	0.1170
h_5^6			0.0355	0.0299
h_6^6			0.0221	0.0132
g_0^7			0.0179	0.0503
g_1^7			−0.0090	−0.0204
g_2^7			−0.0011	0.0085
g_3^7			0.0099	0.0200
g_4^7			0.0123	0.0337
g_5^7			−0.0040	−0.0270
g_6^7			0.0144	0.0318
g_7^7			0.0013	−0.0013
h_1^7			0.0044	0.0046
h_2^7			0.0045	0.0035
h_3^7			−0.0041	−0.0086
h_4^7			−0.0141	−0.0426
h_5^7			0.0148	0.0224
h_6^7			0.0171	0.0361
h_7^7			−0.0016	−0.0118

For this work, the most interesting radii r are the surface of the planet and the top of the dynamo region which is expected at 85% of the planetary radius (Chabrier et al. 1992, Fortney and Nettelmann 2010), since the metallization is predicted to take place around $85-90\%$ of $R_♃$. The plots of the spectra $R_\ell = R(\ell)$ and $R_m = R(m)$ are displayed in Fig. 1.9 at the surface $R_♃$ in solid lines and at 85% of $R_♃$ in dashed lines. The left panel shows a clear dominance of the dipole mode $\ell = 1$ that is over one order of magnitude larger than the $\ell > 1$ modes and a relatively flat spectrum in the range of $\ell = 1 - 5$. The right panel shows that orders $m > 0$ have also a small contribution, one order of magnitude lower than the axisymmetric $m = 0$, with a local increase around $m = 3 - 5$. This might suggest some significance of higher harmonics in Jupiter’s dipole-dominated magnetic field.

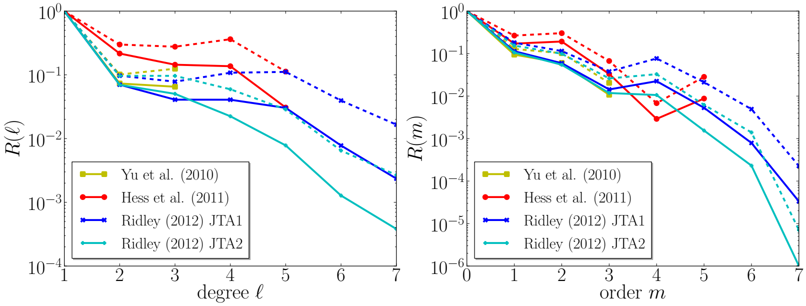

Figure 1.9: Power spectra (Lowes 1966) of the magnetic energy of Jupiter at the surface $r = R_{♃}$ (solid lines) and at $r = 0.85\,R_{♃}$ (dashed lines) as a function of ℓ on the left panel and of m on the right panel. Each of the four spectra is normalized by its maximum value. Yu et al. (2010) calculated the Gauss coefficients from the data of the Galileo mission; Hess et al. (2011) from Voyager, Pioneer and Io’s auroral emissions; Ridley (2013) from Pioneer, Voyager, Ulysses and Galileo (see Tab. 1.1).

1.4 Jupiter’s surface flow

Cloud-tracking methods from both ground-based observations and spacecraft measurements provide information about direction and amplitude of the flow at the surface of the giant planets. These methods, in the simplest terms, consist in tracking the displacement of features in multiple images taken at consecutive periods of time. The displacement and the time interval between images gives the velocity of these features. Fig. 1.10 shows the results for all four giant planets, though the focus is now on the gas giants, mainly Jupiter. Fig. 1.11 shows only the jets configuration for Jupiter obtained from data of Voyager 2. Recent calculations from data of Cassini show similar profiles, with small differences attributed to convective storms and to the uncertainty on the solid-body rotation of Saturn which might shift the 0-line (Helled and Guillot 2013).

Both gas giants display a set of alternated prograde and retrograde winds that can be observed clearly in images of the surface of Jupiter as they shape the longitudinal bands of different colours at different latitudes (background image of Fig. 1.11). In both planets, the equatorial jet is the most extensive in latitude (around ±20° for Jupiter and ±35° for Saturn), with winds in the direction of rotation. The equatorial jet is flanked by two jets (at the lower and higher latitude limits) of opposite direction, which are also bounded at their higher/lower latitude limits by two more jets of prograde direction again and so on, till the poles are reached. The smaller-scale higher latitude jets (above and bellow the equatorial prograde and its two flanking retrograde jets) have on average a latitudinal extend of around 2.5° each and smaller amplitudes than the equatorial flow, which reaches values of 100 – 150 m/s for Jupiter and 400 m/s for Saturn. In non-dimensional units (Rossby number, see Chapter 2), these values become $Ro_{♃} = U/(\Omega R_{♃}) \simeq 0.008$ and $Ro_{♄} = U/(\Omega R_{♄}) \simeq 0.04$ for Jupiter and Saturn, respectively, where U, Ω and R are the planets’ surface equatorial peak velocities, rotation velocities and radii (see Aurnou et al. 2007,

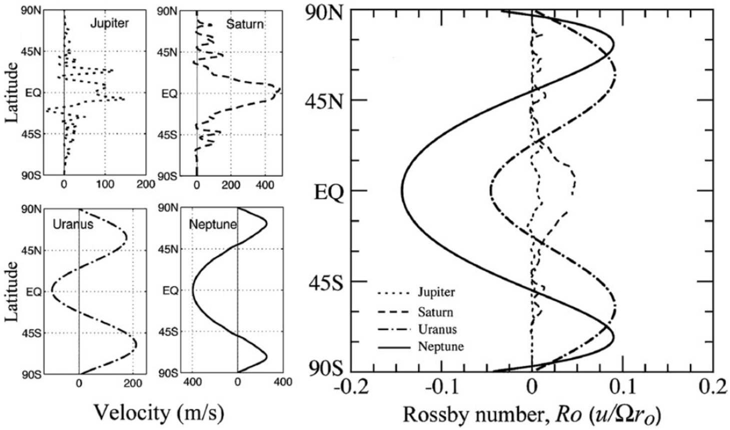

Figure 1.10: The four panels on the left show the zonal flow profiles at the surface of the four giant planets. The panel on the right shows the same profiles gathered in one plot and in units of Rossby number. The image is from Aurnou et al. (2007) and the data is from: Voyager 2, Cassini for Jupiter (Porco et al. 2003), Voyagers 1, 2 for Saturn (Sánchez-Lavega et al. 2000), Voyager 2, Hubble Space Telescope for Uranus (Hammel et al. 2001) and Voyager 2 for Neptune (Sromovsky et al. 1993).

Heimpel and Gómez-Pérez 2011). The lower value of *Ro* for Jupiter shows that this velocity is smaller relatively to the planet's rotation velocity, since Jupiter is one of the fastest rotators of the Solar System. Since the Rossby number is defined as a ratio between the inertia of the flow and Coriolis Force, low values mean simply that rotation is by far the dominating effect in the dynamics of the surface flow based on a length scale of the planetary radius, since large-scale motions are without a doubt rotation-dominated.

Finally, it is worth comparing Jupiter's surface zonal winds profile with Saturn's. Figure 1.10 shows that Saturn's equatorial jet is clearly broader in latitude (from -30 to $+30°$) than Jupiter's (from -15 to $+15°$). The depth of these equatorial surface jets is not known, but the difference between Jupiter and Saturn's might reflect the different interior structures. When considering the main equatorial jet under geostrophic balance, i.e. of constant amplitude along parallels to the rotation axis (z in cylindrical coordinates), its depth could be limited by the region in the interior where the dynamo operates and where the Lorentz force brakes the zonal winds by balancing Reynolds stresses (see Chapters 3 and 4 and Christensen 2002, Heimpel et al. 2005). Figure 1.1 confirms this tendency, since the conducting metallic layer extends closer to the surface in Jupiter than in Saturn, thus the latter is expected to have a more extended jet.

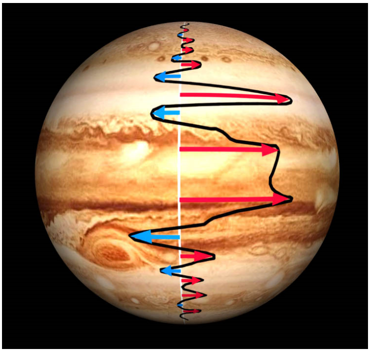

Figure 1.11: Zonal flow profile at the surface derived by Limaye (1986) from data of Voyager 2. The red/blue arrows indicate prograde/retrograde winds, respectively. The background image was taken by NASA's Cassini spacecraft.

1.5 Jupiter's interior flow

The Galileo atmospheric probe provided the only data measured *in situ* of the zonal flow velocity profile bellow the upper cloud level. The measurements, shown in Fig. 1.12, were done down to the 21-bar level or around 156 km, at a latitude of ∼ 6.5°N. Near this depth, when the probe ceased communication, the pressure was near 21 bar and the temperature 153°C. After transmitting almost 1 hour of local weather data, the probe stopped transmitting to the spacecraft overhead, in orbit, most likely due to overheating.

The most unexpected result from the atmospheric probe was the increase of the wind speed, below the 1-bar level and down to the 4-bar level, relatively to the surface wind speed. Below 4-bar, the amplitude of the zonal wind remains approximately constant, though almost twice its surface value. Thus while the peak surface wind speed in non-dimensional units is $Ro \simeq 0.008$, at ∼ 150 km bellow the surface (typically assumed to be the 1-bar level) the wind may reach amplitudes of $Ro \simeq 0.014$ at ∼ 20 bar. This is particularly interesting for this work, since the values of Ro obtained at the top boundary in the models are mostly of the order 10^{-1} (see Chapter 4).

Even though there is an increase in wind velocity during the first quarter of the pressure levels covered in Galileo's probe descent, the amplitude stays roughly constant deeper down. These results offer clues about the driving force of the surface wind. Some authors support the idea of a shallow origin, either by moist convection (release of latent heat from the condensation of water possible only in a shallow layer between 1 and $5-10$ bar), by insolation or by baroclinic instabilities that inject turbulence in a nearly 2D flow (Vasavada and Showman 2005, Showman et al. 2006, Li et al. 2006, Lian and Showman 2008, 2010). Since the light from the Sun is absorbed only down to around the 5-bar level, the winds would be expected to decrease in amplitude with depth if insolation was their primary energy source (see, for example, Ingersoll and Cuzzi 1969, Kaspi and Flierl 2007, Kaspi et al. 2009). According to Kaspi and Flierl (2007), the results from the Galileo probe do not invalidate this hypothesis since the thermal wind shear profiles

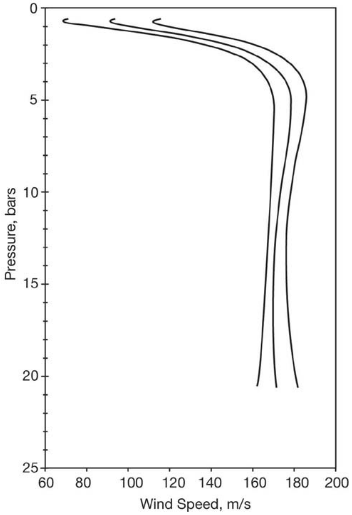

Figure 1.12: Zonal flow profile with depth from data of Galileo's atmospheric probe (Atkinson et al. 1998). The three curves show the range of acceptable solutions for a ±0.21% error in the longitude of the probe descent, ±5% velocity variations and thermal response corrections (Atkinson et al. 1997).

observed for Jupiter suggest an increase of wind speed with depth or simply because the probe descended in a hot spot, i.e. a region of the atmosphere deprived of clouds to absorb the heat released from the interior and of which the origin is uncertain. Furthermore, the probe merely scratches the outer 0.1% of Jupiter's radius, thus it does not reveal the deep-seated dynamics. The other possible driving force is an internal heat source. This means that the winds are directly maintained by deep-seated convection. The Taylor-Proudman theorem states that the flow has to develop as 2D columns in the absence of curvature, thus in a spherical shell an additional axial flow arises along the columns that cross the entire bulk along parallels to the rotation axis (Busse 2002, Vasavada and Showman 2005). This deep-seated forcing mechanism is clearly relevant for the present work, as the amplitudes of the flows can be quantified throughout the convective interior in numerical simulations and roughly compared to Jupiter's observed values at the surface.

1.6 Dynamo models

Carl Friedrich Gauss predicted in 1838 that the origin of the planetary magnetic field must be internal, which brought the necessity of studying the mechanism that generates it, hidden deeper down in the core of the planet. Almost one century later, Walter M. Elsasser suggested, as the mechanism to generate the magnetic field, the existence of self-sustained dynamo action driven by convection in a layer of electrically conducting

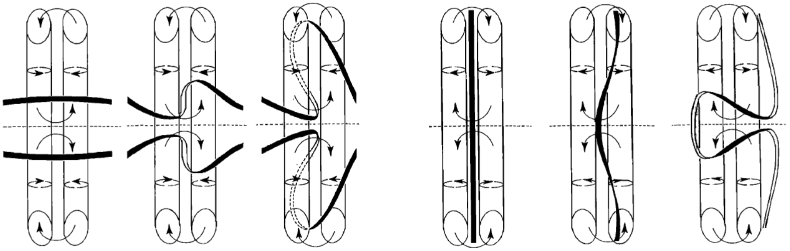

Figure 1.13: Generation of toroidal (left) and poloidal (right) magnetic field from poloidal and toroidal, respectively, due to the action of flow helicity. The arrows represent the directions of the two types of fluid motion: the 2-D convection cells that form the convection columns and the circulation along the rotation axis through the interior of the columns. The thick black lines correspond to magnetic field lines. The image was taken from Olson et al. (1999).

fluid material in the interior of Earth. The magnetic field generated in the interior would then be composed of two types of geometry: poloidal and toroidal. Later on, seismology confirmed the existence of such liquid layer, where the material (mostly iron) is molten. This is where Fluid Dynamics comes in, coupled with the magnetic induction process, in the system of equations that describe dynamo action, known as Magnetohydrodynamics. The Earth was naturally the first target for the study of such interior dynamo mechanism, since it was the subject of the first measurements performed. However, as seen in the previous sections, similar conditions for self-sustained dynamo action exist in the interior of a gas giant planet.

Every planet in the Solar System rotates around its own axis and expels heat through its surface to space. The most efficient way to transfer this energy outward through a layer of liquid material inside the planet is convection. The convection cells are in reality convective columns parallel to the rotation axis. The convection columns or Taylor columns are explained by the Taylor-Proudman theorem that states that in a large-scale flow dominated by rotation, the force balance is mainly between the Coriolis force and the pressure gradients, which translates into a fluid velocity independent of the direction of the rotation axis, thus the convection cells are approximately two-dimensional (geostrophic), i.e. they form convection columns.

Considering that the fluid in the core is composed of electrically conducting material, a dynamo may be generated and permanently maintained by the induced currents. In a self-sustained dynamo, the kinetic energy of the convective motions is constantly converted into magnetic energy through magnetic induction, by two key processes described by Parker (1955). One is called the α-effect which converts the toroidal magnetic field into poloidal and back, the other is the Ω-effect which converts poloidal into toroidal field via shear. The former effect arises when the flow is helical, where helicity is the divergence between the flow velocity and vorticity; this means that there is no helicity in a purely geostrophic flow. The flow that composes the columns becomes non-geostrophic when it meets the curved boundaries of the spherical shell at the ends of the column, generating

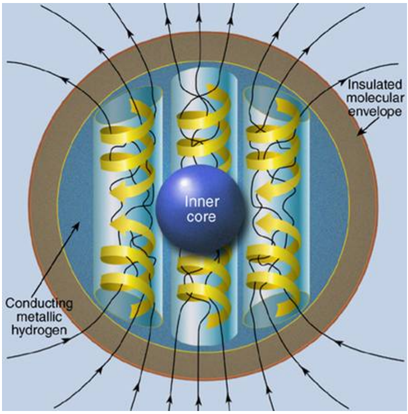

Figure 1.14: Dynamo mechanism operating inside the metallic core of a gas giant, through the generation of poloidal magnetic field (black thin arrows) by the helical flow (yellow thick arrows) organized in convection columns around the inner rocky core.

a secondary type of circulation through the columns, along the direction of the rotation axis. Now the divergence of the flow velocity and vorticity is no longer zero and the flow is helical. The action of helicity to generate poloidal (toroidal) field from toroidal (poloidal) according to the Parker loop model (Parker 1955) is illustrated in Fig. 1.13, where in both situations, the magnetic field lines are twisted by the helical flow motions, stretched and folded around the convection columns. Figure 1.14 shows this mechanism in action in a planetary schematic of a gas giant.

The second process for generation of magnetic field is the Ω-effect illustrated in Fig. 1.15, which can be rather secondary in some dynamo models. This process involves the azimuthal flow component (also called differential rotation due to its dependence with latitude or with radius), since it exclusively generates toroidal field from poloidal in planetary models. The azimuthal flow arises from the westward or eastward tilt of the 2-D convection cells, as momentum is carried away from the rotation axis in the direction of the tilt, making the outer fluid rotate faster in that direction. The correlation of this enhanced azimuthal flow component and the radial component (known as the Reynolds stresses) ensures the presence of significant zonal flows that shear the poloidal field lines in azimuthal direction, stretching them around the planet and creating toroidal field lines.

Both processes described above are typical terminology of mean-field dynamo theory, which studies the generation of large-scale magnetic field while averaging the fluctuating small-scales. The electromotive force is expanded in a mean value with coefficient α plus its fluctuation, as an attempt to achieve scale separation between the mean and fluctuating components of the field.

Typical geodynamo models bear strong columnar convection and assume that the mass density is constant with radius in the fluid core (Boussinesq approximation), thus the flow is dominated by large-scale helical motions that produce the magnetic field. In such type

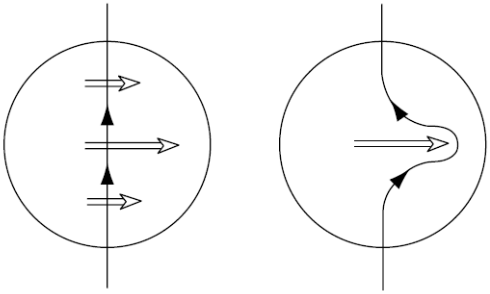

Figure 1.15: Generation of toroidal from poloidal magnetic field, due to the action of differential rotation (white arrows). The black arrows represent magnetic field lines. The image was taken from Roberts (2007).

of dynamo mechanism, both poloidal and toroidal components of the field are generated from the other by α-effect, naming it an α^2-dynamo (Moffatt 1978). However, another type of dynamo mechanism arises if the Ω-effect takes over the generation of toroidal magnetic field from poloidal. These are called $\alpha\Omega$ or $\alpha^2\Omega$-dynamos, depending on the relative importance of the effect. Strong differential rotation is needed for this effect to play a significant role, which may be promoted by features like an outer free-slip mechanical boundary condition (Simitev and Busse 2009, Schrinner et al. 2012, Gastine et al. 2012) or by a strong density contrast in the outer part of the fluid core that concentrates convection near the outer boundary (Gastine and Wicht 2012). Neither of these takes part in a geodynamo model though, where the density contrast is only around 30%, thus is commonly neglected altogether, and the boundaries are assumed rigid.

Past findings of Christensen and Aubert (2006) for geodynamo-like models need now to be tested as well. They carried out a parameter study where they modelled a rotating spherical shell of aspect ratio 0.35, with mechanical rigid boundary conditions and constant density throughout. One of their findings was the minimum requirement for the onset of dynamo action of a magnetic Reynolds number (ratio between magnetic advection and magnetic diffusion) is $Rm \sim 50$ for dipole-dominated magnetic fields and around 100 for multipolar dynamos. Christensen and Aubert (2006) found that dipole-dominated action in rotating spherical shells was possible as long as the Rayleigh number (ratio between buoyancy and viscosity forces, i.e. the strength of convection over conduction) was not too large. As Sreenivasan and Jones (2006) showed, there is a key role of inertia in the morphology of the resulting magnetic field, where low inertia models best approach the geodynamo. The relative role of inertia can be measured by the ratio between inertial and Coriolis forces, the Rossby number. Christensen and Aubert (2006) found a better way to quantify the effect through what they called the local Rossby number Ro_ℓ (see next Chapter for more details), which is based on a local flow length scale instead of the convective layer thickness as it is done for the standard Rossby number. They successfully separated dipole-dominated from multipolar magnetic fields, either below or above the transitional value of $Ro_{\ell cr} \approx 0.1$, respectively, independently of Ekman, Rayleigh or Prandtl numbers (ratios between diffusivities of the system, see Chapter 2). They attributed this abrupt transition to columnar breakdown, i.e. the loss of helical motion which is accompanied by a decrease of the α-effect. Alternatively, a dipolar field increases helicity and consequently α, thus assuring the dipole configuration of the field (Sreenivasan and Jones 2011). However, they observed one exception of a model with $Ro_\ell < Ro_{\ell cr}$ that had also a multipolar solution, which they did not discuss. This was the first suggestion of bistability in dynamo models (or more precisely, of two attractors).

Bistability was later systematically found in Boussinesq models, but when free-slip boundary conditions were employed instead of no-slip (Simitev and Busse 2009, Schrinner et al. 2012). In the former there is less dissipation to balance the shear flow. In the case of no-slip boundaries, the viscous drag at the boundary does the job, but for free-slip, there is only the bulk viscosity available, thus the zonal flow is much more pronounced. These boundaries now allow strong zonal winds to develop that compete with large-scale magnetic fields. On the dipolar branch zonal winds are weak, quenched by the Lorentz force, but on the multipolar branch they are stronger. When no-slip conditions are used, zonal flows generally remain weaker and only the dipolar branch is found for $Ro_\ell < Ro_{\ell cr}$, which was the case of the parameter regime used by Christensen and Aubert (2006).

For a gas giant like Jupiter, the density gradient across the fluid cannot be neglected, as shown before in Fig. 1.7. Models that take into account considerable density gradients have only recently started to be explored, with a first attempt by Stanley and Glatzmaier (2010) where they considered a dynamo generated close to the top of the conducting liquid core of Jupiter, and they did so by modelling a thin convective shell. Another feature that they considered was the electrical conductivity gradient, since it was shown in the previous sections that the transition between the conducting inner part and the molecular outer envelope of Jupiter is continuous, which makes the classical separation of the dynamics for the two layers questionable. Other authors have explored these two effects separately. Gómez-Pérez et al. (2010), Heimpel and Gómez-Pérez (2011) studied the influence of varying only the electrical conductivity and they mostly found weak mutipolar magnetic fields when applying a separation between the two layers of Jupiter at around $0.8\,\mathrm{R}_{♃}$. However in the 2011 work, they presented a solution at a lower value of Ekman number (ratio between viscous and Coriolis force, i.e. a measure of the rotation rate) which allowed for a strong axial dipole magnetic field, if the paremeter set was close to the onset of dynamo action. Such solution also contained a strong surface equatorial zonal flow.

The effect of density stratification was first studied by Gilman and Glatzmaier (1981) and later in a stellar context by Dobler et al. (2006) and Browning (2008), where the latter found a strong tendency also towards multipolar magnetic field configurations for strong density gradients. Chapter 3 introduces a more extensive parameter study of density stratification models (see also Gastine et al. 2012) as an attempt to clarify this dependence. Jones and Kuzanyan (2009) explored linear compressible models and later a benchmark was performed by different codes (Jones et al. 2011), an important step for the new generation of dynamo models.

The present work extends past work by adding background radial density and electrical conductivity profiles, where the latter is loosely based on the *ab initio* calculations by French et al. (2012). Following Gómez-Pérez et al. (2010) and Heimpel and Gómez-Pérez (2011), here the electrical conductivity profile assumes a constant value in the metallic region and an exponential decay in the molecular region. Jones (2003) estimated a magnetic Reynolds number Rm around 10^5 by deriving typical amplitudes of velocity and magnetic field in the conducting core of Jupiter from a MAC balance (comparable forces buoyancy/Coriolis and Coriolis/Lorentz for velocity and magnetic field, respectively, where the latter requires the use of the length scale of the field variation inferred from numerical simulations). Using here the radial profile of electrical conductivity derived by French et al. (2012), Rm would be around 50 at 93% of Jupiter's radius. Thus it is acceptable in this work to assume that the electrical conductivity is constant in the conducting metallic layer, in order for the magnetic Reynolds number to be above 50 around $80-90\%$ of the planetary radius.

A Jupiter-like surface wind pattern was explored more extensively in the past as a feature of non-magnetic models, where typically the molecular convective layer is modelled independently in a thin rotation shell. Their driving forces and depth are still debated. Some authors argue that they are a shallow weather phenomenon (Williams 1978, Cho and Polvani 1996) while others promote deeper-rooted jets that extend through the whole molecular envelope. Heimpel et al. (2005) modelled a Boussinesq fluid in a rotating spherical thin shell without a magnetic field and obtained a pattern of alternating prograde/retrograde zonal winds very similar to Jupiter's surface observations. Jones and Kuzanyan (2009), Gastine and Wicht (2012) carried out similar simulations, but taking into account the density gradient, finding multiple surface jets as well, though different strength of the driving is required. Lian and Showman (2008) show that even when the forcing is restricted to a shallow weather layer the jets may reach much deeper into the planet. Kaspi et al. (2009), on the other hand, presented an anelastic deep convection model where the equatorial zonal flow is geostrophic, but the higher latitude jets are confined to the outer few percent in radius. In this thesis, magnetic simulations are conducted where the flow is naturally driven by convection in the interior of a thick shell, thus typically only the equatorial jet is found.

2 Model

2.1 Compressible MHD equations

2.1.1 Navier-Stokes and continuity equations for a compressible fluid

The Navier-Stokes equation describes the motion of a fluid in a domain with a prescribed type of boundaries. In this work, we consider thermal convection of a fluid in a rotating spherical shell. The Navier-Stokes equations are partial differential equations describing the evolution of momentum $\rho\mathbf{u}$. Their formulation in a rotating frame of reference and in the presence of a magnetic field is

$$\frac{\partial(\rho\mathbf{u})}{\partial t} + \mathbf{u}\cdot\nabla(\rho\mathbf{u}) = -\nabla P + \boldsymbol{\Omega}\times(\boldsymbol{\Omega}\times r) + 2\boldsymbol{\Omega}\times\mathbf{u} + \rho\mathbf{g} + \mathbf{J}\times\mathbf{B} + \nabla\cdot\mathsf{T}, \tag{2.1}$$

where $\mathbf{J}$ is the electric current density, $\boldsymbol{\Omega}$ is the angular velocity vector and $\mathbf{B}$ the magnetic field vector. For a Newtonian fluid the rate-of-stress tensor

$$\mathsf{T} = \mu\left[\left(\frac{\partial u_i}{\partial x_j} + \frac{\partial u_j}{\partial x_i}\right) - \frac{2}{3}\delta_{ij}\nabla\cdot\mathbf{u}\right] \tag{2.2}$$

represents the viscous forces, where μ and ν are, respectively, the dynamic and kinematic viscosities of the fluid. The centrifugal force $\boldsymbol{\Omega}\times(\boldsymbol{\Omega}\times r)$ can be expressed as the gradient of a potential and it is incorporated into the modified pressure p. Oblateness of the model, which results from the action of the centrifugal force, is omitted here and the interior of the planet is modelled as a spherical shell.

The conservation of mass of the system is assured by the continuity equation, which in the compressible form is given by

$$\frac{\partial\rho}{\partial t} + \nabla\cdot(\rho\mathbf{u}) = 0. \tag{2.3}$$

2.1.2 Induction equation for a compressible fluid

The induction equation is constructed by using the modified Ohm's law for a moving conductor $\mathbf{J} = \sigma(\mathbf{E} + \mathbf{u}\times\mathbf{B})$, where σ is the conductivity of the material and $\mathbf{J}$ the current density. The electric field density $\mathbf{E}$ can be expressed via the Maxwell–Faraday equation $\nabla\times\mathbf{E} = -\partial\mathbf{B}/\partial t$ after taking the curl of Ohm's law. The Ampère's circuital law allows the elimination of the current density and it is given by

$$\nabla\times\mathbf{B} = \left(\mu_0\,\mathbf{J} + \frac{1}{c^2}\frac{\partial\mathbf{E}}{\partial t}\right), \tag{2.4}$$

where μ_0 and c are the permeability of vacuum and the speed of light, respectively. In the non-relativistic limit of $|\mathbf{u}| \ll c$, the displacement current term $\partial_t \mathbf{E}$ in Ampère's law can be neglected. Together with Ohm's law, $\mathbf{E}$ may be written as a function of $\mathbf{B}$:

$$\left.\begin{aligned} \mathbf{E} &= \frac{\mathbf{J}}{\sigma} - \mathbf{u} \times \mathbf{B} \\ \mathbf{J} &= \frac{1}{\mu_0} (\nabla \times \mathbf{B}) \end{aligned}\right\} \Rightarrow \mathbf{E} = \frac{1}{\mu_0 \sigma} (\nabla \times \mathbf{B}) - \mathbf{u} \times \mathbf{B}. \tag{2.5}$$

The time dependence of the magnetic field density $\mathbf{B}$ may be obtained as a function of $\mathbf{B}$ and $\mathbf{u}$ through Faraday's law, in what it's called the induction equation,

$$\frac{\partial \mathbf{B}}{\partial t} = \nabla \times (\mathbf{u} \times \mathbf{B}) + \nabla \times (\lambda \nabla \times \mathbf{B}), \tag{2.6}$$

where $\lambda = 1/(\mu_0 \sigma)$ is the magnetic diffusivity. As long as λ is a constant, the diffusive term simplifies as $\nabla \times (\lambda \nabla \times \mathbf{B}) = \lambda [\nabla \times (\nabla \times \mathbf{B})]$. In addition, making also use of another MHD equation,

$$\nabla \cdot \mathbf{B} = 0, \tag{2.7}$$

the diffusive term may be written as

$$\lambda \; [\nabla \times (\nabla \times \mathbf{B})] = \lambda \nabla^2 \mathbf{B}. \tag{2.8}$$

2.1.3 Energy equation for a compressible fluid

The heat flux conducted down the adiabat, used as reference state, is given by $k\nabla T$, where k is the thermal conductivity. The energy equation is given by

$$\rho c_p \left(\frac{\partial S}{\partial t} + \mathbf{u} \cdot \nabla S \right) = \nabla \cdot (k \nabla T) + Q_v + Q_{ohm}, \tag{2.9}$$

where Q_v and Q_{ohm} are the heat sources/sinks due to viscous and Ohmic heating, respectively:

$$\begin{aligned} Q_v &= \rho \nu \left(\frac{\partial u_i}{\partial x_j} \frac{\partial u_i}{\partial x_j} + \frac{\partial u_i}{\partial x_j} \frac{\partial u_j}{\partial x_i} - \frac{2}{3} \delta_{ij} (\nabla \cdot \mathbf{u})^2 \right) \\ Q_{ohm} &= \frac{\lambda}{\mu_0} (\nabla \times \mathbf{B})^2. \end{aligned} \tag{2.10}$$

2.2 Anelastic Model

2.2.1 Thermodynamics – adiabatic state

Solving the anelastic equations is basically solving the perturbations around a quasi-adiabatic reference state. For the anelastic formulation used in this work, this state is assumed to be a reversible adiabatic process, which means that there is no heat transfer and that the entropy of the system is constant. Such approximation holds here because heat is transferred at a much slower rate than the fluid motion (this is the case for atmospheres of planets). Such infinitesimal changes will allow the use of the thermodynamics relations that follow.

The thermodynamic properties of the reference state change along the radius of the domain and these radial profiles may be obtained by looking at basic thermodynamic relations. At constant volume and constant pressure, the heat capacities of a gas correspond to the quantity of heat required to raise the temperature of the gas, obtained from the first law of thermodynamics $dU = dQ - dW = TdS + P/\rho^2 d\rho$, where U, T, S, P and ρ are the internal energy, temperature, entropy, pressure and density per unit mass of a system, respectively. The first term on the right side represents the heat Q added to the system and the second the work W done on it. The specific heat capacities are the amount of Q required to raised the temperature of the system, keeping the volume (c_v) or the pressure (c_p) constant, where "specific" refers to a quantity per unit mass. If the volume is constant, the work done on the system is zero, thus the heat supplied goes into raising the temperature:

$$dU = dQ = c_v dT \Rightarrow c_v = \left(\frac{\partial U}{\partial T}\right)_V = \left(\frac{\partial Q}{\partial T}\right)_V = \frac{1}{T}\left(\frac{\partial S}{\partial T}\right)_V . \tag{2.11}$$

If the pressure is kept constant instead, only part of the heat supplied goes into raising the temperature and part goes into doing external work, i.e. $c_p dT = c_v dT - P/\rho^2 d\rho$. The specific heat capacity at constant pressure is given by

$$c_p = \left(\frac{\partial Q}{\partial T}\right)_P = \frac{1}{T}\left(\frac{\partial S}{\partial T}\right)_P . \tag{2.12}$$

The thermal expansion of a gas corresponds to the increase of its volume with temperature, when the pressure is kept constant. On the other hand, compressibility of the reference gas corresponds to the decrease of its volume with pressure, when assuming constant temperature (it may also be referred to as isothermal compressibility). Replacing the volume by the density, which can be done by resorting to the relation of properties per unit mass $V = 1/\rho$, the coefficients of expansion (α) and compressibility (δ) are

$$\alpha = -\frac{1}{\rho}\left(\frac{\partial \rho}{\partial T}\right)_P \quad \text{and} \quad \delta = \frac{1}{\rho}\left(\frac{\partial \rho}{\partial P}\right)_T . \tag{2.13}$$

In addition, using the ideal gas law in the form $P \propto \rho T$, it can be shown that when $P = constant$, the coefficient of expansion becomes $\alpha = 1/T$ and, when $T = constant$, the coefficient of compressibility simplifies to $\delta = 1/P$. These relations will be used in the next section, which is the second part of the derivation of the reference state.

The entropy of the system is a differentiable property that can be defined in terms of two of the three thermodynamic properties ρ/V, T or P. This allows writing dS as a function of, for example, ρ and P,

$$dS = \left(\frac{\partial S}{\partial P}\right)_\rho dP + \left(\frac{\partial S}{\partial \rho}\right)_P d\rho. \tag{2.14}$$

which together with the equation for hydrostatic equilibrium $dP/dr = -\rho g$, where g represents the acceleration done by gravity, gives a relation for the radial gradient of density

$d\rho/dr$. Since differentiable properties may also be written in the form

$$\left(\frac{\partial S}{\partial P}\right)_\rho \left(\frac{\partial P}{\partial \rho}\right)_S \left(\frac{\partial \rho}{\partial S}\right)_P = -1, \tag{2.15}$$

when assuming any three different thermodynamic properties, in this case S, P and ρ, other similar relations using other two properties together with S and with Eqs. 2.11, 2.12 and 2.13, will lead to equations for the two partial derivatives on the right side of Eq. 2.14:

$$\left(\frac{\partial S}{\partial P}\right)_\rho = \frac{c_v \delta}{T\alpha} \quad \text{and} \quad \left(\frac{\partial S}{\partial \rho}\right)_P = -\frac{c_p}{T\rho\alpha}. \tag{2.16}$$

Replacing Eqs. 2.16 and using the equation for hydrostatic equilibrium, the radial density gradient will be

$$\frac{d\rho}{dr} = -\frac{c_v \delta \rho^2}{c_p} g, \tag{2.17}$$

apart from a term that is a function of the radial entropy gradient which is neglected in a reversible adiabatic process, since this corresponds to an isentropic process as well. In the same way, the radial temperature gradient can be obtained by considering the entropy as a function of T and P and expanding the increment dS similarly as Eqs. 2.14 and 2.15 to obtain

$$\left(\frac{\partial S}{\partial P}\right)_T = -\frac{\alpha}{\rho} \quad \text{and} \quad \left(\frac{\partial S}{\partial T}\right)_P = \frac{c_p}{T}. \tag{2.18}$$

With the use once again of the hydrostatic equilibrium equation, the temperature radial gradient of the adiabatic reference state is

$$\frac{dT}{dr} = -\frac{\alpha T}{c_p} g. \tag{2.19}$$

The two gradients $d\rho/dr$ and dT/dr may be further simplified with the assumption of an ideal gas, as

$$\frac{d\rho}{dr} = -\frac{\rho^2}{P\gamma} g \quad \text{and} \quad \frac{dT}{dr} = -\frac{g}{c_p}, \tag{2.20}$$

since $\alpha = 1/T$ and $\delta = 1/P$. Eqs. 2.20 will go on to be used in the next sections.

2.2.2 Polytrope

Before introducing the system of equations, it is necessary to refer to the material itself that is modelled in this work. The assumption used was a polytropic ideal and perfect gas. Figure 2.1 shows that the density profiles of a polytropic gas are a reasonably good approximation to the realistic background density of the interior of Jupiter (dashed line).

When the gas undergoing a reversible adiabatic process is ideal, it is possible to relate the two heat capacities through the ideal gas constant R. When heat is supplied to a system at constant pressure, some of it goes into raising the temperature, but part of it goes into doing external work, $c_p\, dT = c_v\, dT + P\, dV$. On the other hand, if the volume is kept constant, $dV = 0$, all the heat supplied is used to raise the temperature. Using the ideal gas law and differentiating it at constant pressure, $PV = RT \rightarrow P\, dV = R\, dT$, one can relate

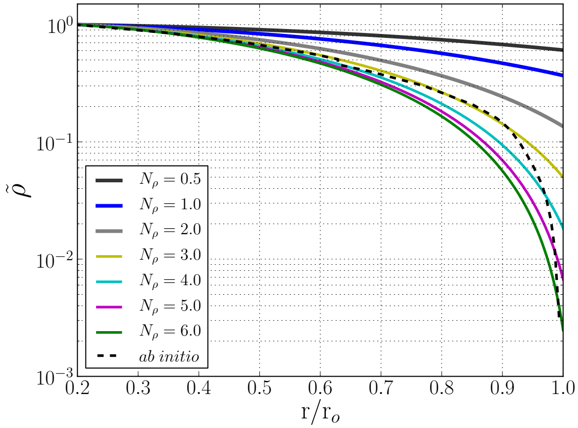

Figure 2.1: Radial profiles of density $\tilde{\rho}(r)$ in the spherical shell geometry modelled here. The colours correspond to different values of N_ρ and the dashed line shows the results of the *ab initio* equations (French et al. 2012), for comparison with the polytrope.

c_v and c_p as $c_p\, dT = c_v\, dT + r\, dT \Rightarrow R = c_p - c_v$. The internal energy of an ideal gas depends solely on its temperature and not on volume, due to the absence of intermolecular forces. Thus using the first law of thermodynamics for a reversible adiabatic state and the c_v relation,

$$\left.\begin{aligned} dU &= -P\, dV \\ dU &= c_v\, dT \end{aligned}\right\} \Rightarrow c_v\, dT = -P\, dV. \tag{2.21}$$

Finally for an ideal gas,

$$\left.\begin{aligned} P &= \frac{1}{V}(c_p - c_v)\, T \\ c_v\, dT &= -P\, dV \end{aligned}\right\} \Rightarrow c_v\, dT = -\frac{1}{V}(c_p - c_v)\, T\, dV. \tag{2.22}$$

The adiabatic index corresponds to the ratio between the two heat capacities: $\gamma = c_p/c_v$. Eq. 2.22 may be re-written as a function of temperature T, volume V and γ. Its integration gives the adiabatic equation:

$$\frac{dT}{T} + (\gamma - 1)\frac{dV}{V} = 0 \;\rightarrow\; T V^{\gamma-1} = \frac{T}{\rho^{\gamma-1}} = constant. \tag{2.23}$$

Furthermore, the ideal gas law allows re-writing the adiabatic equation as a function of pressure, as $PV^\gamma = constant$ or $P/\rho^\gamma = constant$.

A polytropic gas is a solution of the Lane-Emden differential equation and it is characterized by a polytropic index m. The pressure equation of a polytropic gas is given by the adiabatic equation for an ideal gas $P \propto \rho^\gamma$, where the adiabatic index $\gamma = (m+1)/m$ is a constant (for a polytrope). The Lane-Emden differential equation is simply a Poisson-type equation obtained from the mass conservation, the hydrostatic equilibrium and the polytropic equation, i.e. the adiabatic equation for an ideal gas with constant γ. For a monatomic perfect gas, $\gamma = 5/3$ which gives $m = 1.5$ while for a diatomic gas, $\gamma = 7/5 \Rightarrow m = 2.5$. The value used in this work is $m = 2$, a compromise as a choice for a mixture of a diatomic gas (molecular hydrogen) and a monatomic gas (helium).

The aspect ratio of the spherical shell modelled is the parameter $\eta = r_i/r_o$, where the two radii of the inner and outer boundaries may be written in terms of η as $r_i = \eta/(1-\eta)$ and $r_i = 1/(1-\eta)$, respectively. Another parameter, which will be extensively used throughout this thesis, is the number of density scale heights of the polytrope. Going back to the equation for the temperature gradient of an ideal gas (Eq. 2.20), this equation may be integrated to obtain the temperature of the background polytropic state. By non-dimensionazing the temperature with its value at the outer boundary T_o and the radius r with the shell thickness $d = r_o - r_i$, plus adding the boundary conditions $T(r_i)/T_o = (\rho_i/\rho_o)^{1/m} = e^{N_\rho/m}$ and $T(r_o)/T_o = 1$, the temperature profile of the reference polytropic state becomes

$$\frac{T(r)}{T_o} = \frac{e^{N_\rho/m} - 1}{1 - \eta^2}\left(1 - \frac{r^2}{r_o^2}\right) + 1. \tag{2.24}$$

The right-hand side of Eq. 2.19 is considered linear throughout the shell, which is a simplification for the numerical calculations, despite the fact that it is not physically consistent with a radially dependent density stratification profile. As Eq. 2.19 and the second part of Eq. 2.20 show, the gravity profile g is directly related to the radial gradient of temperature across the shell. In the numerical method, this gradient is implemented in the buoyancy term of the momentum equation. Figure 2.2 shows the temperature gradient profiles as functions of radius r, where the linear profile applied here for a polytropic reference state is plotted along side Jupiter's profile from French et al. (2012). The polytropic profiles for different values of N_ρ are shown in different shades of grey colour. Jupiter's profile is represented by two dashed lines, where a few percent of the outer radius was neglected at the surface from the total profile, since the complete profile could not be numerically solved due to the extreme radial gradient in this outer part (see Fig. 1.7). The yellow dashed line corresponds to a cut of 1% of the outermost radius of French et al. (2012)'s profile, while for the red line 2% was removed of the outer part. It is seen in Figure 2.2 that for around 90% of the radius of the shell, the linear profiles follow the realistic model, which only deviates in the outer 10%. In addition, it is noticeable that the slope of the linear part of the realistic profile changes with the cut applied to such model and it increases with smaller cuts. This suggests that a higher number of density scale heights, probably $N_\rho \geq 5$, will better reproduce the full radial temperature profile of Jupiter. The main effect and advantage of the polytropic profiles is to "smooth" the outer gradient of density, as it is numerically easier to solve.

2.2.3 Anelastic approximation

The thermodynamic properties (temperature/entropy, density and pressure) may be defined as a sum of their reference state value (see the two previous sections) and its variation from the reference at each time step, $T = \tilde{T}(r) + T'(r, \theta, \phi, t)$ or $S = \tilde{s}(r) + s'(r, \theta, \phi, t)$, $p = \tilde{p}(r) + p'(r, \theta, \phi, t)$ and $\rho = \tilde{\rho}(r) + \rho'(r, \theta, \phi, t)$. The reference state is thus represented by a tilde, as defined in the previous section, and the perturbation values are marked by an apostrophe. In the anelastic approximation, the fluctuating term is relatively small and the

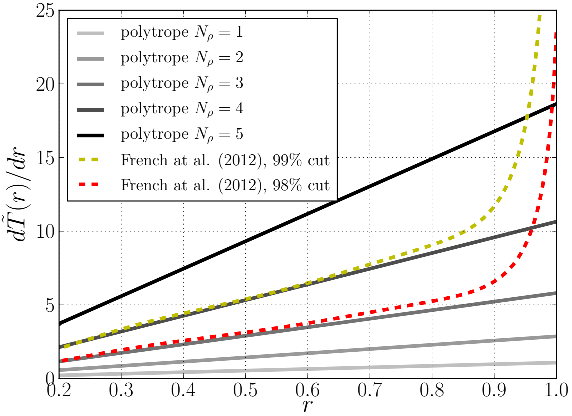

Figure 2.2: Radial profiles of the radial temperature gradient.

mean values correspond to the reference state, assumed here as adiabatic. This approximation assumes that no rapid variations occur so that $\partial\rho/\partial t = 0$, which allows filtering out sounds waves.

In a gas giant, the fluid motions in the interior are assumed to be vigorous enough for an efficient heat transfer which translates into a system close to adiabatic. The reference adiabatic state is then assumed time-independent and a function of radius only, for simplification, while the system of equations is solved only for the small perturbations from the adiabatic reference state.

The thermodynamic variables of the reference state are first order, $o(1)$, while their perturbations, for which the system of equations is solved, are of the order ϵ, $o(\epsilon)$. The former include reference state's $\tilde{\rho}$, $\tilde{p}$, $\tilde{T}$ and the latter the perturbation quantities ρ', p', T'. The expansion parameter $\epsilon = |\rho'|/\tilde{\rho} \ll 1$ is simply the relative measure of the perturbation (apostrophe) compared to its reference constant value (tilde) and all perturbations are considered of similar amplitude, thus ϵ is the same for all thermodynamic variables. The value taken for ϵ is the entropy contrast of the reference state, non-dimensionalized by the heat capacity at constant pressure, $\epsilon = \Delta s/c_p$.

When applying this formulation, which basically separates the variables of the system into a time-dependent (apostrophe) and a time-independent (tilde) parts, the terms retained for the relevant equations will be only the ones of order $o(\epsilon)$. Time derivatives of the reference state are zero and terms with higher order on ϵ are neglected in comparison. Following the formalism of a temperature-based system of equations, pressure and gravity variations are not dealt with in the buoyancy term of the momentum equation since they are absorbed into a "reduced pressure", in the pressure gradient term. This translates into elimination of the density perturbation from the momentum equation altogether. The system chosen for this work is written in terms of entropy instead (Braginsky and Roberts 1995, Lantz and Fan 1999), which also allows such elimination, as is explained in the next paragraph.

The two critical terms of the equations for this formalism are the buoyancy term in the Navier-Stokes equation (Eq. 2.1) and the diffusion term in the energy equation (Eq. 2.27). In the Navier-Stokes momentum equation, Eq. 2.1, the pressure and buoyancy terms together are $(-\nabla p + \rho \mathbf{g})$. Dividing Eq. 2.1 by $\tilde{\rho}$ gives this term as

$$-\frac{\nabla p'}{\tilde{\rho}} + \frac{\rho' \mathbf{g}}{\tilde{\rho}} = -\nabla\left(\frac{p'}{\tilde{\rho}}\right) - \frac{s' \mathbf{g}}{c_p}, \tag{2.25}$$

obtained by expanding $\nabla(p'/\tilde{\rho})$. Here, the relation that comes from deriving the adiabatic equation $\tilde{p}/\tilde{\rho}^{\gamma} = constant$,

$$\nabla\left(\frac{\tilde{p}}{\tilde{\rho}^{\gamma}}\right) = 0 = \frac{\tilde{p}}{\tilde{\rho}^{\gamma}}\left(\frac{\nabla \tilde{p}}{\tilde{p}} - \gamma \frac{\nabla \tilde{\rho}}{\tilde{\rho}}\right) \Rightarrow \frac{\nabla \tilde{p}}{\tilde{p}} = \gamma \frac{\nabla \tilde{\rho}}{\tilde{\rho}}, \tag{2.26}$$

replaces $\nabla\tilde{\rho}$ by $\nabla\tilde{p}$ (minus a proportionality constant), which in turn is replaced by $\nabla\tilde{p} = \tilde{\rho}\,\mathbf{g}$, the hydrostatic equilibrium equation. Acquiring the right-hand side of Eq. 2.26 requires the use of the equation $s'/c_v = p'/\tilde{p} - \gamma\rho'/\tilde{\rho}$ that comes from the first law of thermodynamics with the assumption of an ideal gas $\tilde{p} = \tilde{\rho} R \tilde{T}$ for the reference state and the adiabatic index definition, $\gamma = c_p/c_v$. This transformation finally eliminates the density perturbation from the momentum equation and leaves the buoyancy force as a function of the entropy perturbation only.

The energy equation is shown in Eq. 2.27. With the additional assumption of a closed system to which energy can only be transferred in the form of infinitesimal quantities of heat, then $\tilde{T}\nabla S = c_p \nabla T$. Very small changes are similarly treated as $\tilde{T}s' = c_p T'$. The thermal conductivity k can be expressed as $k = \kappa\rho c_p$, where κ (or κ_T) is the dominant turbulent thermal diffusivity of the classical heat transport (Jones et al. 2011). The final energy equation becomes

$$\frac{\partial S}{\partial t} + \mathbf{v} \cdot \nabla S = \frac{1}{\tilde{\rho}\tilde{T}} \nabla \cdot (\kappa \rho T \nabla S) + Q_v + Q_{ohm}, \tag{2.27}$$

where

$$Q_v = \frac{\nu}{\tilde{T}}\left[\frac{\partial u_i}{\partial x_j} + \frac{\partial u_j}{\partial x_i} - \frac{2}{3}\delta_{ij}\nabla \cdot \mathbf{u}\right]\frac{\partial u_i}{\partial x_j} \quad \text{and} \quad Q_{ohm} = \frac{\lambda}{\mu_0}(\nabla \times \mathbf{B})^2. \tag{2.28}$$

2.2.4 Dimensionless form

A dimensionless formulation of the anelastic approximation is adopted in the following to better control the force balances. Additionally, such analysis can easily be used when establishing scaling laws and extrapolating these to planetary values to determine parameters that are not accessible directly, like the temperature difference between the surface and the bottom boundary of a planetary core.

The shell thickness $d = r_o - r_i$ is used as the reference length scale, the viscous time as the time scale, for entropy the contrast across the shell, for density its value at the outer boundary and $\sqrt{\Omega\mu_0\lambda_i\rho_o}$ for the magnetic field,

$$x^* = \frac{x}{d}, \; t^* = \frac{t}{d^2/\nu}, \; u^* = \frac{u}{\nu/d}, \; s^* = \frac{s}{s_o - s_i}, \; \tilde{\rho}^* = \frac{\tilde{\rho}}{\rho_o}, \; B^* = \frac{B}{\sqrt{\Omega\mu_0\lambda_i\rho_o}}, \tag{2.29}$$

where x represents the spatial coordinates, u the flow velocity, s the entropy, ρ the density, Ω the angular velocity, λ_i the magnetic diffusivity at r_i (constant in Chapter 3, see section 2.4 for the variable case) and B the magnetic field. As a reminder, the subscripts o and i refer to constant values at the top r_o and bottom r_i boundaries of the spherical shell, respectively. The parameter μ_0 is the magnetic permeability. Dropping the star * that distinguishes the dimensionless variables from dimensional, the resulting equations become

$$\begin{aligned} \nabla \cdot (\tilde{\rho}\,\mathbf{u}) = 0 \\ \nabla \cdot (\mathbf{B}) = 0, \end{aligned} \tag{2.30}$$

$$\begin{aligned} E\left(\frac{\partial \mathbf{u}}{\partial t} + \mathbf{u}\cdot\nabla\mathbf{u}\right) = -\nabla\frac{p}{\tilde{\rho}} - 2\mathbf{e}_z \times \mathbf{u} + \frac{Ra\,E}{Pr} g s\,\mathbf{e}_r + \\ + \frac{1}{Pm_i\,\tilde{\rho}}(\nabla\times\mathbf{B})\times\mathbf{B} + \frac{E}{\tilde{\rho}}\nabla\cdot\mathsf{T}, \end{aligned} \tag{2.31}$$

$$\frac{\partial \mathbf{B}}{\partial t} = \nabla\times(\mathbf{u}\times\mathbf{B}) - \frac{1}{Pm_i}\nabla\times(\tilde{\lambda}\nabla\times\mathbf{B}), \tag{2.32}$$

$$\begin{aligned} \tilde{\rho}\,\tilde{T}\left(\frac{\partial s}{\partial t} + \mathbf{u}\cdot\nabla s\right) = \frac{1}{Pr}\nabla\cdot(\tilde{\rho}\tilde{T}\nabla s) + \\ + \frac{Pr}{Ra}(1-\eta)c_0 Q_\nu + \frac{Pr}{Pm_i^2\,Ra\,E}(1-\eta)c_0 Q_j. \end{aligned} \tag{2.33}$$

This system of equations is governed by four dimensionless parameters, namely the Ekman number E, the Rayleigh number Ra, the Prandtl number Pr and the magnetic Prandtl number Pm,

$$E = \frac{\nu}{\Omega d^2},\;\; Ra = \frac{g_o d^3 \Delta s}{c_p \nu \kappa},\;\; Pr = \frac{\nu}{\kappa},\;\; Pm_i = \frac{\nu}{\lambda_i} \tag{2.34}$$

and by the parameters that describe the reference state,

$$\eta = \frac{r_i}{r_o},\;\; m,\;\; N_\rho = \ln\left(\frac{\rho_i}{\rho_o}\right), \tag{2.35}$$

where, as a reminder, ν is the kinematic viscosity, κ is the thermal diffusivity, $\lambda_i = \tilde{\lambda}(r_i)$ is the magnetic diffusivity at the inner boundary, $d = r_o - r_i$ is the thickness of the spherical shell, $\Delta s = s(r_o) - s(r_i)$ is the fixed super-adiabatic entropy contrast across the shell that drives convection, g_o is the value of gravity at the outer boundary, Ω is the rotation rate, c_p is the heat capacity at constant pressure, m is the polytropic index, η is the aspect ratio and N_ρ is the number of density scale heights.

It is worth pointing out that the Boussinesq formulation can be recovered from the anelastic system described here by considering $N_\rho = 0$. In this case, the background density will be constant throughout the domain and the entropy s becomes temperature.

Table 2.1 shows a summary of the dimensionless control parameters used in numerical models like the one described here, listed in Eqs. 2.34 and 2.35. This table points out the difference in the ranges of values accessible to recent numerical simulations from the actual planetary values in the cores of Jupiter and Earth, estimated from observations.

Table 2.1: Range of values of the dimensionless parameters for the present day numerical simulations and values estimated from observations for the Earth (Dziewonski and Anderson 1981, Christensen et al. 2009, Olson 2011) and for Jupiter (Jones 2003, Bagenal et al. 2004, Evonuk and Glatzmaier 2007, French et al. 2012).

Parameters	E	Ra	Pm	Pr	N_ρ
Numerical models	$10^{-6} - 10^{-3}$	$\leq 10^{12}$	$0.1 - 1000$	$0.1 - 1000$	$0 - 6$
Jupiter	5×10^{-19}	$\sim 10^{24}$	$\sim 10^{-7}$	$0.01 - 0.1$	8.5
Earth	$10^{-15} - 10^{-14}$	$\sim 10^{20}$	$10^{-6} - 10^{-5}$	$0.1 - 1$	0.2

2.3 Different dynamo mechanisms

The induction equation introduced in Chapter 2 (Eq. 2.32) contains two mains terms: the induction term that creates magnetic field $\nabla \times (\mathbf{u} \times \mathbf{B})$ and the compensating term that destroys it, the diffusion term $-\nabla \times (\tilde{\lambda} \nabla \times \mathbf{B})$. Addressing first the induction term, it contains three processes, which can either have a positive effect on $\mathbf{B}$ production, like shearing by the differential rotation of the velocity field, or a negative effect, like advection and compressibility. All three are shown on the right side of the following expansion:

$$\nabla \times (\mathbf{u} \times \mathbf{B}) = \underbrace{\mathbf{u}(\nabla \cdot \mathbf{B})}_{=0,\text{ Eq. 2.30}} - \underbrace{\mathbf{B}(\nabla \cdot \mathbf{u})}_{\text{compression}} + \underbrace{(\mathbf{B} \cdot \nabla)\mathbf{u}}_{\text{shear}} - \underbrace{(\mathbf{u} \cdot \nabla)\mathbf{B}}_{\text{advection}} . \tag{2.36}$$

The first relevant term for the next sections is the production of axisymmetric toroidal magnetic field $\mathbf{B}_\phi$ by the zonal flow $\mathbf{u}_\phi$, the shear therm known as the Ω-effect. Splitting the vector fields of velocity and magnetic induction in their azimuthally averaged components (overbar) and respective fluctuations (prime), i.e. $\mathbf{u} = \overline{\mathbf{u}} + \mathbf{u}'$ and $\mathbf{B} = \overline{\mathbf{B}} + \mathbf{B}'$, and with the use of Reynolds averaging rules, the shear term becomes

$$\overline{(\mathbf{B} \cdot \nabla)\,\mathbf{u}} = \overline{\left[(\overline{\mathbf{B}} + \mathbf{B}') \cdot \nabla\right](\overline{\mathbf{u}} + \mathbf{u}')} = \underbrace{(\overline{\mathbf{B}} \cdot \nabla)\,\overline{\mathbf{u}}}_{\text{mean shear}} + \underbrace{\overline{(\mathbf{B}' \cdot \nabla)\,\mathbf{u}'}}_{\text{fluctuating shear}} . \tag{2.37}$$

The production of axisymmetric $\mathbf{B}_\phi$ is then

$$(\overline{\mathbf{B}} \cdot \nabla)\,\overline{\mathbf{u}}\Big|_\phi = \overline{B}_r \frac{\partial}{\partial r}\left(\frac{\overline{u}_\phi}{r}\right) + \frac{\overline{B}_\theta \sin\theta}{r} \frac{\partial}{\partial \theta}\left(\frac{\overline{u}_\phi}{\sin\theta}\right) = \Omega. \tag{2.38}$$

The Ohmic diffusion is represented in the induction equation by the diffusion term (second on the right-hand side of Eq. 2.32). Applying a similar expansion to retrieve the mean diffusion part gives

$$\nabla \times (\tilde{\lambda} \nabla \times \overline{\mathbf{B}})\Big|_\phi = \tilde{\lambda}\, \nabla^2 \overline{B}_\phi - \frac{\tilde{\lambda}\, \overline{B}_\phi}{r^2 \sin^2\theta} + \left(\frac{\partial \tilde{\lambda}}{\partial r}\right)\left(\frac{1}{r} \frac{\partial r \overline{B}_\phi}{\partial r}\right) = \text{MD}. \tag{2.39}$$

The other relevant term in the induction mechanism measures the α-effect. The production of mean poloidal magnetic field comes from the balance between the turbulent induction and the diffusion terms (Brown et al. 2010). The poloidal component of the field may be represented by a potential with azimuthal component,

$$\overline{\mathbf{B}}_{pol} = \overline{B}_r\, \mathbf{e}_r + \overline{B}_\theta\, \mathbf{e}_\theta = \nabla \times \left(\overline{A}_\phi\, \mathbf{e}_\phi\right). \tag{2.40}$$

Writing the induction equation Eq. 2.32 in function of the vector potential gives

$$\frac{d\overline{\mathbf{A}}_\phi}{dt} = \underbrace{\overline{\mathbf{u}\times\mathbf{B}}\Big|_\phi}_{\text{emf}} - \underbrace{\frac{1}{Pm_i}\tilde{\lambda}\,\nabla\times\overline{\mathbf{B}}\Big|_\phi}_{\text{ohmic diffusion}} . \tag{2.41}$$

where the first term on the right-hand side represents the electromotive force, emf. This term can be split into mean and fluctuating parts. Brown et al. (2010) found that the dominant term for production of $\overline{A}_\phi$ is the fluctuating part, i.e. the turbulent emf, which is more than one order of magnitude larger than the mean part. Thus the turbulent emf is given by the fluctuating flows and fields, as

$$\overline{\mathbf{u}'\times\mathbf{B}'}\Big|_\phi = \overline{\mathbf{u}_r\,\mathbf{B}_\theta} - \overline{\mathbf{u}_\theta\,\mathbf{B}_r}, \tag{2.42}$$

which in mean-field theory is parametrized by the α-effect.

2.4 Variable conductivity

To simulate the variable electrical conductivity of hydrogen in the interior of Jupiter, we employ a profile that corresponds to a constant conductivity in the metallic hydrogen layer and an exponential decay in the outer molecular envelope. Both branches are matched via a polynomial that also ensures that the first radial derivative is continuous:

$$\tilde{\sigma}(r) = \begin{cases} 1 + (\tilde{\sigma}_m - 1)\left(\dfrac{r - r_i}{r_m - r_i}\right)^a & r < r_m \\ \tilde{\sigma}_m \exp\left[a\,\frac{r - r_m}{r_m - r_i}\,\frac{\tilde{\sigma}_m - 1}{\tilde{\sigma}_m}\right] & r \geq r_m \end{cases} . \tag{2.43}$$

The exponential decay with a rate a starts at a radius r_m where the normalized conductivity has already decreased from $\tilde{\sigma}_i = 1$ to $\tilde{\sigma}_m$. For convenience we also define the relative transition radius in percentage: $\chi_m = r_m/r_o$.

This profile has first been used by Gómez-Pérez et al. (2010) and it seems a fair first approximation to the results from *ab initio* calculations by French et al. (2012). The super-exponential increase of electrical conductivity over the molecular layer is not feasible to model numerically (see Fig. 2.3). We thus mainly use a rate of $a = 9$ for our simulations, but we also tested $a = 25$ in a few cases and $a = 1$ for one case with a different σ_m (grey profile in Fig. 2.3, discussed in section 4.1.2). In all the other cases, $\tilde{\sigma}_m$ was fixed to 0.5 and χ_m was varied assuming values of 95, 90, 80 and 70%. Corresponding simulations for homogeneous conductivity with $\chi_m = 100\%$ can be found in Chapter 3.

2.5 Diagnostic parameters

The parameters of all numerical experiments discussed here are listed in Appendix A along with several diagnostic quantities that characterize the solution and are defined in the following. The amplitude of the zonal flow contribution is measured in terms of the Rossby number Ro_{zon}:

$$Ro_{zon} = \frac{u_{zon}}{\Omega\, d}, \quad \text{with} \quad u_{zon} = \sqrt{\frac{3}{r_o^3 - r_i^3}\int_{r_i}^{r_o} \langle \overline{u}_\phi^2 \rangle\, r^2\, \mathrm{d}r}\,, \tag{2.44}$$

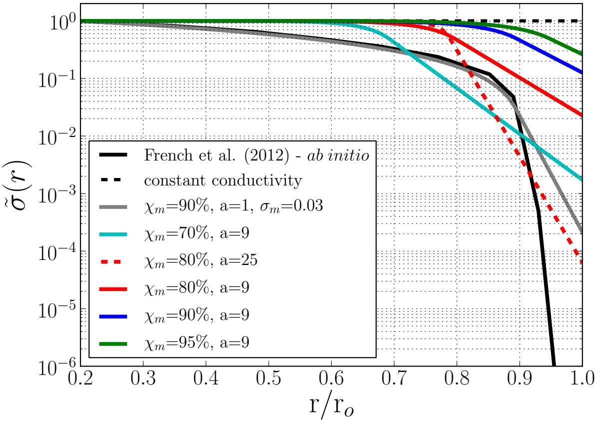

Figure 2.3: Radial profiles of electrical conductivity used in this work. The black line corresponds to the *ab initio* solution from French et al. (2012), see Chapter 1. All the profiles in colour, with either $a=9$ or $a=25$, have $\sigma_m=0.5$.

where u_{zon} is the rms volume-averaged flow velocity, $\overline{u}_\phi$ is the axisymmetric azimuthal flow component, overbars correspond to azimuthal averages and the triangular brackets denote the average over a spherical surface

$$\langle f \rangle = \frac{1}{4\pi} \int_0^\pi \int_0^{2\pi} f(r,\theta,\phi) \sin\theta \, \mathrm{d}\theta \, \mathrm{d}\phi. \tag{2.45}$$

The relative kinetic energy

$$Z = \frac{Ro_{zon}^2}{Ro^2} = \frac{\int_{r_i}^{r_o} \langle \overline{u}_\phi^2 \rangle \, \mathrm{d}r}{\int_{r_i}^{r_o} \langle u^2 \rangle \, \mathrm{d}r} \tag{2.46}$$

is used to quantify the relative importance of zonal flows.

The magnetic Reynolds number R_m estimates the ratio of magnetic field production and diffusion and a modified form is used here to account for the radial-dependent magnetic diffusivity in Chapters 4 and 5:

$$R_m = \frac{3}{r_o^3 - r_i^3} \int_{r_i}^{r_o} \frac{\sqrt{\langle u^2(r,\theta,\phi) \rangle}}{\tilde{\lambda}(r)} \, r^2 \, \mathrm{d}r. \tag{2.47}$$

The local Rossby number is known to be a good proxy of the relative importance of the advection term in the Navier-Stokes equation, Eq. 2.31 (Christensen and Aubert 2006), and it is defined as

$$Ro_\ell = \frac{\sqrt{\frac{1}{V} \int_{r_i}^{r_o} \langle u^2 \rangle \, r^2 \, \mathrm{d}r}}{\Omega \, \ell}, \tag{2.48}$$

where the typical flow length scale is derived from the kinetic energy spectrum,

$$\ell(r) = \frac{\pi\, u^2(r)}{\sum\limits_l l\, u_l^2(r)}, \tag{2.49}$$

where u_l is the flow contribution of spherical harmonic degree l. A modified form of Ro_ℓ based exclusively on the inner conducting region ($r_i \leq r \leq r_m$) is used in Chapters 4 and 5,

$$Ro_\ell = \frac{3}{r_o^3 - r_i^3} \int_{r_i}^{r_m} \frac{\sqrt{\langle u^2(r,\theta,\phi)\rangle}}{\Omega\, \ell(r)}\, r^2\, \mathrm{d}r. \tag{2.50}$$

The magnetic field strength is quantified by the Elsasser number which measures the ratio of Lorentz to Coriolis forces using the modified form

$$\Lambda = \frac{3}{\mu_0\, \Omega\, (r_o^3 - r_i^3)} \int_{r_i}^{r_o} \left\langle \frac{\mathbf{B}^2}{\rho(r)\, \tilde{\lambda}(r)} \right\rangle r^2\, \mathrm{d}r. \tag{2.51}$$

The geometry of the surface field is characterized by the dipolarity

$$f_{dip} = \frac{\left\langle (\mathbf{B}_{l=1}^{m=0})^2 \right\rangle}{\left\langle \sum\limits_{l,m\leq 12} (\mathbf{B}_l^m)^2 \right\rangle}, \tag{2.52}$$

which measures the relative energy in the axial dipole contribution at the outer boundary r_o. Following Christensen and Aubert (2006), the magnetic field is restricted to spherical harmonic degrees and orders below 12 in Eq. (2.52). The table in Appendix A lists time averages of the properties defined above for all models. The time variability of the dipolarity, also listed in Appendix A, is quantified by its standard deviation SD_{dip}.

The local Elsasser number is an alternative to the standard Elsasser number (ratio between Lorentz and Coriolis forces) proposed by Soderlund et al. (2012) that provides a more direct ratio of Lorentz and Coriolis forces in the Navier-Stokes equation. It includes the length scale δ_B of the magnetic field present in the curl in the Lorentz force. This parameter seems to be a better proxy of the actual Lorentz/Coriolis force balance. Soderlund et al. (2012) obtained δ_B from the typical values of spherical harmonic degree and order, ℓ_B and m_B, respectively,

$$\ell_B = \sum_\ell \frac{\ell \langle \mathbf{B}_\ell \cdot \mathbf{B}_\ell \rangle}{\langle \mathbf{B} \cdot \mathbf{B} \rangle} \;,\; m_B = \sum_m \frac{m \langle \mathbf{B_m} \cdot \mathbf{B_m} \rangle}{\langle \mathbf{B} \cdot \mathbf{B} \rangle} \;\rightarrow\; \delta_B = \frac{\pi d}{2\sqrt{\ell_B^2 + m_B^2}}. \tag{2.53}$$

The local Elsasser number Λ_ℓ then becomes

$$\Lambda_\ell = \frac{\Lambda}{Rm} \frac{d}{\delta_B}. \tag{2.54}$$

2.6 Numerical method

Taking advantage of Eqs. 2.30, i.e. the fact that the vector fields $\mathbf{B}$ and $\tilde{\rho}\mathbf{u}$ are solenoidal, both may be expressed as function of two scalar potentials. The advantage of this method, known as the toroidal/poloidal decomposition, is that the fulfillment of the continuity equations for magnetic field $\mathbf{B}$ and mass flux $\tilde{\rho}\mathbf{u}$ is assured. The poloidal and toroidal potentials of $\tilde{\rho}\mathbf{u}$ are W and Z, respectively, and the same potentials for $\mathbf{B}$ are B and A,

$$\begin{aligned} \tilde{\rho}\mathbf{u} &= \nabla \times (\nabla \times W\mathbf{e}_r) + \nabla \times Z\mathbf{e}_r \\ \mathbf{B} &= \nabla \times (\nabla \times B\mathbf{e}_r) + \nabla \times A\mathbf{e}_r \,. \end{aligned} \tag{2.55}$$

The unknowns of the system are then the four vector potentials (W, Z, B and A) plus the two thermodynamic quantities s and p, thus six equations need to be solved. The poloidal components of the vector fields $\rho\mathbf{u}$ (W) and $\mathbf{B}$ (B) are obtained by taking the radial component of Eqs. 2.31 and 2.32, respectively, as "(Eq.)$\cdot\mathbf{e}_r$", while the toroidal components Z and A will be determined from the radial component of the curl of these same two equations, as "($\nabla\times$Eq.)$\cdot\mathbf{e}_r$". The remaining coefficients of entropy $s_{\ell mn}$ and pressure $p_{\ell mn}$ come from the energy equation (Eq. 2.33) and from the horizontal divergence of Eq. 2.31, i.e. "$\nabla_H\cdot$Eq.". All four vector potentials and the thermodynamic variables entropy s and pressure p are expanded in spherical harmonics up to a certain degree ℓ_{max} in longitudinal and latitudinal directions and in Chebyshev polynomials up to degree N_r in radial direction.

The spherical harmonic functions express the dependence of the spherical coordinates ϕ and θ on ℓ (degree) and m (order):

$$Y_{\ell m}(\theta, \phi) = P_{\ell m}(\cos\theta)\, e^{\mathrm{i}m\phi}, \tag{2.56}$$

where $P_{\ell m}(x)$ are Legendre functions. The values at which ℓ and m will be truncated, are specified as the horizontal resolution of the model. This is done through one single value, ℓ_{max}, and ℓ assumes values between 0 and ℓ_{max} and m up to ℓ.

For the radial direction, the Chebyshev polynomials C_n used are of the first kind, defined recursively and used here in their trigonometric version. Furthermore, these polynomials of degree n are a function of the coordinate r_{cheb} in the polynomial space $-1 < r_{cheb} < 1$:

$$C_n(r_{cheb}) = \cos\left[n \arccos\left(r_{cheb}\right)\right]. \tag{2.57}$$

The transition between the Chebyshev polynomial space and the real space is done most commonly through the linear relation

$$r_{cheb} = 2\,\frac{r - r_i}{r_o - r_i} - 1 \quad \Leftrightarrow \quad r = r_i + \frac{d}{2}\left(r_{cheb} + 1\right). \tag{2.58}$$

The points in radial direction in Chebyshev space are distributed according to a cosine function, which concentrates more points near the boundaries in order to more accurately resolve the boundary layers (Chebyshev-Gauss-Lobatto collocation points). In addition, a more practical advantage of such cosine distribution for r_{cheb} is the direct elimination of the arccos() function in Eq. 2.57, such that the Chebyshev polynomials simplify to

$$C_n(r_{cheb}) = \cos\left(n\,\pi\,\frac{k-1}{n_{max}-1}\right), \tag{2.59}$$

where n_{max} is the maximum degree n of the polynomials that is specified, thus it corresponds to the radial resolution of the model.

Applying both horizontal and radial expansions to the unknown variables of the models is then the first step in deriving the equations implemented in the numerical code. As an example for the vector potential A,

$$A(r,\theta,\phi) = \sum_{\ell=0}^{\ell_{max}} \left[\sum_{m=-\ell}^{\ell} \left(\sum_{0}^{n_{max}} A_{\ell mn} C_n(r) \right) Y_{\ell m}(\theta,\phi) \right], \tag{2.60}$$

where $Y_{\ell m}(\phi,\theta)$ is given by Eq. 2.56 and $C_n(r)$ by Eq. 2.59.

The spectral equations are now obtained by expanding all six unknowns (two magnetic potentials, two velocity potentials, temperature and pressure) in spherical harmonics and Chebyshev polynomials, to give equations for their six coefficients $W_{\ell mn}$, $Z_{\ell mn}$, $B_{\ell mn}$, $A_{\ell mn}$, $T_{\ell mn}$ and $P_{\ell mn}$. These six coefficients are the actual unknown variables of the problem.

Due to the presence of non-linear terms in the equations, namely the Coriolis and the Lorentz forces, the advection term in Eq. 2.31, the curl of $(\mathbf{u} \times \mathbf{B})$ in Eq. 2.33, the viscous and ohmic heatings, the time integration requires a combination of implicit and explicit methods, in a mixed implicit/explicit algorithm. The linear terms are solved in spectral space but not the non-linear. These are solved in the physical space, hence several Legendre transforms are needed at each time step to compute them. The non-linear terms are solved explicitly through an Adams–Bashforth scheme, which is a two-step method of the form

$$y_{n+2} = y_{n+1} + \frac{3}{2}\Delta t\, f(t_{n+1}, y_{n+1}) - \frac{1}{2}\Delta t\, f(t_n, y_n), \tag{2.61}$$

i.e. each value of the current time step is obtained from the two previous time steps. The linear terms, on the other hand, are determined with a Crank-Nicolson method, an implicit algorithm that is an average of a fully explicit and a fully implicit methods. The algorithm has the form

$$y_{n+1} = y_n + \frac{\Delta t}{2}\left[f_{n+1}(y, x, t, \partial_x y, \partial_x^2 y) + f_n(y, x, t, \partial_x y, \partial_x^2 y) \right], \tag{2.62}$$

where x represents spatial coordinates and t temporal.

The value of the time step Δt changes during the simulation and it is adjusted according to the Courant-Friedrichs–Lewy (CFL) condition. The CFL criterion relates Δt to the length between two grid points Δx through the relation

$$\mathrm{CFL} = \min\left(u \frac{\Delta t}{\Delta x}\,,\ u_{Alfven} \frac{\Delta t}{\Delta x} \right). \tag{2.63}$$

In other words, the CFL condition requires the time step to be less than the time that a fluid parcel takes to be advected from one grid point to another next to it. Thus, when the grid size is increased, the spatial distance between the grid points decreases and so does the time step. For the numerical implementation of the CFL condition in the code, two values of this quantity are calculated, one where u is the flow velocity, another where it is the Alfvén velocity. The value accounted for in each time step is the lower of the two.

2.7 Boundaries

The boundary conditions are applied on the radial grid, which means that the differential equations for bottom and top grid points are replaced by the equations according to the boundary conditions.

Most of the cases have an outer/top (r_o) free-slip boundary, where $(\mathsf{T} \times \vec{n}) \cdot \vec{n} = 0$, but the no-slip boundary is also applied in a few selected test cases for comparison, where $\vec{u} = 0$. The inner/bottom boundary (r_i) is always assumed to be no-slip. In the case of only no-slip boundaries, both toroidal and poloidal components of the mass flux are zero at the boundaries, which corresponds to $C_n(r_i)W_{\ell mn} = 0 = C_n(r_o)Z_{\ell mn}$. Independently of the mechanical boundary being free or no-slip, both boundaries are assumed impenetrable and the poloidal mass flux, W, across them always vanishes.

Following Wicht and Christensen (2007), the equation for the free-slip boundary for both components of the mass flux implemented is

$$\begin{aligned} &\left[\frac{\partial^2 C_n(r_o)}{\partial r^2} - \left(\frac{1}{\rho}\frac{\partial \rho}{\partial r} + \frac{2}{r}\right)\frac{\partial C_n(r_o)}{\partial r}\right] W_{\ell mn} = 0 = \\ &= \left[\frac{\partial C_n(r_o)}{\partial r} - \left(\frac{1}{\rho}\frac{\partial \rho}{\partial r} + \frac{2}{r}\right) C_n(r_o)\right] Z_{\ell mn}\,. \end{aligned} \tag{2.64}$$

The top boundary of the shell r_o is assumed electrically insulating for a planet like a gas giant, thus the toroidal magnetic field cannot pass through the interface. Therefore the induction equation for the toroidal field must be replaced by a condition that sets this component of $\mathbf{B}$ to zero, as $C_n(r_o)A_{\ell mn} = 0$. The poloidal component B is matched to a potential field in the source-free outer region by using the equation $[\partial_r C_n(r_o) - \ell/r\, C_n(r_o)]\, B_{\ell mn} = 0$. The inner core is modelled as an electrical conductor (see section 2.8 below) and the induction equation Eq. 2.32 is additionally solved for a radial grid inside the inner core, which is assumed to be in solid-body rotation.

Finally, the entropy is fixed on both top and bottom boundaries, with a fixed contrast between them of $\Delta S = 1$. This is the assumption of heating from the bottom, thus the entropy contrast drives the thermal convection.

2.8 Present work - modelling strategy

The work carried out for this thesis is based on a set of parameters that is fixed (some exceptions will only be mentioned at the end of Chapter 3) and another set of parameters that will be varied. It is the analysis of these varied parameters that constitutes the focus of this study. The main purpose of the work described in this and the next Chapters is to approach a model for the interior of the gas giants by exploring the effects of variable properties, mainly density and electrical conductivity.

The model developed here covers from 0.2 to 0.99 of Jupiter's interior (aspect ratio $\eta = 0.2$). According to results on the interior composition of Jupiter, obtained from solving *ab initio* equations by Nettelmann et al. (2012), the existence of an inner core is poorly constrained, it lies between 0 and 10% of the planetary radius. The assumed η here suggests a bigger inner core of 20%, which still qualifies as a thick shell, when compared to geodynamo models. This will be shown in the results presented in the last section of Chapter 3.

The Prandtl number Pr measures the ratio between the diffusions of momentum and heat. Here this value is assumed to be 1.0 in the majority of the simulations.

The magnetic Prandtl number Pm represents the balance between the viscous and magnetic diffusivities. In the numerics, Pm is clearly overestimated, as Tab. 2.1 shows. It was reported by Christensen et al. (1999) that the minimum Pm for dynamo action is highly dependent on the Ekman number of the model and they found that the critical Pm decreases with E. They also found that a minimum magnetic Reynolds number of $Rm \approx 50$ is necessary to sustain dynamo action. Thus, when E is decreased, it is possible to use lower values of Pm in the models. The dependence of Pm on E scales as $Pm_{cr} = 450\, E^{3/4}$, where Pm_{cr} is the lower value of Pm at which Christensen and Aubert (2006) found dynamo action. No matter how big Rm is, if $Pm < Pm_{cr}(E)$, self-sustained dynamo action does not occur. However, even for $Pm > Pm_{cr}$, for the lower values of Pm the flow velocity must be stronger to achieve Rm_{cr}, i.e. the supercriticality (Ra/Ra_{cr}) of the system must be higher for dynamo action when both Pm and E are lower. In the models discussed in this work, Pm will typically be 5 or 10 for $E = 10^{-3}$, 2 for $E = 10^{-4}$, 1 for $E = 10^{-5}$, $5-10$ for $E = 3 \times 10^{-4}$ and $1-2$ for $E = 3 \times 10^{-5}$.

The parameters that will be varied systematically in the next Chapters are the Ekman number E, the Rayleigh number Ra and the number of density scale heights N_ρ. E will be in the range 10^{-3} – 10^{-5} to model different rotation rates, where the highest value is approaching a non-rotating regime. It has been possible to achieve lower values of Ekman number in numerical simulations ($\sim 10^{-7}$, Stellmach and Hansen 2004), but only at great computational costs, which is not appropriate for this work that is based on an extensive study of a parameter regime. Ra is considered between 3 to 50 times supercritical and N_ρ will vary between 0 (Boussinesq model) and 5 (a density ratio between the inner and outer boundaries of ~ 150).

The boundary conditions assumed here are simple and some are non-realistic for a model of a gas giant. Initial simulations were carried out assuming an electrically conducting inner core, which may be appropriate Jupiter if assuming that the rocky inner core is mainly composed of iron and thus electrically conducting. This is however still unknown. The magnetic field matches a diffusive solution at the inner boundary and a potential field at the outer boundary.

The entropy is fixed at constant values in both boundaries, with $\Delta S = 1$ in the reference state, decreasing outward. This corresponds to heating from the inner to the outer boundaries, which is not realistic for a model of a gas giant since Jupiter, for example, might not even have an inner core and if it does, it is only a rocky core that is not likely to be heating the fluid shell above (Nettelmann et al. 2012). Instead, the appropriate heating mode would be internal heating, but this is not addressed in this work.

The mechanical boundary conditions are considered no-slip at the assumed rocky inner boundary and free-slip at the top. The free-slip outer boundary is appropriate for modelling a gas giant and it allows for more complex dynamics, like the presence of two attractors and surface jets, as it will be demonstrated below (see also Gastine et al. 2012).

Chapter 2 describes the model implemented by Thomas Gastine in the MAGIC code by Johannes Wicht, namely the anelastic system of equations, the reference state and the numerical method. The first part of the results concerns models for the metallic region of Jupiter's interior alone and it is presented in Chapter 3, followed by the second part in Chapter 4 where the metallic and molecular envelope are coupled through a radially varying electrical conductivity profile. The latter Chapter, as well and the present section, were adapted from Duarte et al. (2013). Finally, in Chapter 5, previously developed scaling laws for numerical simulations are applied to the results from Chapters 3 and 4.

3 Constant electrical conductivity

Both density and electrical conductivity vary along radius, though only mildly in the metallic interior of a gas giant and much more significantly in the outer molecular envelope. For the first part of this work, the two effects will be separated to start by exploring the effects of background density stratification.

In contrast with the Boussinesq models of constant density, the target here is to take such gradients into account to understand what could be the scenario in the deep interior of high temperature and pressure of a gas giant, where the dynamo is generated. Thus only the deeper part of Jupiter's interior is simulated in this Chapter, while the electrical conductivity is kept constant.

3.1 Onset of convection in anelastic models

The critical values of Rayleigh number, frequency and wavenumber refer to the lowest Rayleigh number at which it is possible to initiate convection in a rotating spherical shell, i.e. the least amount of power necessary to add to the system to have a superadiabatic temperature gradient that promotes the instability that drives the convection needed to transport the excess heat that cannot be transferred by conduction. The linear code developed by Jones et al. (2009) is used in this section to obtain the critical values for the onset of convection in a rotating spherical shell, at Ekman numbers in the range $10^{-3}-3\times10^{-6}$, $Pr=1$, aspect ratio $\eta=0.2$ and different values of N_ρ (see Tab. 3.1).

The location of the convection cells is a natural function of N_ρ since the radial entropy gradient changes with density stratification, i.e. the region where the buoyancy gradient is steeper. For a typical constant density model (Boussinesq or $N_\rho=0$), the convection starts at the inner boundary, which also applies to increasing values of N_ρ, as long as the density stratification remains mild (below 2 density scale heights). At higher values of N_ρ, past 2, the onset is always found near the outer boundary instead. Thus there will be one value of N_ρ at which this shift of the most unstable layer between inner and outer happens (see Fig. 3.1 and next paragraph). This transition increases with decreasing Ekman number E, as does the wavenumber (Gastine and Wicht 2012). An interesting result of this feature is that very near the transitional N_ρ both layers can co-exist. We will come back to this point later, but first we would like to show the effects of density stratification alone.

Figure 3.1 shows the evolution of the convection in a rotating spherical shell, when the density gradient is increased. In the first three plots ($N_\rho = 0 - 2$) the convection stays attached to the inner boundary of the shell, where the combination of two factors determines its preferential location here: the buoyancy gradient and the curvature of the shell. The tangent cylinder is defined by an imaginary boundary parallel to the rotation

Table 3.1: Some values of critical Rayleigh number (Ra_{cr}) and critical wave number (m_{cr}) for different values of N_ρ at $\eta = 0.2$ and $Pr = 1$. The values listed were obtained with a modified version of the linear code by Jones et al. (2009).

Ekman	N_ρ	Ra_{cr}	m_{cr}
10^{-3}	0.0	7.582×10^4	2
10^{-3}	1.0	1.371×10^5	3
10^{-3}	2.0	2.282×10^5	3
10^{-3}	3.0	2.745×10^5	15
10^{-3}	4.0	3.197×10^5	18
10^{-3}	5.0	4.478×10^5	21
3×10^{-4}	0.0	2.635×10^5	3
3×10^{-4}	1.0	5.402×10^5	4
3×10^{-4}	2.0	9.376×10^5	4
3×10^{-4}	3.0	1.185×10^6	27
3×10^{-4}	4.0	1.254×10^6	31
3×10^{-4}	5.0	1.586×10^6	35
10^{-4}	0.0	8.706×10^5	4
10^{-4}	1.0	1.935×10^6	5
10^{-4}	2.0	3.455×10^6	6
10^{-4}	3.0	4.648×10^6	43
10^{-4}	4.0	4.569×10^6	49
10^{-4}	5.0	5.372×10^6	55
10^{-4}	5.5	6.172×10^6	58
10^{-4}	6.0	7.332×10^6	61
3×10^{-5}	0.0	3.392×10^6	6
3×10^{-5}	1.0	8.024×10^6	7
3×10^{-5}	2.0	1.465×10^7	8
3×10^{-5}	3.0	2.146×10^7	70
3×10^{-5}	4.0	1.971×10^7	80
3×10^{-5}	5.0	2.168×10^7	91
10^{-5}	0.0	1.207×10^7	7
10^{-5}	1.0	3.012×10^7	9
10^{-5}	2.0	5.582×10^7	11
10^{-5}	3.0	8.874×10^7	108
10^{-5}	4.0	1.001×10^8	110
10^{-5}	5.0	1.155×10^8	128
3×10^{-6}	0.0	5.021×10^7	11
3×10^{-6}	1.0	1.304×10^8	13
3×10^{-6}	2.0	2.453×10^8	15
3×10^{-6}	2.5	3.322×10^8	15
3×10^{-6}	3.0	4.268×10^8	166

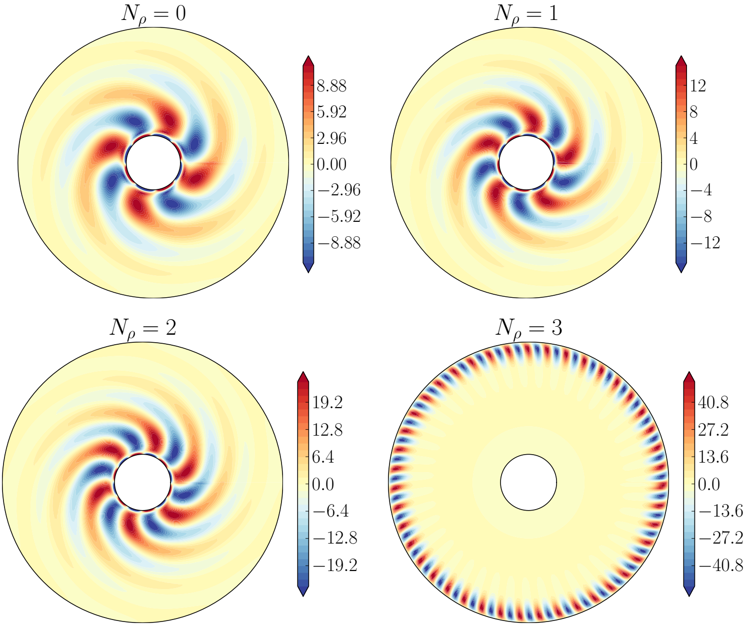

Figure 3.1: Contours of z-vorticity at the onset of convection in a rotating spherical shell of aspect ratio $\eta = 0.2$ and Ekman number $E = 10^{-4}$. The number of density scale heights N_ρ is 0 (Boussinesq), 1, 2 and 3 from left to right and top to bottom.

axis, that touches the surface of the inner core, i.e., a cylinder of radius $r_{TC} = 0.2\,r_o$. Just outside of the tangent cylinder (TC) is where the convection columns can be longer and, due to the thickness of the shell, it is also where the curvature of the boundaries of the sphere is smaller, with an angle of only 11.5°/0.2 rad, which is around 12% of the inclination at r_o. The convection thus tends to be attached to the inner boundary with increasing N_ρ for as long as possible, even though the buoyancy gradient is becoming weaker there and stronger at the outer boundary. However, the most unstable wavenumber increases with N_ρ, which can be seen in Fig. 3.1 as well. In the last panel of Fig. 3.1, for $N_\rho = 3$, the convection has shifted to the outer boundary and has much higher wavenumber. This transition occurs suddenly, unlike the behaviour for a thin shell reported by Gastine and Wicht (2012) which shows a gradual movement of the location of the convection with increasing N_ρ. This can be understood since in their case there is already a significant curvature at the tangent cylinder, of 36.9° which is around 41% of the inclination at r_o.

The phenomenon of two-layer convection in the thick shell simulations studied here is also present in one figure of Jones et al. (2009) for parameters $E = 2\times10^{-4}$, $\eta = 0.5$ and $Pr = 0.1$, though they did not discuss it. They proposed scaling laws for the dependence of the critical Rayleigh number, wavenumber m and drift frequency f of the convection cells on the Ekman number E. They report that in the limit of $E \to 0$, the scaling relations are $Ra_{cr} \propto E^{4/3}$, $m_{cr} \propto E^{1/3}$ and $f_{cr} \propto E^{1/3}$.

In Fig. 3.2, the quantities Ra_{cr}, m_{cr} and f_{cr} are plotted with the respective factor ($E^{4/3}$ for Ra, $E^{2/3}$ for f and $E^{1/3}$ for m) against the Ekman number. This plots should be basically a horizontal line (or tend to one when $E \to 0$) if the results obtained here for the critical values prove to follow the scaling laws of Jones et al. (2009). A tendency to approach the scaling law when $E \to 0$ appears to be true in these plots, though actually reaching the asymptotic regime would require $E < 3 \times 10^{-6}$. According to the plots of Fig. 3.2 for $N_\rho = 0 - 2$, the most unstable mode is always attached to the inner boundary. These cases correspond to the bottom (top) parallel lines in the middle (bottom) plots of Fig. 3.2. Jumping to $N_\rho = 3$ (magenta lines with upside triangles) for now, the convection starts attached to the outer boundary instead. This can also be seen in the middle and bottom plots where the $N_\rho = 3$ line belongs to the other group of lines of higher m_{cr} and lower f_{cr}. The conclusion so far is that the cases of $N_\rho = 0 - 2$ belong to the regime where the convection happens first in the inner layer and $N_\rho = 3$ belongs to the other regime, with convection in the outer layer. The intermediate values of $N_\rho = 2.5$ and $N_\rho = 2.8$ have the particularity of showing the transition between these two regimes with a clean jump in critical wavenumber, which happens around $E = 2.6 \times 10^{-4}$ and $E = 1.4 \times 10^{-5}$, respectively (see top panel of Fig. 3.2). The transitional N_ρ between the two locations of convection increases with decreasing Ekman number.

The top plot of Fig. 3.2 is the scaling for the critical value of Rayleigh number, which is the most significant parameter of the three for this work, since Ra is a direct input of the MHD equations implemented in the code and it will also be used for analysis of the output results, mostly in the form of the model's supercriticality (Ra/Ra_{cr}).

Figure 3.3 shows another way to represent graphically this transition, where for each pair of (N_ρ, E), a dot is shown with a colour that quantifies its most critical value of wavenumber m_{cr} (adjacent colorbar). Though this plot is not very specific about actual values, the point here was solely to identify the transition, which is described by a simple power law obtained from a least squares polynomial fit to the estimated transition points $(N_{\rho\, tr}, E_{tr})$ (dashed line and equation above it). The sudden jump from blue to red colours clearly depicts this transition between the two convective layers and it shows which of these layers is more unstable for each pair (N_ρ, E).

In this work, the parameters are similar to Gastine and Wicht (2012)'s, where the onset of convection gradually moves outward with increasing N_ρ, but for a thicker shell of $\eta = 0.2$. This suggests that the presence of double layer convection possibly depends on the aspect ratio and maybe on the Prandtl number, since Jones et al. (2009) also observed this sharp transition, but only at $Pr = 0.1$, $\eta = 0.5$ and $E = 2 \times 10^{-4}$. The purpose of this section is not to find a parameter regime where double layer convection exists, but merely to report its presence in more detail.

Figure 3.4 shows the double layer convection at values of N_ρ where the two layers co-exist at various Ekman numbers and slightly supercritical Rayleigh numbers. Due to a non-linear relation between them, the wavenumbers of inner and outer layers are multiples of each other. The outer mode is not necessarily the most unstable mode here, but it has the wavenumber $m_o = a\, m_i$ which is closest to $m_{cr,o}$, where a is the proportionality constant. This is mostly clear at higher Ekman numbers, because of the smaller wavenumber and thus longer radial extent of the convection cells (see, for example, the $E = 10^{-3}$ plot in

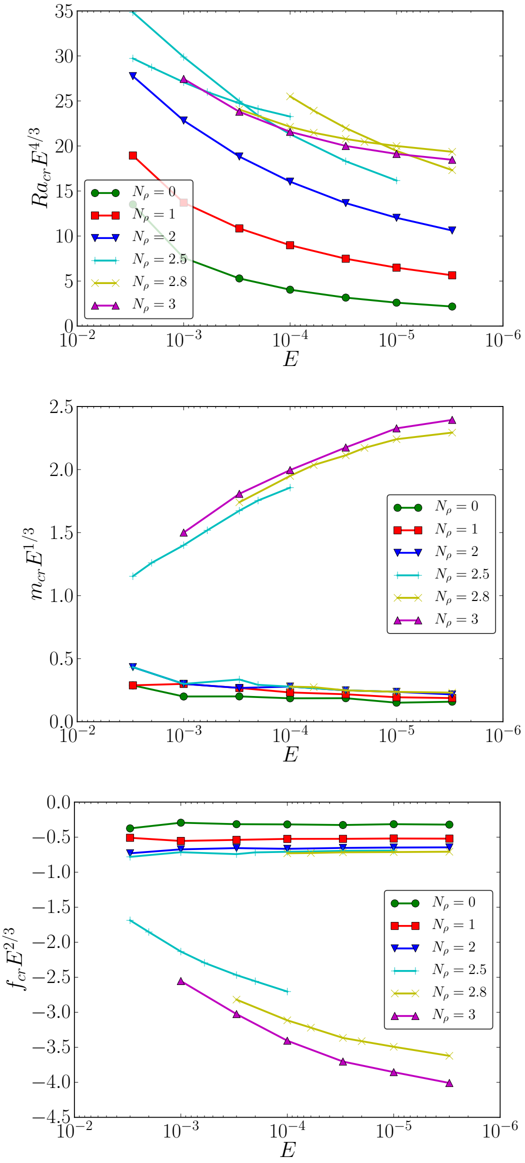

Figure 3.2: Plots based on the scaling suggested by Jones et al. (2009), here for aspect ratio $\eta = 0.2$, gravity proportional to the radius, mixed boundary conditions and $Pr = 1.0$. The scaling laws are $Ra_{cr} \propto E^{-4/3}$, $m_{cr} \propto E^{-1/3}$ and $f_{cr} \propto E^{-2/3}$.

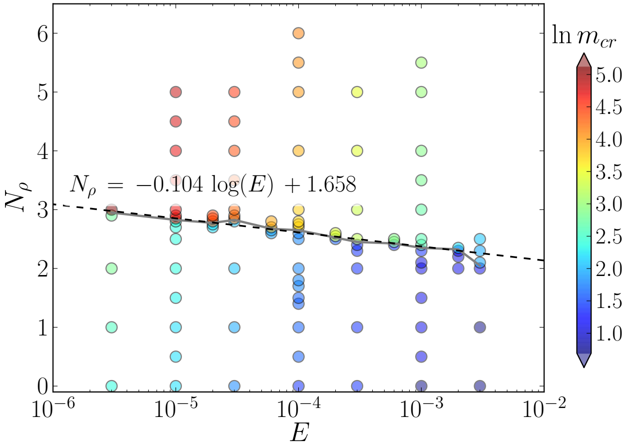

Figure 3.3: Regime diagram of the critical wavenumber m_{cr} for each pair of parameters N_ρ and E. The magnitude of m_{cr} is indicated by the colorbar on the right side of the plot. The dashed line is the polynomial least squares fit obtained from the points gathered by the grey line. The equation for the fit is $N_\rho = -0.104 \log E + 1.658$.

Fig. 3.4). The six panels in Fig. 3.4 manifest simultaneously the wavenumber pairs of 4/12, 4/24, 6/42, 8/64, 11/99 and 16/160 for the Ekman numbers 10^{-3}, 3×10^{-4}, 10^{-4}, 3×10^{-5}, 10^{-5} and 3×10^{-6}, respectively.

3.2 Nonlinear convection

The force that is directly affected by a variable density with radius is the buoyancy force. When the density starts to decrease toward the outer boundary, the fluid is convected to the lower density part of the shell. The steep density (thus temperature) gradient close to the outer boundary, given by the polytropic background state, translates into a stronger buoyancy force closer to the outer part, where the biggest part of the density contrast is. In a constant density environment, the convection would onset at the inner boundary to guarantee conservation of the heat transferred from the inner core boundary, due to the deficit in the transfer by conduction merely because of the smaller surface area.

Figure 3.5 shows how the convection changes with density stratification in non-magnetic turbulent simulations through contour plots of z-vorticity in the equatorial region (vorticity with axis perpendicular to the disc shown). Even though these models are now far from the onset of convection of Fig. 3.1, clearly the differences in the fluid dynamics of the system reported in the previous section for the different values of N_ρ remain.

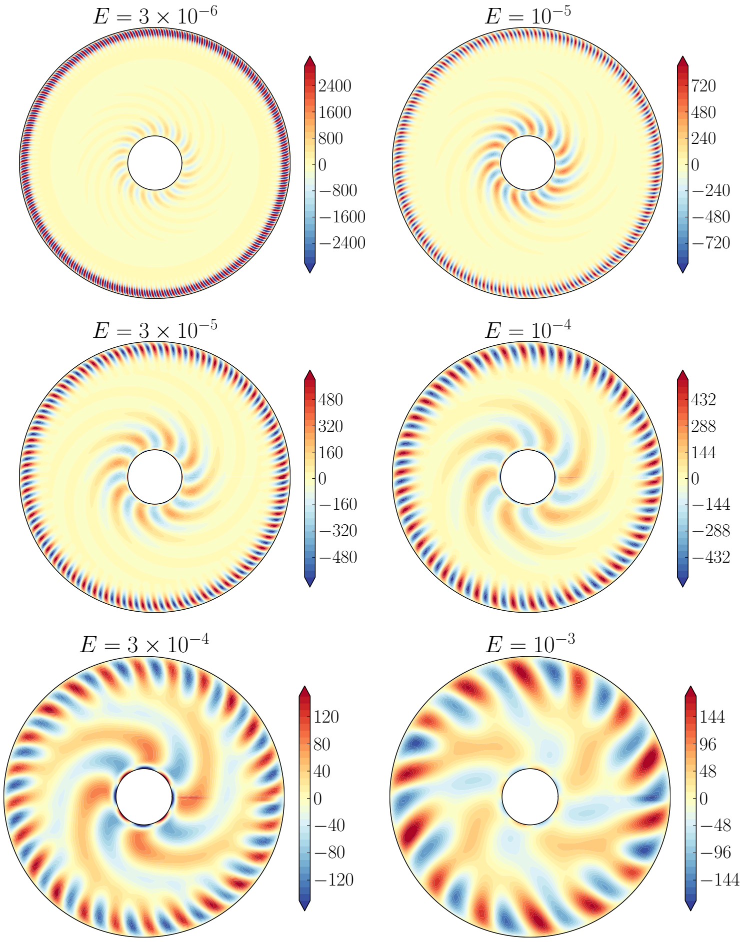

Figure 3.4: Six cases close to the transition of N_ρ between the two convective layers, where it is possible to have both simultaneously. The Ekman number increases from left to right and top to bottom, while N_ρ decreases (see Fig. 3.3).

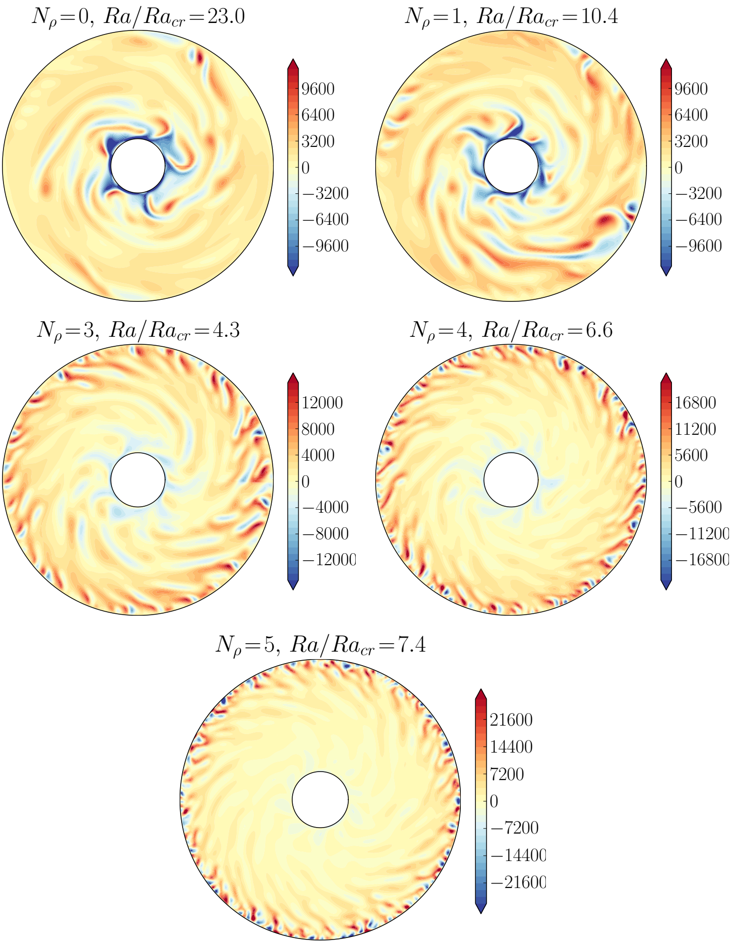

Figure 3.5: Contours of z-vorticity in a rotating spherical shell of aspect ratio $\eta = 0.2$ and Ekman number $E = 10^{-4}$. The number of density scale heights N_ρ is 0 (Boussinesq), 1, 3, 4 and 5 from left to right and top to bottom.

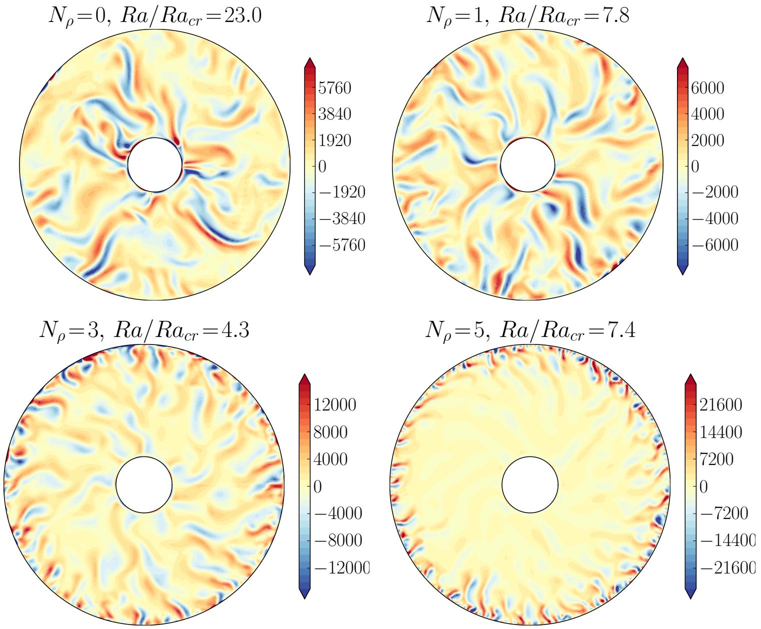

Figure 3.6: Contours of z-vorticity in a rotating spherical shell of aspect ratio $\eta=0.2$ and Ekman number $E=10^{-4}$. The number of density scale heights N_ρ is 0 (Boussinesq), 1, 3 and 5 from left to right and top to bottom.

3.3 Dynamo action

This and the following sections focus on models with Ekman number $E = 10^{-4}$. The induction equation will also be solved from now on, to explore the effect of the changes in the dynamo mechanism due to the density contrast in a fluid shell. Figure 3.6, is similar to Fig. 3.5 but it shows a magnetic simulation where the full MHD system of equations is solved. The difference between panels is the increasing N_ρ from left to right and top to bottom. As before, the main location of the convective motions moves from being close to the inner to being close to the outer boundaries. The difference to Fig. 3.5 is unrelated to the density stratification and it is the fact that models with a magnetic field have much less tilted z-vorticity structures. This is due to the existence of one more force in Fig. 3.6 entering the dynamics: the Lorentz force. This force limits significantly the amplitude of the zonal flows and the convection cells are therefore less tilted and more elongated in the radial direction.

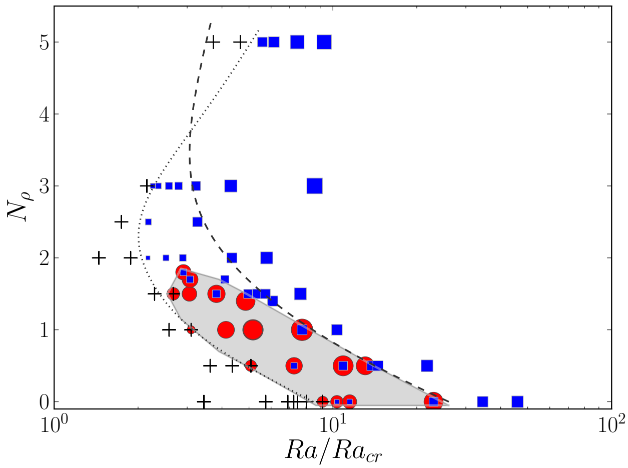

Figure 3.7: Number of density scale heights N_ρ versus supercriticality of the system Ra/Ra_{cr}, for Ekman number 10^{-4} and Prandtl numbers $Pr=1$, $Pm=2$. The red circles correspond to dipole-dominated magnetic fields, the blue squares are multipolar fields and the crosses represent failed dynamos. The shaded region corresponds to the window in the parameter space where dipolar solutions (red circles) exist. The dashed line traces the transition between rotation-dominated and inertia-dominated regimes, at $Ro_\ell = 0.08$. The dotted line traces the onset of dynamo action.

3.3.1 Regime diagrams and bistability

Starting with the weakly stratified cases, the features observed in our models are similar to former published studies with absence of a density contrast. For $N_\rho < 2$, two solutions exist for the same exact parameters, depending on the initial condition used for the magnetic field. When the initial solution is dominated by a strong axisymmetric dipolar component, the final solution of the model remains as a geodynamo-type of solution, but when the starting magnetic field has a weak dipole component compared to the other modes, the dipole never develops and the resulting magnetic field either remains multipolar and weak or the dynamo decays when the Rayleigh number is too low. The latter case corresponds to subcritical dynamo action. The results are summarized the regime diagrams of Figs. 3.7 and 3.8.

Starting with the description and then analysis of Fig. 3.7, the three kinds of symbols (red circles, blue squares and black crosses) represent the dominant types of dynamo modes (axisymmetric dipole, multipole and decaying, respectively). The dipolar solutions are selected with a minimum f_{dip} (Eq. 2.52) of 2.0 and the values below this threshold are considered multipoles (non-dipolar). The dashed line marks a constant value of the local Rossby number (~ 0.08, the same dashed line in Fig. 3.8, discussed below), the dotted line represents the onset of dynamo action and the shaded grey area is simply another indication of the location of dipole-dominated solutions, in addition to the red circles.

Thus everything outside of this area is either a multipolar solution or a failed dynamo. The size of the circles and squares is scaled by the local Elsasser number defined in Chapter 2 (Eq. 2.54) to provide information about the strength of the resulting magnetic field.

When N_ρ increases, the dashed line of constant Ro_ℓ indicates that the supercriticality of the system Ra/Ra_{cr} decreases up to $N_\rho \sim 3$ and it increases when $N_\rho > 3$. As seen before, the main location of the convection in the simulated spherical shell moves from the inner to the outer boundaries, between $N_\rho = 2$ and $N_\rho = 3$. At $N_\rho \geq 3$, the convection is not only attached to the outer boundary, but also the convection cells move to radii even closer to the outer radius with increasing N_ρ, along with a larger wavenumber (Fig. 3.1).

On the left side of this diagram, the Rayleigh number for onset of dynamo action (crosses) also depends on N_ρ. It starts by becoming lower with increasing N_ρ and then it increases for $N_\rho \geq 2.5$. This suggests that up to $N_\rho \sim 2.5$, the magnetic Reynolds number necessary for dynamo action Rm_{cr} decreases with growing N_ρ, together with a subtle decrease of the amplitude of the flow averaged in the whole shell, Ro. To illustrate this, the cases represented in Fig. 3.7 closest to the crosses of $N_\rho = 0, 0.5, 1, 1.5, 2$ have, respectively, $Rm = 124, 104, 68, 86, 88$ and $Ro = 0.007, 0.005, 0.003, 0.004, 0.004$. However at $N_\rho \geq 2.5$, the flow amplitude increases from $Ro = 0.007$ at $N_\rho = 2.5$ to $Ro = 0.02$ at $N_\rho = 5$, and so does Rm_{cr}, from 115 to 313 for the same values of N_ρ. The two "boundaries", of failed dynamos on the left (dotted line) and $Ro_\ell = 0.08 = Ro_{\ell\, cr}$ on the right (dashed line), appear to be roughly parallel until $N_\rho = 2.5$, after which the left border changes direction and eventually crosses the $Ro_{\ell\, cr} = 0.08$ line around $N_\rho = 4$. The reason for this behaviour at higher values of N_ρ may be the increasingly more confined convection close to the outer boundary, where the flow amplitude is very high and enough to guarantee large values of Ro_ℓ, though its relative absence in the bulk of the shell limits the possibility of having dynamo action.

The shaded region of this plot incorporates all of the dipole-dominated solutions (red circles), but most of these cases have another possible solution, shown by either a cross or a blue square overlapping the red circle. The cross means that these are subcritical dynamos, close to the onset, where dynamo action is only self-sustained when the initial magnetic field is strong enough. Most of the other cases have two possible dynamo solutions for the same exact parameters. These two attractors differ in both magnetic field morphology and strength (size of the symbols).

Figure 3.8 shows the dipolarity f_{dip} of the magnetic field (i.e. the relative amplitude of the energy in the axisymmetric dipolar mode) against the local Rossby number Ro_ℓ, introduced in Chapter 2. The dashed line represents a limit where the effect of inertia becomes significant in the force balance and severely reduces the effectiveness of the convection columns to produce helical flow motions. As a consequent, the dynamos beyond $Ro_{\ell\, cr} = 0.08$ are dominated by smaller magnetic scales instead of a strong dipolar mode (Christensen and Aubert 2006). This dashed line is the same as in Fig. 3.7. The existence of the two attractors in the shaded area of Fig. 3.7, on the left side of the dashed line, can also be seen in Fig. 3.8 in two branches: an upper branch that corresponds to the red circles and a lower branch that corresponds to the blue squares (Busse and Simitev 2006, Sasaki et al. 2011, Schrinner et al. 2012, all found this behaviour in models of $N_\rho = 0$). Most of the solutions that exist in the branch of higher dipolarity ($f_{dip} \sim 0.8$) below $Ro_{\ell\, cr}$, also have a solution in the multipolar branch, which can be seen clearly in Fig. 3.7 from the

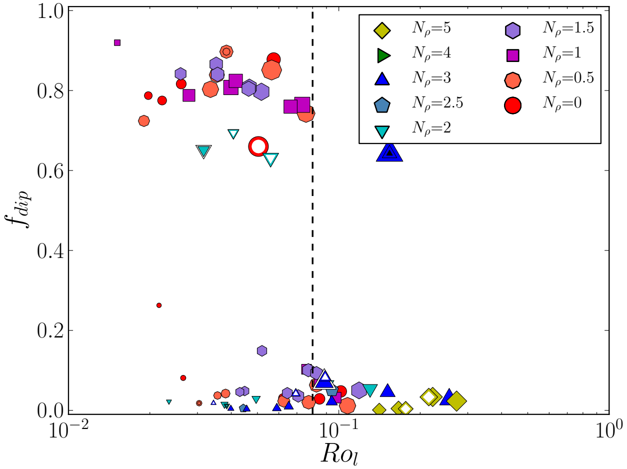

Figure 3.8: Dipolarity versus local Rossby number for Ekman number 10^{-4}. The symbols shapes and colours correspondence is indicated in the legend and the open symbols have a different mechanical condition at the outer boundary, no-slip. The typical Prandtl numbers are $Pr = 1$ and $Pm = 2$. The symbols with extra outer rim have $Pm > 2$ and inner have $Pm < 2$. The symbol with an inner black triangle has $Pr = 0.1$.

superposition of squares (multipoles) over circles (dipoles) in the shaded region. Subcriticality is another feature illustrated by both figures, since in Fig. 3.8 the lower multipolar branch starts at higher values of Ro_ℓ (or Ra) than the upper dipolar branch, and in Fig. 3.7 there is also overlapping of crosses (non-magnetic) and circles (dipoles).

An undeniable difference between the two branches of $Ro_\ell \leq Ro_{\ell\,cr}$, no matter the value of N_ρ, is then the size of the symbols, scaled by the local Elsasser number Λ_ℓ, and in the dipole-dominated solutions, the magnetic field is around three times larger than the non-dipolar attractors in the lower branch of Fig. 3.8. This suggests a different force balance. At $N_\rho < 1.8$, each of the two attractors belongs to one of the two branches. If the outer boundary of the model was no-slip, for a model starting as a low amplitude magnetic field, the convection columns formed would be relaxed by the viscosity of the outer boundary and the amplitude of the zonal flow would be severely limited. This still happens with free-slip boundaries, if the simulation starts as a magnetic field with significant amplitude. When it does not, the zonal flow is allowed to grow fast, maintained by the Reynolds stresses (product of the cylindrical velocity components ϕ and s of the convection columns, where s is the radial direction), since the only viscosity available to brake it comes from the bulk, which is clearly too small. As result, the z-independent azimuthal flow (zonal flow) dominates. This means that the lower branch contains solutions that follow a geostrophic balance where the Coriolis force is balanced by pressure gradients in the horizontal component of the momentum equation, while the upper branch displays models under a magnetostrophic balance, where the Lorentz force enters the force bal-

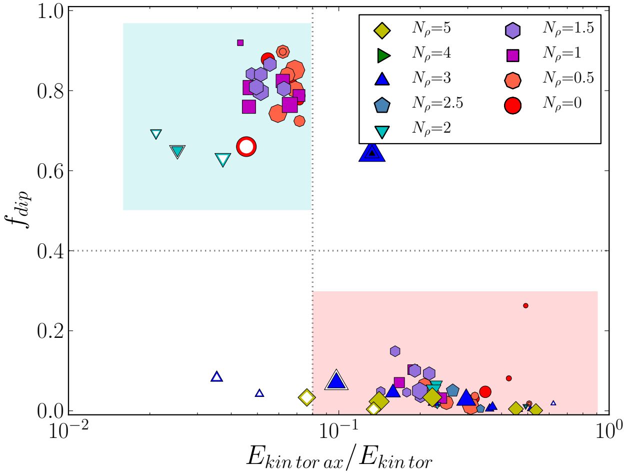

Figure 3.9: Dipolarity versus the ratio between the axisymmetric part of the toroidal kinetic energy and the the total toroidal kinetic energy, for Ekman number 10^{-4}. The symbols have the same meaning as in Fig. 3.8.

ance with the same order as the Coriolis force. This conflicting behaviour between strong zonal flow and strong magnetic field amplitudes is summarized in Fig. 3.9. In this figure, the data fall in either one of the two shaded rectangular areas corresponding to the two branches in Fig. 3.8.

Since the lower branch is dominated by the strong zonal winds which increase toward the outer boundary, it is natural to expect a considerable generation of toroidal magnetic field by the differential rotation through Ω-effect. This can be seen in the middle panels of both top and bottom rows of Fig. 3.10 where the contours represent the term of the azimuthal component of the induction equation responsible for generation of B_ϕ through shearing by the differential rotation (contours in the left panels of Fig. 3.10). This term of the induction equation is what we call here the Ω-effect (Eq. 2.38). The lines of the middle panels show isocontours of B_ϕ, which match very well the Ω-effect (colours) in the multipolar case (bottom row), but not in the dipolar case (top row), as expected. The left panels in both rows of Fig. 3.10 show the contours of v_ϕ that is indeed predominantly geostrophic for the multipolar case in the bottom row and larger amplitude than the dipolar case (colorbars of the left panels). The dipolar branch shows a weak zonal flow (top left panel) that arises from the thermal wind balance due to latitudinal temperature gradients.

Figure 3.11 displays the kinetic and magnetic energy spectra of both attractors in Fig. 3.10. The kinetic energy does not show significant difference in the smaller scales or in the shape of the spectra, though overall the kinetic energy of the dipolar case is slightly lower than the multipolar. The magnetic spectra exhibits a pronounced difference at $\ell = 1$ between the two cases. In the dipolar case (red line), this is the component with the higher

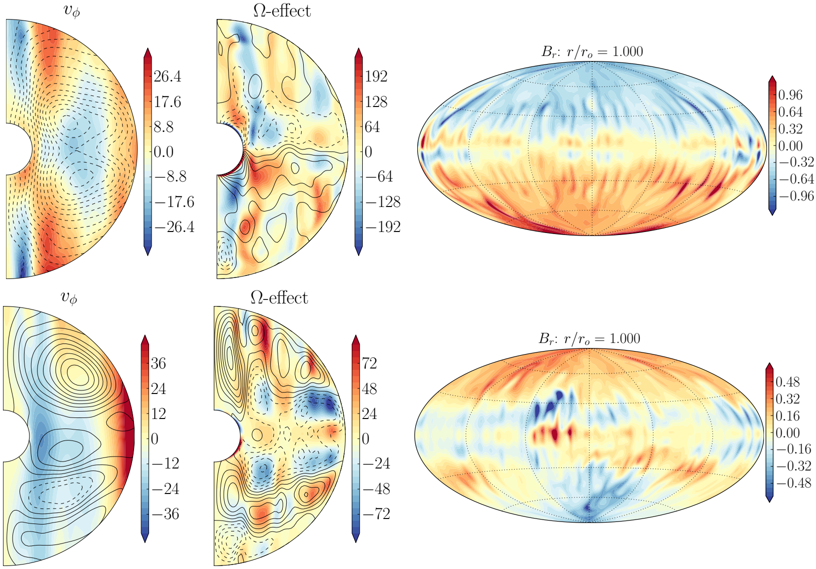

Figure 3.10: An example of bistability at $N_\rho = 1.5$, the top plots belong to the attractor in the dipolar branch and the bottom to the attractor in the multipolar branch. Both top and bottom rows display three plots each, from left to right: contours of axisymmetric azimuthal velocity with lines of poloidal magnetic field; contours of the azimuthal component of the induction equation responsible for the Ω-effect with lines of toroidal magnetic field; radial component of the magnetic field at the surface of the simulated shell. All images are snapshots.

amount of energy, almost one order of magnitude larger than the following components ℓ. The spectrum of the multipolar case is fairly similar, except for the low energy in the $\ell = 1$ mode (around one order of magnitude less than in the dipole). Note specially that this mode has less energy than the quadrupolar ($\ell = 2$) and octupolar ($\ell = 3$) modes. This is also reflected in the different surface magnetic fields of the right panels of Fig. 3.10.

Before moving on to the next section, notice the fact that the top of the shaded area in Fig. 3.7 is not flat, but instead $Ro_{\ell\,cr} < 0.08$ for N_ρ in the range of $1.5-2$. These values are increasingly smaller than the value of the dashed line for higher N_ρ's. At values of density stratification in this range, the dynamo solutions manifest strong sensibility to small changes in the parameters. This aspect is most evident at $N_\rho = 2$, where these changes allow changing the solution back to a dipole-dominated magnetic field. This was done by altering the mechanical boundary condition at the top (r_o) to no-slip and the simple absence of the surface zonal flow keeps the model in the dipolar regime for a slightly higher N_ρ than with a free-slip boundary. This can be observed in the open symbols of Fig. 3.8 that correspond to such modification of the upper boundary condition, where the dipolarity is recovered for $N_\rho = 2$ due to its location close to the limit of the

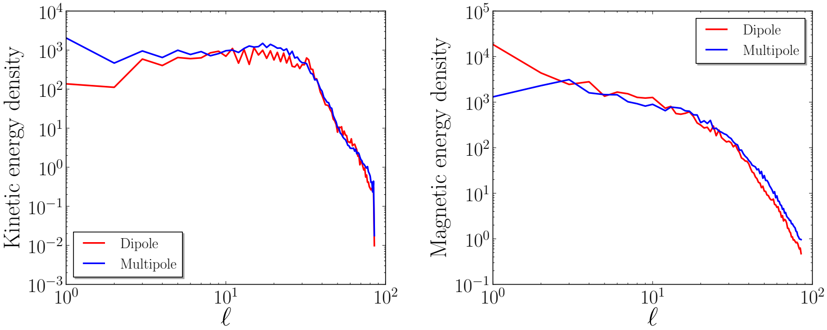

Figure 3.11: Magnetic and kinetic energy spectra of the two attractors from Fig. 3.10.

dipolarity window (shaded area in Fig. 3.7), but not at higher values of N_ρ. Another idea to switch a solution of $N_\rho = 2$ to a dipole was suggested by Simitev and Busse (2009) and partially tested here by increasing only *Pm* at $N_\rho = 2$, which successfully changed the dynamo solution.

3.3.2 Dependence on stratification

At $Ro_\ell \geq Ro_{\ell\,cr}$, all cases for any value of N_ρ show an amplitude of magnetic field comparable to the dipolar branch. These cases might then be back on the magnetostrophic force balance due to the stronger convection motions that develop in the entire spherical shell at these higher values of *Ra* (Christensen and Aubert 2006).

The remaining cases at $Ro_\ell \leq Ro_{\ell\,cr}$ but for $N_\rho \geq 2$ also belong to the lower multipolar branch and show no difference from the multipolar attractor at $N_\rho < 2$ in Figs. 3.7 and 3.8. But there is a different reason for their multipolar field morphology and for the absence of a dipolar branch. It is well-established now that a dipolar-dominated dynamo is usually an α^2-dynamo. As a reminder, the α-effect arises due to the presence of helical flows, a direct consequence of rotation, generated from the combination of the columnar convection and the non-axisymmetric meridional circulation. The axisymmetric helicity of models at different values of N_ρ is shown in Fig. 3.12. Its location follows naturally the main location of the convection columns, which becomes confined in a thin region around the equator and close to the outer boundary at $N_\rho \geq 2$ (right panel of Fig. 3.12, for $N_\rho = 3$). It was shown by Ruzmaikin et al. (1988) and Bassom et al. (2005) that in mean-field models such confinement of the helicity promotes a non-axisymmetric magnetic field of low critical wavenumber, typically in the range $m = 1-3$. Such pattern is observed in the right bottom panel of Fig. 3.13 of the surface radial component of the magnetic field for $N_\rho = 3$. The preference for these non-axisymmetric modes at higher values of N_ρ is also emphasized by the models of $N_\rho = 3$ in Fig. 3.8 with an upper no-slip boundary. These cases remain multipolar even in the absence of the strong zonal flow promoted at the surface in the free-slip models. In the leftmost plot of the bottom row, the flow is

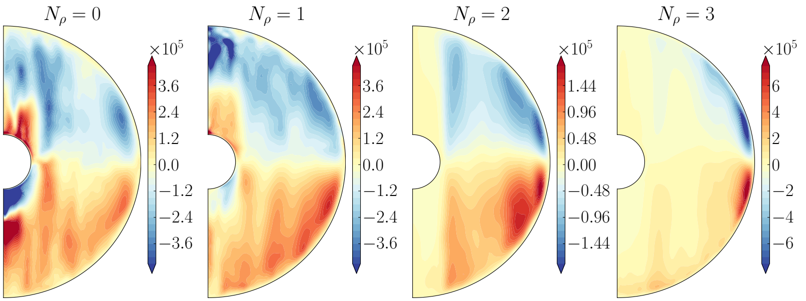

Figure 3.12: Contours of flow helicity $\overline{\mathbf{u}' \cdot \nabla \times \mathbf{u}'}$ in a rotating spherical shell of aspect ratio $\eta = 0.2$ and Ekman number $E = 10^{-4}$. The number of density scale heights N_ρ is 0 (Boussinesq), 1, 2 and 3 from left to right.

prominently geostrophic like the multipolar attractor at milder density stratification.

In Fig. 3.14, the magnetic spectra of two cases at different density stratifications ($N_\rho < 2$ and $N_\rho \geq 2$) are displayed. The Boussineq model is donimated by the dipole component (red line, case from the top row of Fig. 3.13) and the $N_\rho = 3$ model is multipolar (blue line, case from the bottom row of Fig. 3.13). Once more, there are a few striking differences between the two spectra. On the left panel, where the magnetic energy is plotted against degree ℓ, there is a lack of energy in the dipole mode of the multipolar model (blue line) that is considerably lower than the smaller scales $\ell > 10$, while the dipolar model has a clear peak of magnetic energy in the dipole mode (red line). On the right panel, the magnetic energy is plotted against order m, which shows the dominance of the $m = 0$ mode in the dipolar dynamo (red line), while the multipolar dynamo shows relatively high energy in the $m = 1$ and $m = 2$ modes and in the smaller scales $m > 10$. The stronger degree of geostrophy in the flow of $N_\rho \geq 2$ can be speculated to be a consequence of the absence of an axisymmetric dipolar component that would disrupt the zonal flow promoted by the stress-free boundaries, which turns out to be a similar effect as in the multipolar attractors at $N_\rho < 2$ when the flow also grows as a consequence of a weak non-dipolar starting field. Once the zonal flow is allowed to develop, it tends to prevent the (re)generation of a dipolar field. This confirms and concludes the discussion of the previous paragraphs, by placing the strongly stratified models in the multipolar and weaker field branch, because in both bases, the MHD equations are dominated by a strong differential rotation, though at high N_ρ it is "helped" by the preferential generation of non-axisymmetric modes, while at low N_ρ it is merely a consequence of the initial magnetic field condition applied.

3.3.3 Dynamo waves

All the cases that belong to the multipolar branch have significant contributions of Ω-effect to the induction process which makes them a dynamo of either $\alpha^2\Omega$ or $\alpha\Omega$ type. These cases also show a wave-type behaviour, known as dynamo waves or Parker waves. Similar phenomena were found for Boussinesq simulations by Goudard and Dormy (2008),

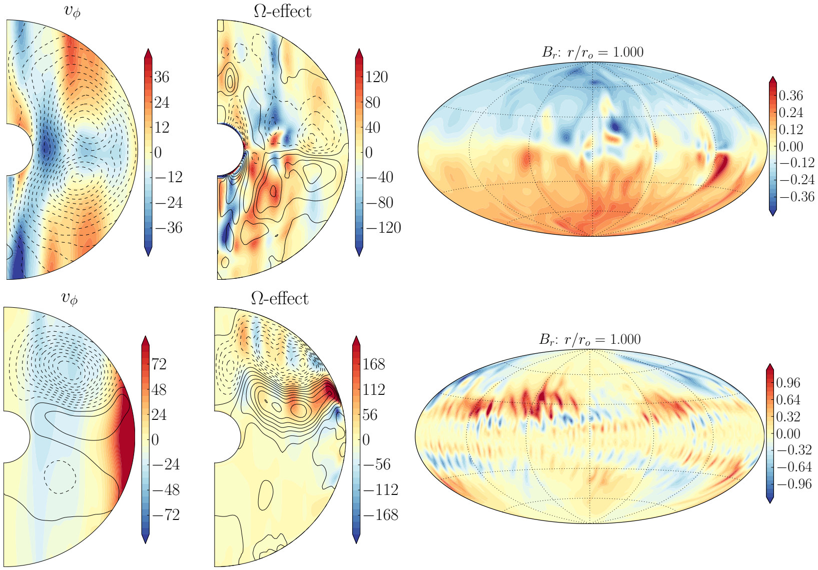

Figure 3.13: Two examples at different values of N_ρ, the top row shows a Boussinesq simulation in the dipolar branch and the bottom a $N_\rho = 3$ case on the multipolar branch. The panels are, from left to right: contours of axisymmetric azimuthal velocity with field lines of the axisymmetric poloidal magnetic field; contours of the axisymmetric azimuthal component of the induction equation responsible for the Ω−effect with lines of toroidal magnetic field; radial component of the magnetic field at the surface of the simulated shell.

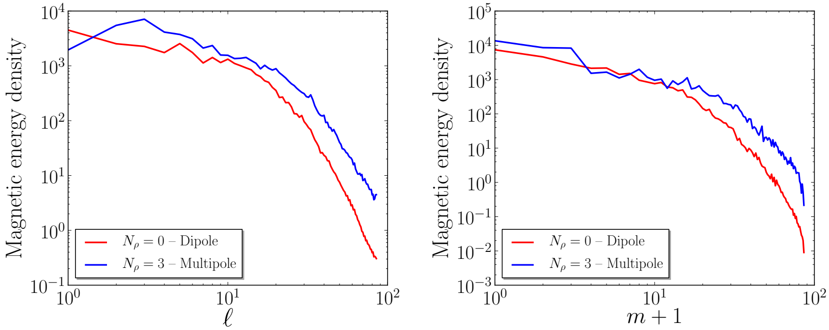

Figure 3.14: Magnetic energy spectra of the two cases from Fig. 3.13, versus the degree ℓ on the left and the order m on the right.

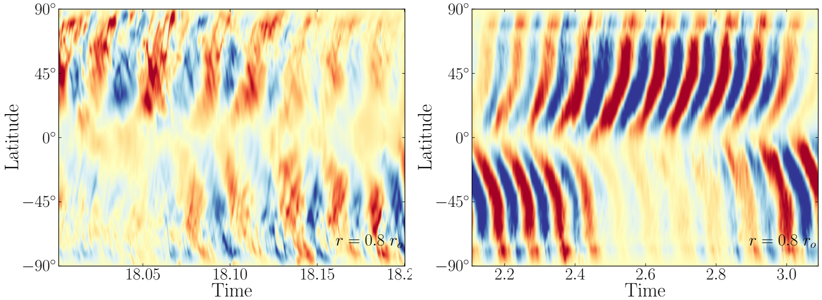

Figure 3.15: Time evolution of the azimuthally-averaged axisymmetric toroidal field component of the magnetic field at a depth of $r = 0.8\,r_o$. The time is given in viscous diffusion times. The left panel corresponds to a Boussinesq simulation and the right to a $N_\rho = 3$ model.

Schrinner et al. (2011) and Simitev and Busse (2012). Figure 3.15 shows this wave-like character in the azimuthal component of the magnetic field at 80% of the outer radius for $N_\rho = 3$ and $N_\rho = 0$, respectively. The wave is related to the strong toroidal field generated by the differential rotation present in these models. The direction in which the wave travels is directly associated to the direction of the gradient of angular velocity (Yoshimura 1975). Since the angular velocity decreases toward the inner boundary, the wave travels poleward. Due to the α-effect acting on the toroidal field to generate poloidal, the signature of the dynamo wave is also seen in B_r.

There is a tendency for a stronger amplitude of the field in one hemisphere, even though the motion of the wave is present in both. This can be seen not only in the panels of Fig. 3.15, but also in Fig. 3.16 where a longer time series of around four magnetic diffusion times is displayed. This illustrates how the activity switches from the northern to the southern hemisphere in a stochastic fashion.

Figure 3.17 shows the movement of the toroidal field patches inside the spherical shell. They form in the equatorial region and move to higher latitudes at the same time that another patch with opposite polarity appears at the equator and grows, pushing the first patch further away and poleward. These patches have their largest amplitude around ±40° of latitude. Between ±40° and ±75° of latitude, their amplitude decreases until the patch vanishes near the boundary of the tangent cylinder, which seems to stop the patches from reaching the poles.

It is possible to derive a dispersion relation, and this is done here using a mean-field formalism (Busse and Simitev 2006, Schrinner et al. 2011, Gastine et al. 2012). First it is assumed that both the magnetic field and the velocity are axisymmetric, i.e. independent of ϕ. Then the magnetic field $\mathbf{B}$ and the flow velocity $\mathbf{u}$ may be reduced to their axisymmetric parts, denoted here by the overbars,

$$\begin{aligned} \mathbf{B} = \mathbf{B}_\mathrm{P} + \mathbf{B}_\mathrm{T} &\xrightarrow{\partial_\phi = 0} \overline{\mathbf{B}} = \nabla \times (A\,\mathbf{e}_\phi) + C\,\mathbf{e}_\phi \\ \mathbf{u} = \mathbf{u}_\mathrm{P} + \mathbf{u}_\mathrm{T} &\xrightarrow{\partial_\phi = 0} \overline{\mathbf{u}} = u\,\mathbf{e}_\phi, \end{aligned} \tag{3.1}$$

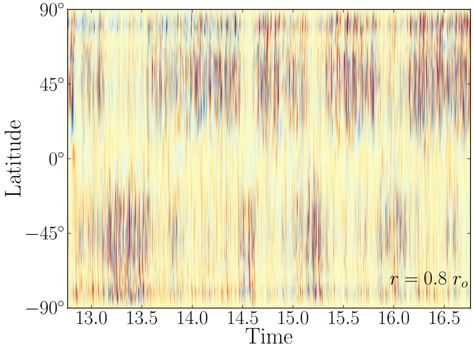

Figure 3.16: A longer time evolution of the azimuthally-averaged toroidal component of the magnetic field at a depth of $r = 0.8\, r_o$ in a multipolar Boussinesq simulation at low Ro_ℓ. The time is given in viscous diffusion times.

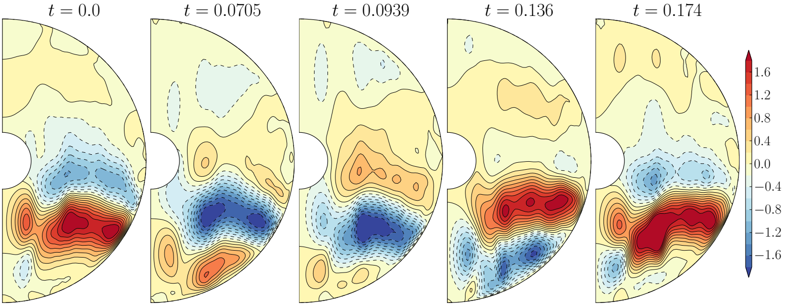

Figure 3.17: Time evolution of the patches of the azimuthal component of the magnetic field (colours) over time. The solid/dashed lines correspond to the positive/negative toroidal magnetic field.

where A and C are ϕ-independent vector potential fields. The induction equation may then be written for $\mathbf{B_P}$ and $\mathbf{B_T}$ to obtain the system

$$\begin{aligned}\frac{\partial A}{\partial t} &= \alpha C + \frac{1}{Pm}\nabla^2 A\\ \frac{\partial C}{\partial t} &= \mathbf{B_P}\cdot\nabla u + (\nabla\times\alpha\mathbf{B_P}) + \frac{1}{Pm}\nabla^2 C,\end{aligned}\tag{3.2}$$

where α represents the diagonal of the α-tensor in the mean electromotive force $\varepsilon = \overline{\mathbf{u}'\times\mathbf{B}'} = \alpha\overline{\mathbf{B}}$, since the turbulent diffusion term was neglected and the α-tensor is considered symmetric. Using Parker (1955)'s plane layer model, Eqs. 3.2 are written in cartesian coordinates (x, y, z) that correspond to the original spherical coordinates (ϕ, θ, r), and the velocity $\overline{\mathbf{u}}$ becomes a function of z (or r) alone. The new system becomes

$$\begin{aligned}\frac{\partial A}{\partial t} &= \alpha C + \frac{1}{Pm}\nabla^2 A\\ \frac{\partial C}{\partial t} &= -\alpha\nabla^2 A + \frac{du}{dz}\frac{\partial A}{\partial y} + \frac{1}{Pm}\nabla^2 C.\end{aligned}\tag{3.3}$$

Obtaining now the dispersion relation requires replacing the fields A and C with the equation of a plane wave in Eq. 3.4, i.e. the ansatz $(A, C) \propto \exp\left[\mathrm{i}(k_y y + k_z y) + \zeta t\right]$. The dispersion relation for the dynamo waves then becomes

$$\left(\zeta + \frac{|\mathbf{k}|^2}{Pm}\right)^2 = \alpha^2\,|\mathbf{k}|^2 + \mathrm{i}\,\alpha\,k_y\,\frac{du}{dz},\tag{3.4}$$

where $\zeta = \xi + \mathrm{i}\,\omega$ is the angular frequency of the wave and $|\mathbf{k}|^2 = k_y + k_z$ is its wavenumber. Since we are looking for an oscillatory behaviour, only the imaginary part of ζ is needed to determine the frequency of the wave. Moreover, α and du/dz are assumed constant. The frequency of the dynamo wave ω is given by

$$\omega = \sqrt{\frac{\alpha\,k_y}{2}\,\frac{du}{dz}}.\tag{3.5}$$

Further simplifications are possible with a few more assumptions. The wavelength is assumed to be of the order of the shell thickness d, which gives $k_y \sim 1/d$, while the differential rotation can be approximated by the ratio between the mean zonal flow $\overline{u_\phi}$ and the thickness of the shell d, i.e. an axisymmetric azimuthal Reynolds number, $du/dz \sim Re_{zon}/d$. Finally the frequency of the dynamo wave will be simply

$$\omega = \sqrt{\frac{\alpha}{2\,d^2}\,Re_{zon}}.\tag{3.6}$$

In order to calculate ω, it is required to estimate a value for α. The most accurate result could be obtained by deriving the full α-tensor (Schrinner et al. 2007), which is out of the reach of this PhD thesis. Instead, an approximation was used which assumes that the small-scale turbulent flow is both homogeneous and isotropic. α can be estimated as the fluctuating kinetic helicity $\alpha \sim -(\tau_c/3)\,(\overline{\mathbf{u}'\cdot\nabla\times\mathbf{u}'})$. The time τ_c refers to the time that a convective feature takes to decay. Brown et al. (2010) estimate τ_c with the ratio between

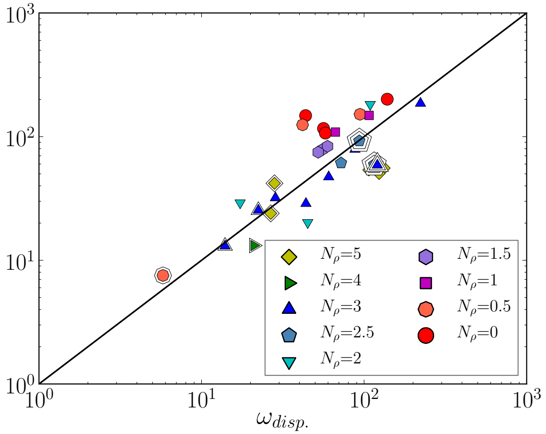

Figure 3.18: Frequencies of the waves measured from butterfly diagrams identical to Fig. 3.15 (y-axis) plotted against the solution from the simplified dispersion relation $\omega_{disp.}$ of Eq. 3.6. The black line simply marks the linear optimal relation between the two values. The symbols with one extra outer black line have the higher Ekman number of 10^{-3} and the symbols with two extra outer black lines have the lower Ekman number of 10^{-5}. The symbols with no extra outer lines all have the moderate Ekman number of $E = 10^{-4}$.

the pressure scale height and the fluctuating velocity of the flow. Here, the density scale height $H_\rho = 1/(d\ln\tilde{\rho}/dr)$ is used instead giving $\tau_c = H_\rho/u'$ as long as $H_\rho < d$, otherwise the density scale height H_ρ is replaced by d to determine τ_c.

Using Eq. 3.6 to determine the frequency of the dynamo waves, the results can be compared with the actual frequencies obtained by applying a Fourier transform to the butterfly diagrams (Figs. 3.15, 3.16). This is plotted in Fig. 3.18, where the black line traces the ideal linear relations between the two values. The points roughly follow the line but with some scatter due to the simplified dispersion relation and the difficulties of estimating α. In several cases it was also difficult to determine the wave frequency. Examples of such dubious cases can be seen in Fig. 3.19 or even when comparing the left panel of Fig. 3.15 with the right panel which is distinctly more clear.

Figure 3.20 displays the frequency of the waves against the supercriticality Ra/Ra_{cr}. Establishing a scaling law for such dependence is questionable, because of the big scatter. The best fit obtained was a logarithmic fit with the equation displayed in the plot of Fig. 3.20. In addition, there appears to be a dependence on Ekman number as well, since the symbols of $E = 10^{-3}$ (one extra outer line) are located below the fitting line and the symbols of $E = 10^{-5}$ (two extra outer lines) are located above. However, this dependence was not explored further due to the underlying uncertainty of the results and the limited number of points.

Figure 3.21 shows the field lines of the magnetic field in a model with a density stratification of three scale heights, supercriticality 4.3 and $Pm = 2$, $Pr = 1$. The bigger concen-

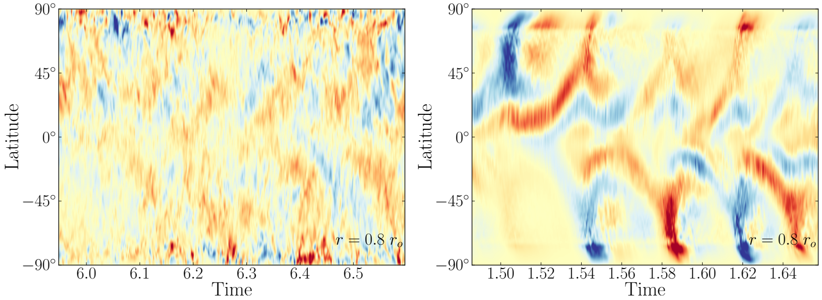

Figure 3.19: Two examples of time evolution of the azimuthally-averaged axisymmetric toroidal field, at a depth of $r = 0.8\,r_o$, that may introduce a sizeable error in the measurement of the values of the frequency of the dynamo wave. The time is given in viscous diffusion times. The simulation on the left corresponds to a case of $N_\rho = 5$ and $E = 10^{-3}$ (thus of higher turbulence, see Fig. 3.7) and the simulation on the right to $N_\rho = 3$ and $E = 10^{-5}$.

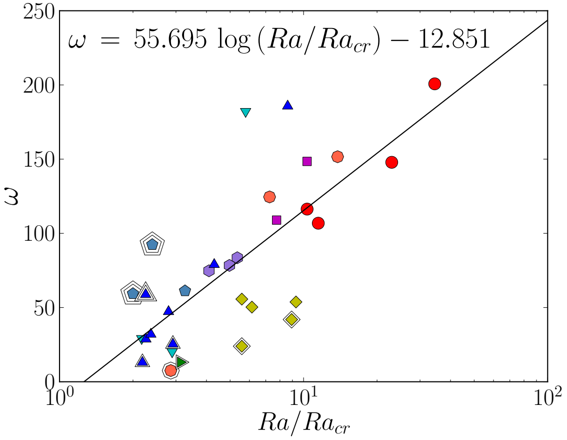

Figure 3.20: Frequencies of the waves measured from butterfly diagrams identical to Fig. 3.15 ω plotted against the supercriticality of the solution Ra/Ra_{cr}. The black line corresponds to the logarithmic fit indicated by the equation. The symbols shapes and colours are described in Fig. 3.18.

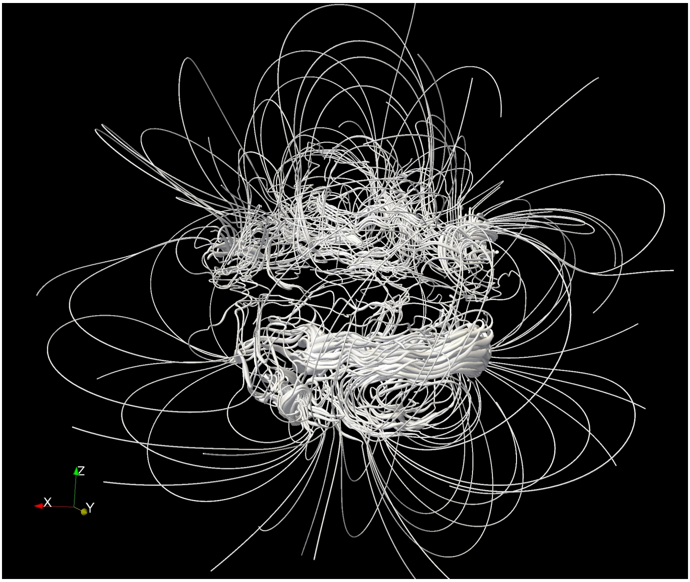

Figure 3.21: 3D rendering of the magnetic field lines in a snapshot of a model with $N_\rho = 3$, $Ra/Ra_{cr} = 4.3$, $Pm = 2$ and $Pr = 1$.

tration of field lines corresponds to the interior of the modelled spherical shell. It can be seen in this image the features discussed throughout this section, namely the effects of the Ω-effect in the southern hemisphere and the non-axisymmetry of the generated field in the northern hemisphere. The absence of poloidal field lines is seen in the equatorial region due to their conversion in toroidal field by the strong Ω-effect. As mentioned above, these models tend to be rather hemispherical and time-dependent. In the northern hemisphere, the large non-axisymmetric $m = 2$ is present, though the toroidal field action in the south dominates at this point of the simulation.

3.3.4 Ekman number dependence

A total of three different Ekman numbers were tested in models with homogeneous conductivity, namely 10^{-3}, 10^{-4} and 10^{-5}. The middle value of 10^{-4} was already discussed in detail in the previous sections, thus now the focus will be on the other two values.

Figures 3.22 and 3.23 show plots similar to the one discussed in section 3.3.1, now for lower and higher Ekman numbers. There is again a dependence of the dipolarity/axisymmetry of the magnetic field on the local Rossby number Ro_ℓ with a clear transition between two types of dynamos, traditionally defined as either dominated by rotation

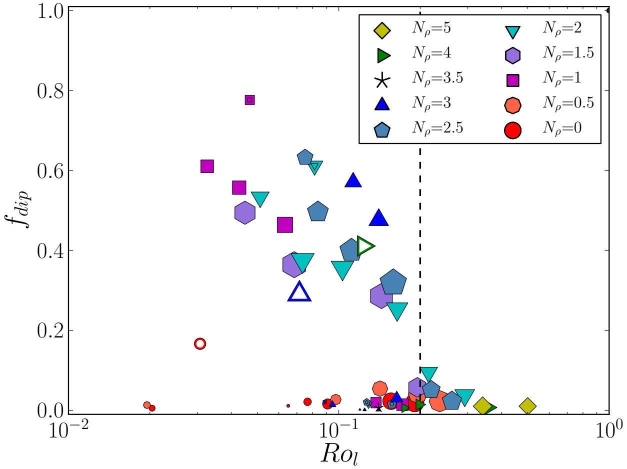

Figure 3.22: Dipolarity versus local Rossby number for Ekman number 10^{-3}. For all the cases, $Pr = 1$ and for most $Pm = 10$. The exceptions are marked with an inner black line which corresponds to cases with $Pm = 5$ instead. The open symbols have an outer no-slip boundary. The size of the symbols of scaled by the strength of the magnetic field, quantified by Eq. 2.54. The dashed line corresponds to $Ro_{\ell\, cr} = 0.2$ and it separates the rotation-dominated from the inertia-dominated regimes.

or by inertia. Christensen and Aubert (2006) reported a remarkable independence of this transition on parameters like the Ekman number or the Prandtl numbers. The results presented here, however, show a strong dependence of this transition on Ekman number E and merely suggest a possible dependence on Prandtl numbers as well, with a single case of different Pr represented by a big blue triangle in Fig. 3.8, of $N_\rho = 3$, $Pr = 0.1$ and $Pm = 1$, which is dipolar at $Ro_\ell \approx 0.15$. Fig. 3.22 reveals a value of $Ro_{\ell\, cr} = 0.2$ indicated in the plot by the dashed line, whilst $Ro_{\ell\, cr} = 0.06$ in Fig. 3.23.

Figure 3.24 shows that models of higher Ekman number prove to be very different from the lower Ekman number (see Fig. 3.7 for comparison) by having no dipolar solutions at very mild density gradients ($N_\rho = 0 - 0.5$), barely hosting a dynamo at all in this range and at lower supercriticallities. The exception is a model at $N_\rho = 0$ shown in Fig. 3.22 with a no-slip outer boundary which stabilizes at $f_{dip} \approx 0.2$. This model is dipolar due to the absence of zonal flow, but its dipolarity is low since dynamo action arises from a single plume (see next section on aspect ratio dependence and Heimpel et al. 2005). The dipolarity window in Fig. 3.24 is now an island located approximately between $N_\rho = 1$ and $N_\rho = 3$. This window thus has an additional lower boundary ($N_\rho \approx 1$), bearing a decrease of the $Ro_{\ell\, cr}$ towards lower supercriticalities. According to this regime diagram, there is an absence of strong magnetic fields (reduced size of the symbols) at $N_\rho = 0 - 0.5$ and $Ro_\ell < 0.08$. This suggests that higher supercriticality Ra/Ra_{cr} and higher value of N_ρ help promote dynamo action, where the latter may even promote dipole-dominated fields till

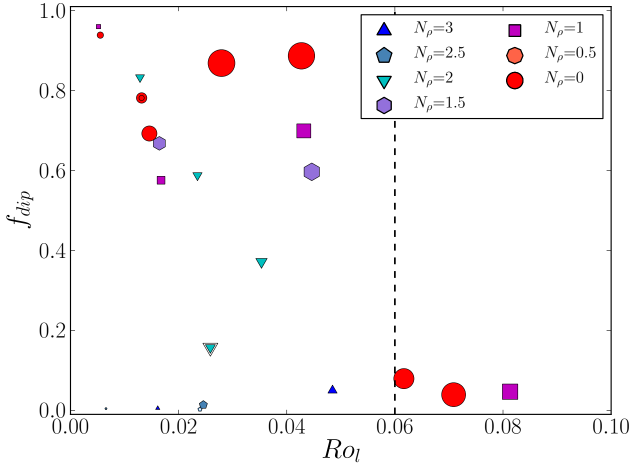

Figure 3.23: Dipolarity versus local Rossby number for Ekman number 10^{-5}. For all the cases, $Pr = 1$ and for most $Pm = 1$. The exceptions are marked with an inner (outer) black line which corresponds cases with $Pm = 0.5$ ($Pm = 2$) instead. The open symbols have an outer no-slip boundary. The size of the symbols of scaled by the strength of the magnetic field, quantified by Eq. 2.54. The dashed line corresponds to $Ro_{\ell\,cr} = 0.06$ and it separates the rotation-dominated from the inertia-dominated regimes. Note that the x-axis is displayed in linear scale, unlike Figs. 3.8 and 3.22, which is more appropriate here due to the smaller range of Ro_ℓ for this dataset.

a certain point ($N_\rho \approx 3$). Figure 3.25 displays the radial magnetic field at the equatorial plane of two multipolar cases of $N_\rho = 0$ and $N_\rho = 0.5$ with supercriticalities $Ra/Ra_{cr} = 4.0$ and $Ra/Ra_{cr} = 2.9$, respectively. The generation of the radial magnetic field for such cases happens in a smaller localized region, only on one side of the inner boundary, thus the strength and consistency of the resulting field will be limited. This point will be revisited in the next section.

Figure 3.26 is similar to Fig. 3.9, but for the $E = 10^{-3}$ data set. This figure shows the expected existence of two main groups corresponding to the two possible branches: multipolar solutions with weaker magnetic field and stronger zonal flow amplitude and dipolar solutions with stronger magnetic field but a weak zonal flow. Even though there is a less pronounced separation between the two branches in Fig. 3.22 due a more gradual decrease of dipolarity, there is still a clear separation between the two types of dynamo solutions.

A lower value of Ekman number means reduced viscous effects. Both the magnetic and kinetic energy spectra of a magnetic simulation broaden compared to the non-magnetic case, independently of the Ekman number. This difference between a purely hydrodynamic case and a dynamo suggests that the scale of the flow is mainly affected by the magnetic field. The small-scale structures also become increasingly more import for the lower Ekman numbers, making these computationally more challenging (Rotvig and

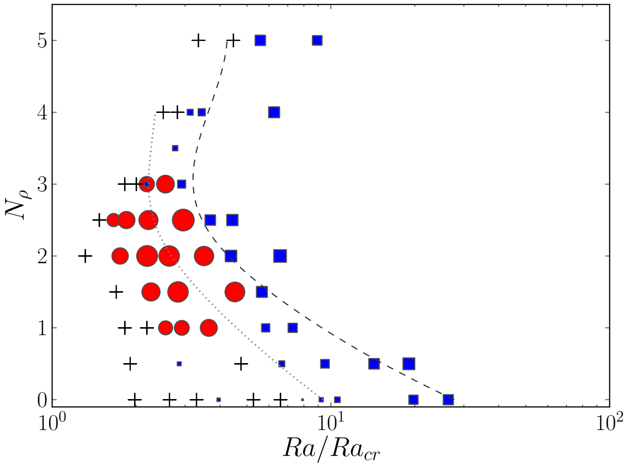

Figure 3.24: Number of density scale heights N_ρ versus supercriticality of the system Ra/Ra_{cr}, for Ekman number 10^{-3}. The red circles correspond to dipole-dominated magnetic fields, the blue squares are multipolar fields and the crosses represent failed dynamos. The dashed line traces the transition between rotation-dominated and inertia-dominated regimes, $Ro_{\ell\,cr} = 0.2$. The dotted line corresponds to $Ro_\ell = 0.08$, which was the value of $Ro_{\ell\,cr}$ at $E = 10^{-4}$.

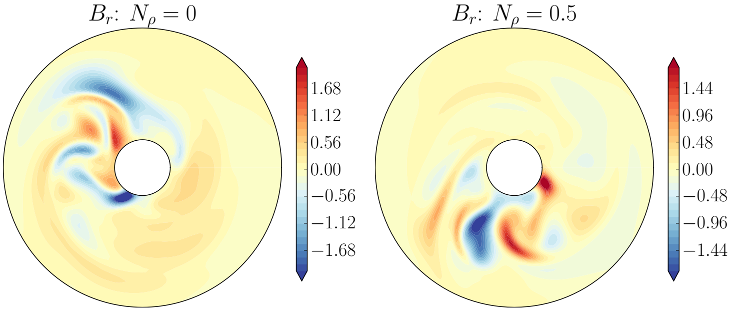

Figure 3.25: Equatorial cuts of the radial magnetic field for the two multipolar cases of $N_\rho = 0$ (left panel) and $N_\rho = 0.5$ (right panel), of lower supercriticality in Fig. 3.24.

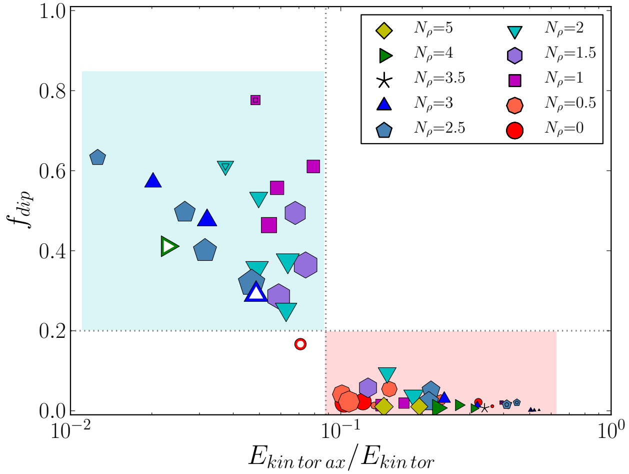

Figure 3.26: Dipolarity versus the ratio between the axisymmetric part of the toroidal kinetic energy and the the total toroidal kinetic energy, for Ekman number 10^{-3}. The symbols have the same correspondence as in Fig 3.22.

Jones 2002).

Figure 3.27 displays the regime diagrams of density gradient given by N_ρ at $E = 10^{-5}$ versus supercriticality of the system Ra/Ra_{cr}. Again, the differences become clear between the different Ekman numbers. The transition between the two regimes of dynamo action takes place at lower values of Ro_ℓ with decreasing E. Yadav et al. (2013a) suggest a dependence of Ro_ℓ on parameters like E and Pm for Boussinesq models with free-slip boundaries, but a different aspect ratio ($\eta = 0.35$). A dependence on aspect ratio η was reported previously by Aubert et al. (2009). They introduced a correction to $Ro_{\ell\,cr}$ to eliminate the dependence on η, but this is not applied here due to the fixed value of $\eta = 0.2$, with the exception of the next section.

In Figure 3.27, the Boussinesq and mild density gradient models show a behaviour similar to what was observed in the previous sections for $E = 10^{-4}$. However, at higher values of N_ρ (close to the limit of dipole-dominated solutions, $N_\rho \sim 2$), the average dipolarity decreases gradually toward $Ro_{\ell\,cr}$. This gradual decrease is clear in Fig. 3.23 for $N_\rho = 2$ (the three inverted cyan triangles at $Ro_\ell < Ro_{\ell\,cr}$). This is not observed in solutions with $N_\rho = 0 - 1.5$, where the dipolarity f_{dip} is nearly independent of Ro_ℓ, up to the point where the transition occurs (magenta squares $N_\rho = 1$, purple hexagons $N_\rho = 1.5$ and red circles $N_\rho = 0$, in Fig. 3.23). On the other hand, for the higher Ekman number $E = 10^{-3}$ (Fig. 3.22), there is a tendency to always have a gradual decrease of dipolarity for any value of N_ρ. In the previous sections, it was seen that in the range of $N_\rho = 1.5 - 1.9$ for $E = 10^{-4}$ (Fig. 3.7), the dipolarity window decreases in Ro_ℓ extent with increasing N_ρ, i.e. the transition occurs and a lower Ro_ℓ than at $N_\rho < 1.5$. This seems to be the case

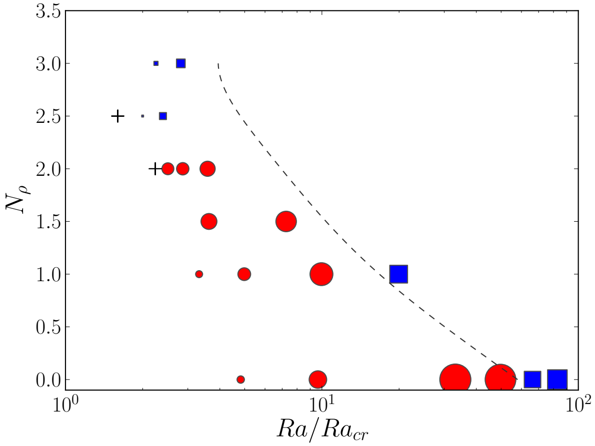

Figure 3.27: Number of density scale heights N_ρ versus supercriticality of the system Ra/Ra_{cr}, for Ekman number 10^{-5}. The red circles correspond to dipole-dominated magnetic fields, the blue squares are multipolar fields and the crosses represent failed dynamos. The dashed line traces the transition between rotation-dominated and inertia-dominated regimes, at $Ro_\ell = 0.06$.

for $E = 10^{-5}$ as well, hence the existence of the gradual decrease in f_{dip} at the top of the dipolarity window seen in Fig. 3.23.

3.3.5 Aspect ratio dependence

The motivation for this last section was the complete absence of dipole-dominated dynamo solutions at $E = 10^{-3}$ and $N_\rho = 0-0.5$ in Fig. 3.22 of the previous section. For thinner shells (higher values of η), there appears to be no difficulty obtaining dipole-dominated magnetic fields though. Figure 3.28 corresponds to a regime diagram of aspect ratio η versus Ra/Ra_{cr}, with red symbols representing dipole-dominated magnetic fields and blue squares multipolar fields. This figure reveals that a requirement of a minimum value of $\eta = 0.35$ (for this set of parameters: $E = 10^{-3}$, $Pr = 1$ and $Pm = 10$) is needed to obtain a dipolar dynamo solution, or simply consistent dynamo solution. One may speculate about the relation to the length scale of the flow, which increases with Ekman number, as shown in the first section of this Chapter, about the onset of convection in a rotating spherical shell. According to Fig. 3.8, at $E = 10^{-4}$ this behaviour does not exist any more.

Two other effects alter the scale of the flow convective motions, where one is the size of the shell. It is shown in Tab. 3.2 that the scale decreases for thinner shells, i.e. higher values of m_{cr} are obtained for higher η. The other effect is the density stratification itself, which was the main topic of discussion throughout the previous sections of the present Chapter and this is clearly shown by the increase of m_{cr} with N_ρ in Tab. 3.1.

Figures 3.29, 3.30 and 3.31 show, respectively, the contours of axial vorticity in the equatorial plane, radial velocity field at the mid-depth and and the resulting magnetic

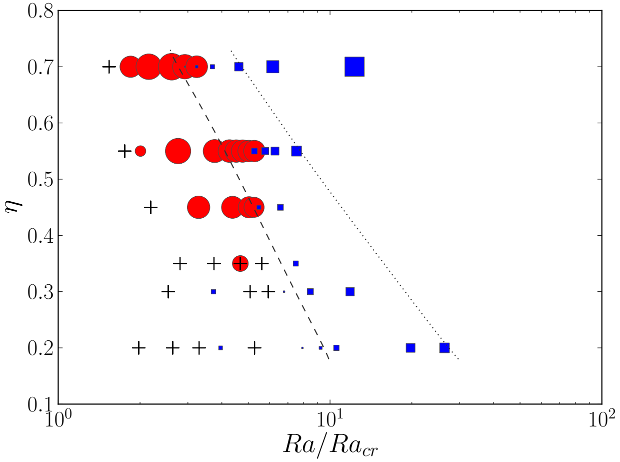

Figure 3.28: Aspect ratio of the spherical shell η versus supercriticality of the system Ra/Ra_{cr}, for Ekman number 10^{-3}, $Pr = 1$ and $Pm = 10$. The red circles correspond to dipole-dominated magnetic fields, the blue squares are multipolar fields and the crosses represent failed dynamos. The dashed (dotted) line serves only to trace a constant value of $Ro_\ell = 0.08$ ($Ro_\ell = 0.2$).

Table 3.2: Values of critical Rayleigh number (Ra_{cr}) and critical wave number (m_{cr}) for different aspect ratios η at $E = 10^{-3}$, $N_\rho = 0$ and $Pr = 1$. The values listed were obtained with a modified version of the linear code by Jones et al. (2009).

η	Ra_{cr}	m_{cr}
0.2	7.582×10^4	2
0.3	5.905×10^4	4
0.35	5.345×10^4	4
0.45	4.457×10^4	6
0.55	3.985×10^4	9
0.7	3.248×10^4	16

field and at the outer boundary, for five different aspect ratios. These five dynamo cases were selected from Fig. 3.28 for the lower supercriticality, to clearly visualize the effects of varying η. Figures 3.29 and 3.30 show that in smaller aspect ratios (thicker shells), convection arises from a single plume of upwelling in a limited region on one side of the inner core, where most of the poloidal magnetic field is generated (see also Fig. 3.25). This column is then sheared around the tangent cylinder by the dominant zonal flow that exists in the remaining part of the volume, empty of columnar convection (see top row of Fig. 3.30). Thus dynamo action in these models is restricted in longitude, which makes it less efficient. Heimpel et al. (2005) studied this behaviour in detail and the models simulated here differ from theirs only in the type of upper mechanical boundary condition,

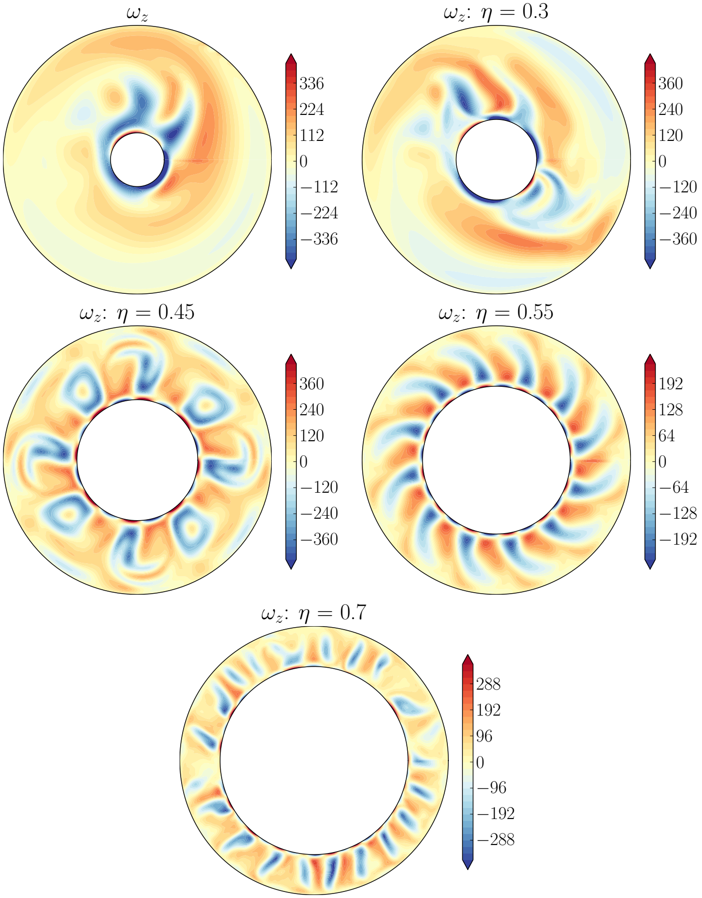

Figure 3.29: Equatorial cuts of the axial vorticity for five cases of $N_\rho = 0$ and increasing η from top to bottom and left to right. The cases selected are the dynamo solutions of lower supercriticality in Fig. 3.28.

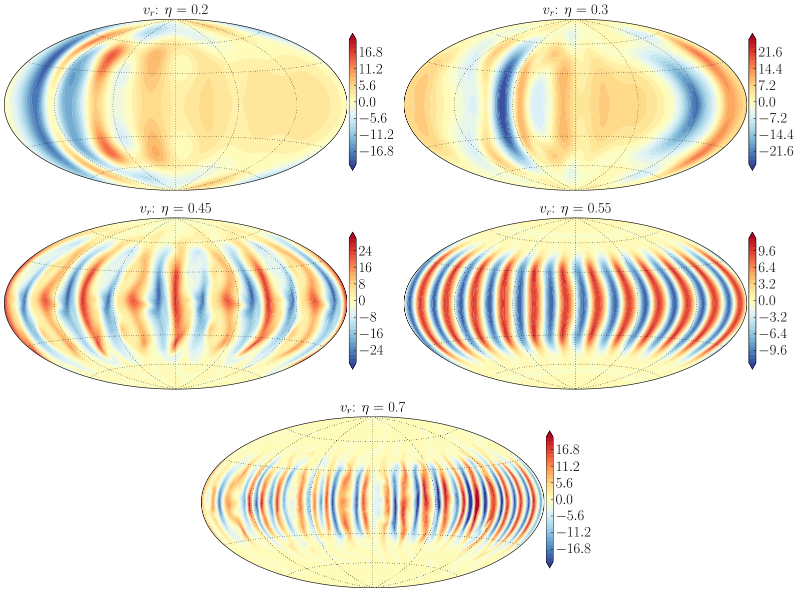

Figure 3.30: Mid-depth maps of the radial velocity field for the same cases listed in Fig. 3.29.

since they assumed no-slip. The increasing efficiency of dynamo action with η can be observed in Fig. 3.31 where the surface radial magnetic fields of the five cases in Fig. 3.29 are presented. There is a difference in field strength of around one order of magnitude between $\eta < 0.35$ and $\eta > 0.35$ models and the multipolar morphologies of the first contrast with the dipolar magnetic fields of the second.

As Heimpel et al. (2005) reported, there are three main features associated with the change between a single plume dynamo and a multi plume one. The first is the decrease of Ra for onset of dynamo action as it approaches Ra_{cr} with increasing η. This can be seen in Fig. 3.28, where the region of failed dynamos (crosses) becomes narrower towards thinner shells. Consequently, the kinetic energy of the dipolar dynamos of lower supercriticality also decreases. The second change detected is displayed in Fig. 3.32 and it is the reversal of the ratio of magnetic to kinetic energies, where the magnetic energy becomes lower than the kinetic for large shells, $\eta = 0.2 - 0.3$ here and $\eta = 0.15$ in Heimpel et al. (2005)'s work. The fact that the transition happens here between $\eta = 0.3$ and $\eta = 0.35$, while it took place between $\eta = 0.15$ and $\eta = 0.25$ in their work is due to the different outer boundary condition. As seen in the previous sections, the enhancement of zonal flow due to a free-slip boundary is problematic for sustaining a strong dipolar field. In this case, it delays the transition between multipolar and dipolar dynamos with increasing η.

The third observation by Heimpel et al. (2005) was that both poloidal kinetic and magnetic energies increase with η. Since the total kinetic energy actually decreases with

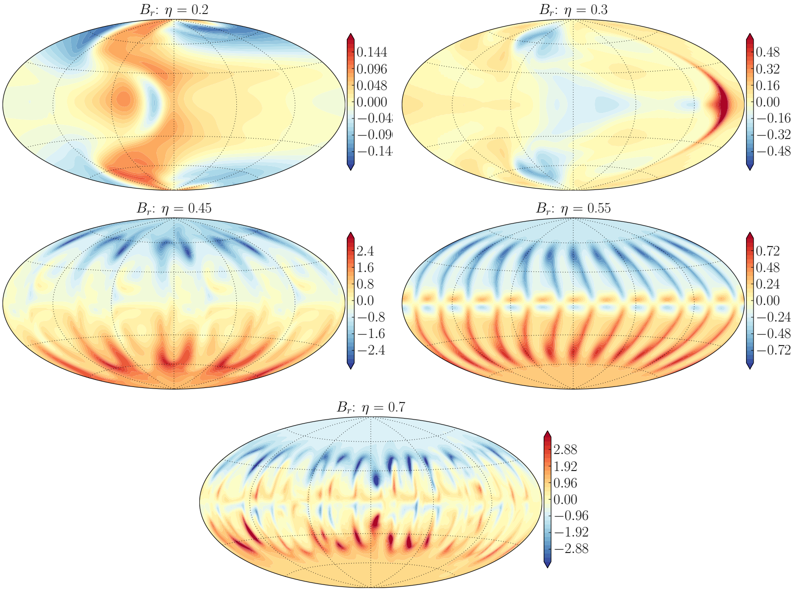

Figure 3.31: Surface maps of the radial magnetic field for the same cases listed in Fig. 3.29.

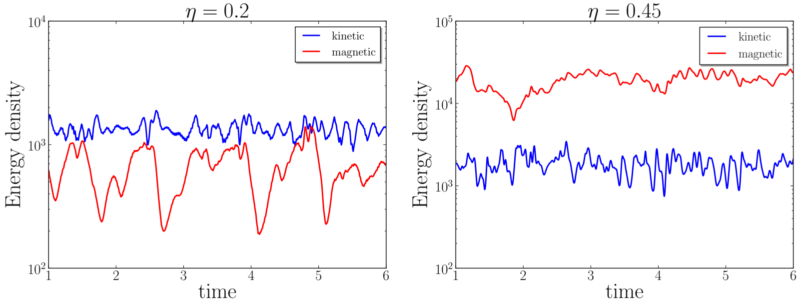

Figure 3.32: Kinetic (blue line) and magnetic (red line) energy densities of two cases with $\eta = 0.2$ (left panel) and $\eta = 0.45$ (right panel) of supercriticalities 4.0 and 3.4, respectively. The left panel belongs to a multipolar dynamo and the right panel to a dipolar one (see Fig. 3.28). The time is given in viscous time.

η, this would mean that the poloidal motions contain most of the kinetic energy for thinner shells. Poloidal kinetic energy comes from the flow along the convective columns, which is the main responsible for the helicity that produces the poloidal magnetic field. Thus the relative importance of one is usually followed by the other in models of $N_\rho = 0$. Hence the models presented here of thinner shells $\eta \geq 0.35$ are α^2-dynamos. In the case of thicker shells, the helical flow arises from one column (possibly two) and the remaining part of the volume is filled with axisymmetric toroidal flow that generates toroidal magnetic field through Ω-effect, making these dynamos of $\alpha\Omega$-type.

To conclude, three effects in the models studied in this Chapter affect the scale of the flow: the number of convection columns increases with decreasing E, with increasing η and with increasing N_ρ. Thus it was shown in this and the previous sections that a combination of the three such that the scale of the convection cells becomes so large that it comes down to only one or two dominant plumes, dynamo action will be difficult and predominantly non-dipolar.

4 Radially varying electrical conductivity

4.1 Results

As seen in the previous Chapter, in the complex models explored here, the magnetic field geometry not only depends on the local Rossby number (Christensen and Aubert 2006) but also on the density stratification, on the Ekman number, and on the magnetic Prandtl number. The "universality" of Ro_ℓ as the best way to separate the different dynamo regimes was questioned in the results presented in Chapter 3, thus now the analysis will be extended to models with varying electrical conductivity (see Chapter 2, section 2.4 for the modelling information). The present Chapter was adapted from Duarte et al. (2013).

4.1.1 Dynamo regimes

Figure 4.1 shows the dependence of the dipolarity f_{dip} on the local Rossby number for all cases with varying conductivity, excluding runs with $Pm \neq 2$, with the exception of the case marked by a grey dot in the interior, which is one of the models of Heimpel and Gómez-Pérez (2011). To illustrate the relation between the field geometry and the zonal flows, f_{dip} is plotted versus the relative kinetic energy of axisymmetric azimuthal flows Z (Eq. 2.46) in Fig. 4.2. In both figures, the symbol type refers to the different stratifications N_ρ while the symbol colour identifies the four transitional radii χ_m explored in this Chapter. The first part is an analysis of the different dynamo regimes based on the results for $E = 10^{-4}$ and $Pm = 2$, followed by an expansion to other Ekman numbers and the discussion about the role of the zonal flow.

4.1.1.1 Ekman number $E = 10^{-4}$

When the weakly conducting layer is relatively thin ($\chi_m = 95\%$ and $\chi_m = 90\%$) and the stratification is mild to intermediate ($N_\rho \leq 2$), we once more find the two distinct branches described in the previous Chapter. The dipolar branch, characterized by $f_{dip} > 0.7$ and weak zonal flows, is restricted to cases with local Rossby numbers below the critical value of $Ro_{\ell cr} \approx 0.04$. This is significantly lower than the value of $Ro_{\ell cr} \approx 0.08$ suggested for homogeneous electrical conductivity by the results of Chapter 3 (Gastine et al. 2012). The dipole-dominated solutions forming this branch are located in the upper left corner of Fig. 4.1 and in the left portion of the yellow high-dipolarity regime in Fig. 4.2.

The second branch with multipolar magnetic fields at $f_{dip} < 0.2$ but intermediate zonal

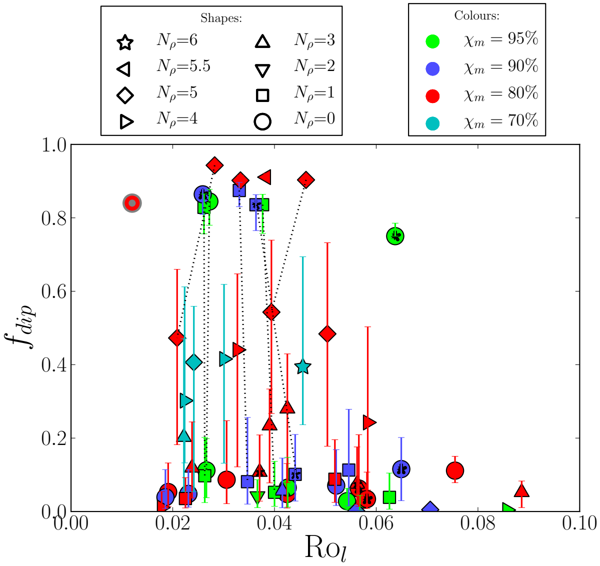

Figure 4.1: Dipolarity against the local Rossby number defined by Eq. (2.50). The black star inside the symbols marks the cases with a no-slip upper boundary, instead of free-slip. The error bars correspond to standard deviations of the time series of each case, for which the point itself is the time average. The dotted lines connect sets of cases for which we found two solutions, depending on the initial magnetic field. The Boussinesq case with a grey dot inside is the case from Heimpel and Gómez-Pérez (2011) of $\chi_m = 80\%$ and $\eta = 0.35$ and $E = 10^{-5}$. This image was adapted from Duarte et al. (2013).

flows exists for all Ro_ℓ values. These solutions can be found in the lower part of Fig. 4.1 and the cyan low-dipolarity regime in Fig. 4.2.

Figures 4.1 and 4.2 contain examples (dotted lines) where a solution on each branch is found for identical model parameters, clearly demonstrating the bistability for $Ro_\ell < Ro_{\ell cr}$. As a reminder (see Chapter 3), which branch a specific numerical simulation will chose depends on the initial magnetic field configuration and the multipolar attractor always has the more intense zonal flows (see Fig. 4.2). Comparing magnetic Reynolds numbers and local Rossby numbers for bistable cases shows that the relative difference is smaller in the latter than in the former measure. This indicates that the weaker flow amplitude caused by the larger Lorentz forces in the dipole-dominated cases is accompanied by a growth in the flow length scale.

Increasing the stratification to values beyond $N_\rho = 2$ while keeping χ_m large always leads to solutions of the multipolar thin-shell type discussed in Chapter 3, i.e. the confinement of the dominating dynamics in a limited radial extent ($\sim 10 - 20\%$ of d), just below the outer boundary r_o, thus making an imaginary thinner shell where most of the dynamics of the system takes place. Altogether, the behaviour for a thin weakly conduct-

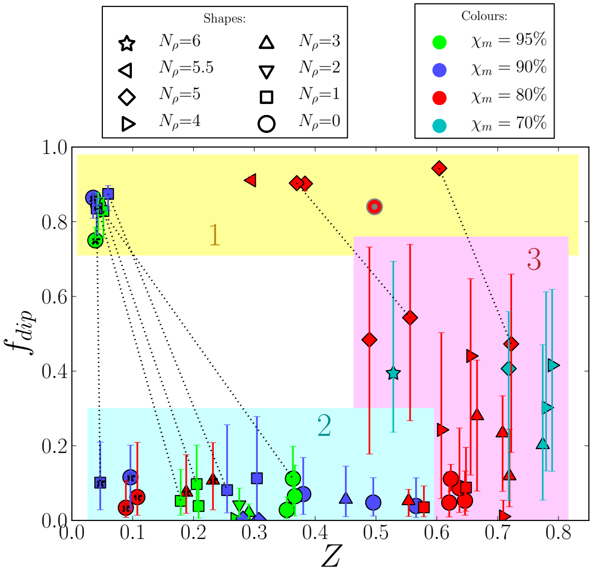

Figure 4.2: Dipolarity plotted against the ratio between the azimuthal kinetic energy and the total kinetic energy, averaged in time and volume. The symbols and colours have the same definition as in Fig. 4.1. The three boxes mark the three different regimes discussed in the text. The dotted lines connect sets of cases for which we found two solutions, depending on the initial magnetic field. This image was adapted from Duarte et al. (2013).

ing layer is similar to that for a homogeneous electrical conductivity with the exception of the lower value of critical Rossby number $Ro_{\ell cr}$.

For a thicker weakly conducting layer with $\chi_m = 80\%$, the influence of the stratification on the dipolarity is reversed. Clearly, dipolar solutions with $f_{dip} > 0.7$ now exclusively exist for stratifications of $N_\rho = 5$ or $N_\rho = 5.5$ (see Fig. 4.1). Since the relative zonal flow amplitude reaches intermediate values, these cases can be found in the middle section of the yellow regime in Fig. 4.2. A second branch of solutions is characterized by low to intermediate dipolarity f_{dip}, that increases with N_ρ, and by large relative zonal flow amplitudes; these cases populate the pink region in Fig. 4.2. For stratification of $N_\rho \geq 3$, the solutions on this secondary branch become strongly time-dependent as indicated by the large error bars in Figs. 4.1 and 4.2. Figure 4.3 demonstrates that the time dependence reflects an oscillation between dipolar and multipolar field configurations without ever establishing a stable solution on the dipole-dominated branch. Polarity reversals or excursions become possible when the dipolarity is relatively low.

Once more, both branches coexist for not too large local Rossby numbers and we could identify two bistable cases for $\chi_m = 80\%$, $N_\rho = 5$, $Ra/Ra_{cr} = 7.4$ (solid red profile of Fig. 2.3) and $Ra/Ra_{cr} = 9.3$ (dashed red profile of Fig. 2.3). When increasing the Rayleigh number to $Ra/Ra_{cr} = 11.2$, however, only the multipolar solution remains which suggests

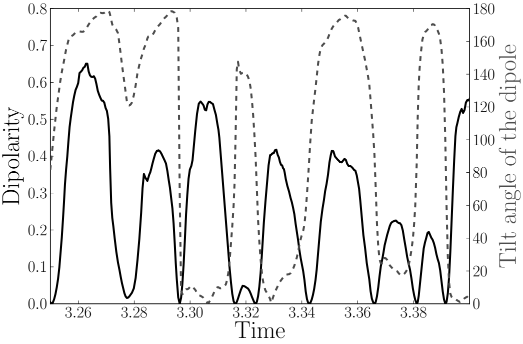

Figure 4.3: Time evolution of the dipolarity at the surface (solid black line) and the tilt angle of the dipole (dashed grey line) in degrees. The time is given in magnetic diffusion units. The parameters are: $E = 10^{-4}$, $N_\rho = 3$, $Ra = 4.3\,Ra_{cr}$, $\chi_m = 80\%$. This image was taken from Duarte et al. (2013).

a critical local Rossby number of about $Ro_{\ell cr} \approx 0.05$.

For $\chi_m = 70\%$, the thickest weakly conducting outer shell explored here, even the stronger stratification of $N_\rho = 6$ is not sufficient to establish a dipole-dominated magnetic field, which was possible already with $N_\rho \geq 5$ at $\chi_m = 80\%$. For the magnetic Prandtl number $Pm = 2$, generally used here at $E = 10^{-4}$, only the highly time-dependent solutions with intermediate dipolarity and strong zonal winds (on average) were found, even at $N_\rho = 5, 6$. Despite the fact that the mean dipolarity increases with N_ρ for $N_\rho = 3-5$, just as in the $\chi_m = 80\%$ cases, the case at $N_\rho = 6$ suggests that dipolar solutions might not exist at any value of N_ρ for $\chi_m = 70\%$ (cyan symbols/line of Fig. 4.4, discussed in the next paragraph).

Figure 4.4 highlights the role of the density stratification at $\chi_m = 95\%$, 90%, 80% and 70% for models at $E = 10^{-4}$ and $Pm = 2$ with similar local Rossby numbers, $Ro_\ell \sim 0.04$. When the weakly conducting layer is relatively thin ($\chi_m = 95\%$ or $\chi_m = 90\%$), dipole-dominated solutions can only be found for $N_\rho < 2$ while multipolar solutions exist for all stratifications. For a thicker conducting layer, however, the stratification has a reversed effect. The mean dipolarity increases slightly with stratification and highly dipolar solutions are only found for stronger stratifications $N_\rho \geq 5$. Note that at $\chi_m = 90\%$ and $N_\rho = 0$, we could only find multipolar solutions, even at low Rayleigh numbers where Ro_ℓ is small. The reason for this is not yet understood. What finally helped to establish a dipolar solution here was increasing the magnetic Prandtl number from 2 to 5.

We tested the effect of larger magnetic Prandtl numbers for several other parameter combinations and this often promoted dipole-dominated solutions. For example, at $\chi_m = 80\%$ and $N_\rho = 0$ a multipolar case became dipolar when increasing Pm from 2 to 10. Likewise, the highly time-dependent case at $\chi_m = 80\%$, $N_\rho = 4$, $Ra/Ra_{cr} = 5.5$ and $Pm = 2$ developed into a stable dipole-dominated solution when doubling Pm. The same behaviour was found at $\chi_m = 70\%$, $N_\rho = 4$ and $Ra/Ra_{cr} = 6.6$. This indicates a certain

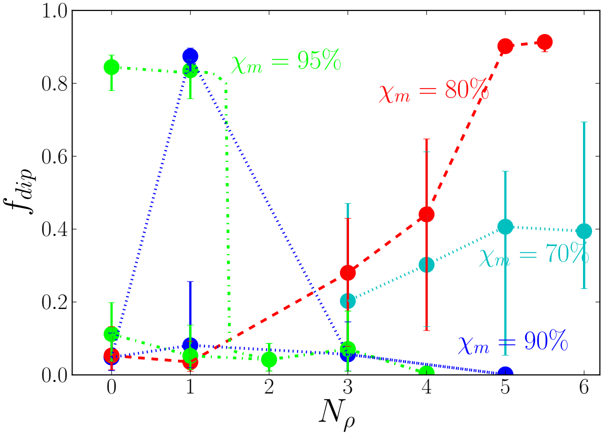

Figure 4.4: Dipolarity against density stratification, for fixed transition radii: green $- \chi_m = 95\%$, blue $- \chi_m = 90\%$, red $- \chi_m = 80\%$, cyan $- \chi_m = 70\%$. The dashed lines simply gather the symbols with the same χ_m. The error bars are the same as in Figs. 4.1 and 4.2. This image was adapted from Duarte et al. (2013).

trade-off between larger stratifications and higher electrical conductivities. At $\chi_m = 80\%$ or 70%, $N_\rho = 3$ and $Ra/Ra_{cr} = 4.3$, however, an increase from $Pm = 2$ to $Pm = 6$ was not sufficient to establish a dipole-dominated solution. Even higher magnetic Prandtl numbers may be required here.

Figure 4.5 illustrates the different types of solutions with snapshots of the radial magnetic field at the outer boundary for $E = 10^{-4}$. The top row shows $\chi_m = 95\%$ cases at two different stratifications: a dipole-dominated Boussinesq case and a multipolar solution at $N_\rho = 4$. The latter shows a large scale wave number ($m = 1$) structure, similar to that reported for multipolar dynamos with homogeneous electrical conductivity and free-slip boundaries (Goudard and Dormy 2008, Gastine et al. 2012, Chapter 3). The bottom row of Fig. 4.5 depicts the two branches found for $\chi_m = 80\%$. The left panel shows a snapshot of a Boussinesq multipolar case and the right panel illustrates the dipolar configuration found at strong stratifications ($N_\rho = 5$).

4.1.1.2 Ekman number dependence

Several cases at $E = 10^{-3}$, $E = 3 \times 10^{-4}$, $E = 3 \times 10^{-5}$ and $E = 10^{-5}$ help to eplore the Ekman number dependence. The Boussinesq case marked by a grey dot in Figs. 4.1 and 4.2 is identical to one of the models presented by Heimpel and Gómez-Pérez (2011) and has a larger aspect ratio of $\eta = 0.35$ instead of $\eta = 0.2$.

Figure 4.6 shows five panels, each for one of five different values of Ekman number ($E = 10^{-3}$ in panel **a.**, $E = 3 \times 10^{-4}$ in panel **b.**, $E = 10^{-4}$ in panel **c.**, $E = 3 \times 10^{-5}$ in panel **d.** and $E = 10^{-5}$ in panel **e.**) and for different magnetic Prandtl numbers ($Pm = 0.5 - 10$). The

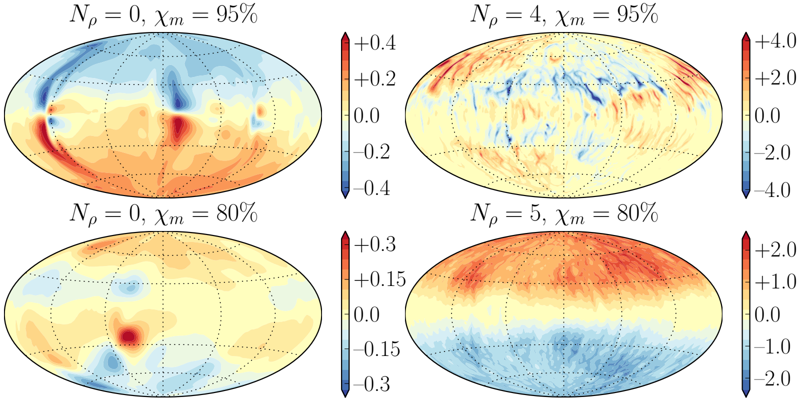

Figure 4.5: Radial magnetic field at the outer boundary. The top row corresponds to $\chi_m = 95\%$ cases and the bottom row to $\chi_m = 80\%$ cases. The maps on the left are $N_\rho = 0$ cases ($Ra/Ra_{cr} = 11.5$ and $Ra/Ra_{cr} = 23.0$, top and bottom, respectively) and the maps on the right column are $N_\rho = 4$, $Ra/Ra_{cr} = 5.5$ (top) and $N_\rho = 5$, $Ra/Ra_{cr} = 7.4$ (bottom). The magnetic field contours are given in units of Elsasser number Λ. This image was taken from Duarte et al. (2013).

$E = 10^{-4}$ cases were discussed in the previous section. The correspondence of colours is different to accommodate the different values of Pm, since E is a constant in each panel of Fig. 4.6. The colour of the outer line of the symbols now indicates χ_m, using the same colours as in the previous section, i.e. green, blue, red and cyan represent $\chi_m = 95\%$, $\chi_m = 90\%$, $\chi_m = 80\%$ and $\chi_m = 70\%$, respectively. The grey scale of the symbol colour codes the magnetic Prandtl number Pm, reading from light grey ($Pm = 0.5$) to black ($Pm = 10$). The open symbols mark the outer no-slip boundary (in the previous section, these were marked by a star) and the star is the case from Heimpel and Gómez-Pérez (2011) (in the previous section, this case was marked by a grey dot). Finally, the shape of the symbols corresponds to the value of N_ρ, as in the previous section (Figs. 4.1 and 4.2).

All five Ekman numbers show a similar behaviour, with the sharp transition from dipole-dominated at local Rossby numbers below a critical value $Ro_{\ell cr}$ to multipolar for $Ro_\ell > Ro_{\ell cr}$. The two branches at $Ro_\ell < Ro_{\ell cr}$ are present as well, with dipoles and multipoles populating each of the two branches, plus a few bistability cases found mainly at higher values of E. The main difference between the five different Ekman numbers is the also different values of $Ro_{\ell cr}$ for each. This means that the transition between the values of Ro_ℓ for which dipolar solutions exist and where only multipoles remain is clearly dependent on Ekman number.

While for $E = 10^{-4}$ and $\chi_m = 80\%$ we had to increase the stratification to $N_\rho \geq 5$ to find strongly dipolar solutions, this is not the case any more at $E = 10^{-5}$ (panel **e.**). Even the Boussinesq models now clearly have dipole-dominated magnetic fields. The multipolar case at $N_\rho = 1$ with a local Rossby number of $Ro_\ell \approx 0.04$ seems to be of the highly time-

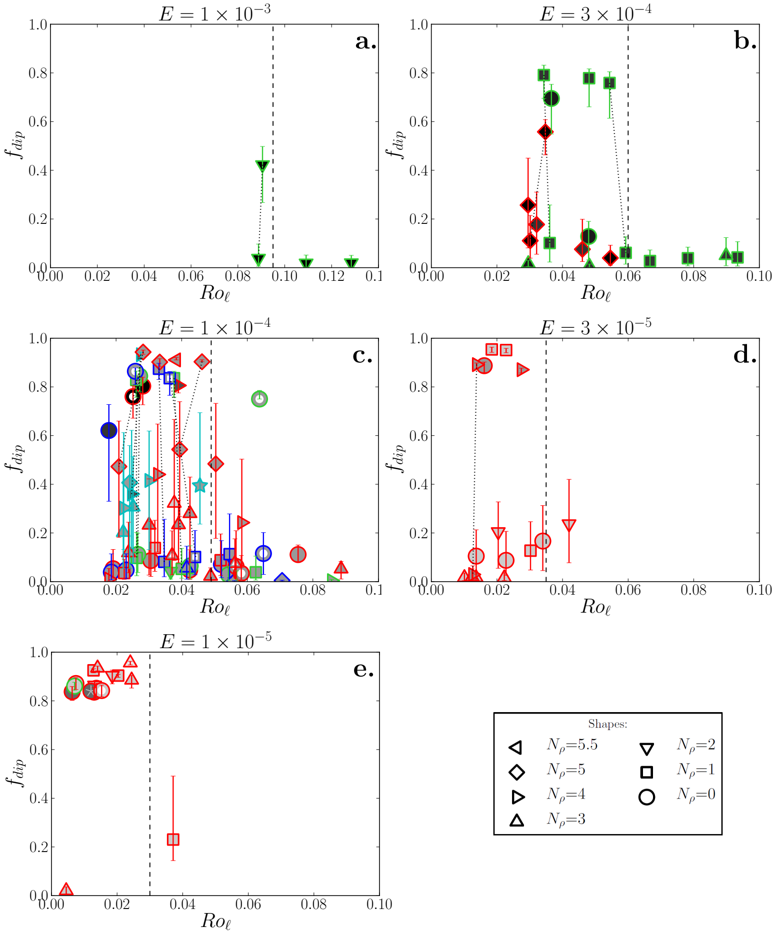

Figure 4.6: Dipolarity against the local Rossby number defined by Eq. (2.50). The colour of the outer line of each symbol represents here the vale of χ_m as in Figs. 4.1 and 4.2: green – $\chi_m = 95\%$, blue – $\chi_m = 90\%$, red – $\chi_m = 80\%$ and cyan – $\chi_m = 70\%$. The inner colour (grey) represents Pm, where darker/lighter corresponds to higher/lower value. The empty symbols mark the cases with a no-slip upper boundary. The error bars correspond to standard deviations of the time series of each case, for which the point itself is the time average. The dotted lines connect sets of cases for which we found two solutions, depending on the initial magnetic field. Each of the five panels corresponds to a different E and the dashed line marks a likely location for $Ro_{\ell cr}$. The circle with a star inside in panel **e.** is the case from Heimpel and Gómez-Pérez (2011).

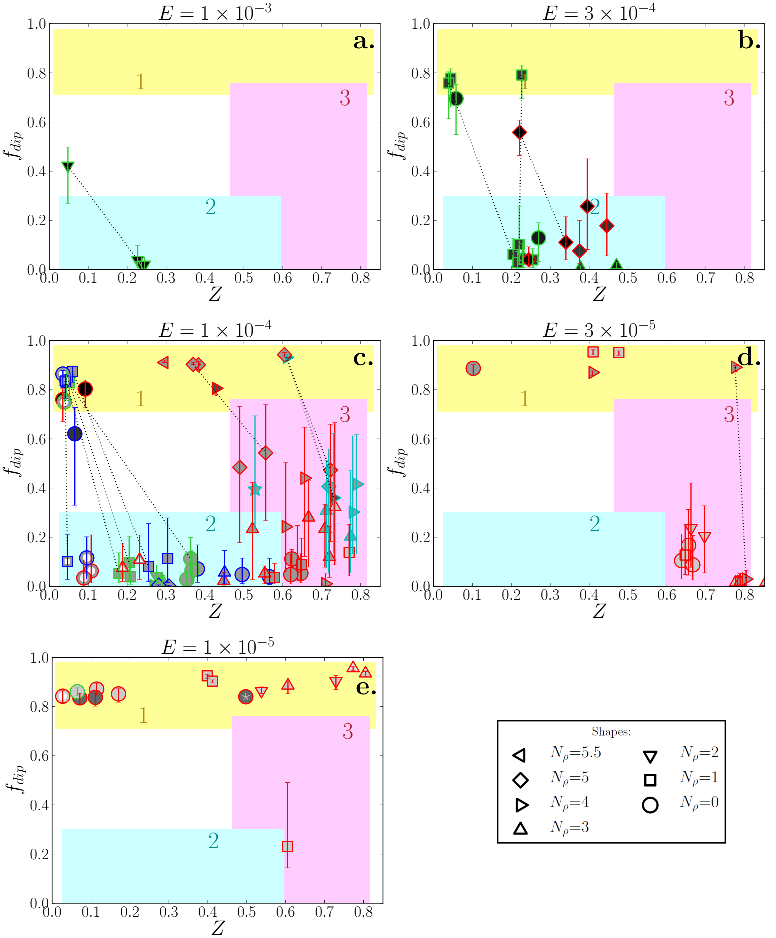

Figure 4.7: Dipolarity plotted against the ratio between the azimuthal kinetic energy and the total kinetic energy Z, averaged in time and volume. The symbols and colours have the same definition as in Fig. 4.6. The three boxes mark the three different regimes of Fig. 4.2 merely for comparison. The dotted lines connect sets of cases for which we found two solutions, depending on the initial magnetic field. Each panel corresponds to a different Ekman number E. Similarly to Fig. 4.6, panels **c.** and **e.** were adapted from Duarte et al. (2013).

dependent type. Another model at $N_\rho = 1$ but $Ro_\ell \approx 0.02$ is strongly dipolar so that the critical local Rossby number can be estimated to $Ro_{\ell cr} \approx 0.03$ at $E = 10^{-5}$. Note however, that $Ro_{\ell cr}$ may depend on stratification as well. At $E = 10^{-5}$, the multipolar branch is rather uninhabited at $Ro_\ell < Ro_{\ell cr}$. The only case found was very close to onset of dynamo action, where the convection is almost laminar and the Lorentz force is simply too weak to sustain a strong axisymmetric magnetic field. In addition, no bistable or lower *Pm* multipoles were found (even $Pm = 0.5$ results in a dipole-dominated field, but bistability was not investigated systematically). The reason for this void in the lower branch may be the decreased strength of absolute zonal flow amplitude, even though the relative strength, represented here by Z, is similar. This will be discussed further in the next section.

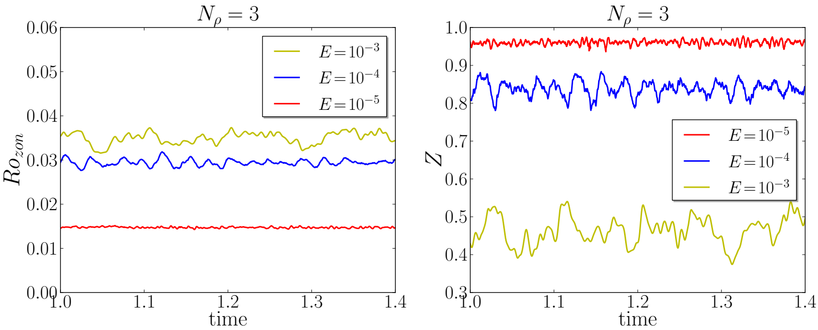

Figure 4.8: Time series of zonal Rossby number (left panel) and relative zonal flow amplitude Z (right panel). The three lines correspond to the three different Ekman numbers 10^{-3} (yellow), 10^{-4} (blue) and 10^{-4} (red). The time is given in viscous time.

At Ekman number $E = 3 \times 10^{-5}$ (panel **d.**), bistability cases were not investigated extensively either (dotted lines), but the two branches exist nonetheless. For the two dipolar cases at $N_\rho = 4$ and two different Rayleigh numbers, it was tested whether there is a complementary multipolar solution. Starting from a multipolar and weaker field amplitude configuration revealed absence of the multipolar branch for the case with higher Rayleigh number, though it exists for the lower *Ra*. This is due to the fact that the convection is not vigorous enough at the lower *Ra* to build and sustain the strong field of an axisymmetric dipole when starting from a weak multipolar field. In panel **d.** of Fig. 4.6, the lower branch contains mainly simulations of $Pm = 1$ and most of the $Pm = 2$ cases occupy the dipolar branch. This confirms the dependence on magnetic Prandtl number suggested in the previous section for $E = 10^{-4}$. Similar to the case with the higher Ekman number (see previous section), strong stratifications N_ρ or higher *Pm* cases dominate the upper dipolar branch. In the corresponding $E = 3 \times 10^{-5}$ panel **d.** of Fig. 4.7, where the symbols have the same meaning as in Fig. 4.6, the zonal flow amplitude differs from the $E = 10^{-4}$ cases described previously, since no solutions in the multipolar branch with weaker zonal flow Z (cyan area) were found in either panels **d.** or **e.** of Fig. 4.7. This can be explained by non-magnetic models. Figure 4.8 displays three cases at Ekman numbers 10^{-3}, 10^{-4} and 10^{-5} with supercriticalities 2.9, 4.3 and 4.5, respectively. The left panel shows the Rossby number of the zonal flows, which measures their absolute amplitude and the right panel corresponds to Z, a relative measure. It is seen here that the even though the cases selected have a value of Ro_{zon} that decreases with decreasing E, the value of Z actually increases with E. Thus the relative importance of the zonal flow increases with decreasing E, but not its absolute value. This also explains the dipole-dominated solutions at low Ekman number and mild density stratifications, since the absolute zonal flow amplitude is weaker there. The topic of the role of the zonal flows is explored further in the next section.

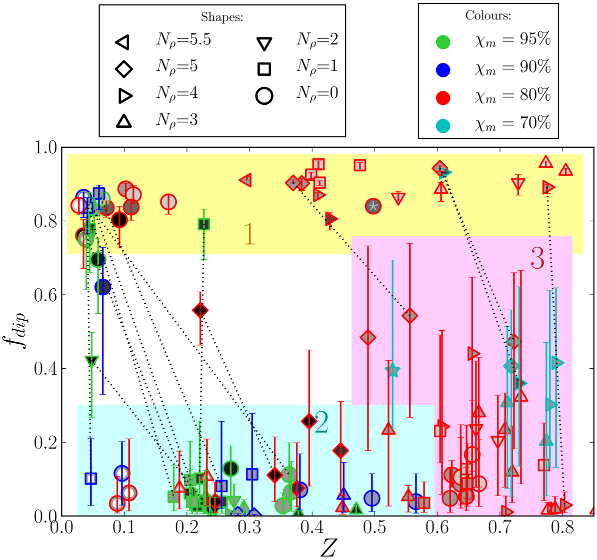

Figure 4.9: Dipolarity plotted against the ratio between the azimuthal kinetic energy and the total kinetic energy Z, averaged in time and volume, for all the cases of Fig. 4.7. The symbols and colours have the same definition as in Fig. 4.6. The three boxes mark the same three different regimes of Fig. 4.2 with the sole purpose of serving as a reference, for comparison. The dotted lines connect sets of cases for which we found two solutions, depending on the initial magnetic field. This image was adapted from Duarte et al. (2013).

Figure 4.9 compiles all the simulations in one plot to confirm that the three regimes 1 (yellow area), 2 (cyan area) and 3 (pink area) hold independently of Ekman number, since the relative amplitude of zonal flow Z is comparable between different Ekman numbers. The previous section shows a higher difficulty to find dipole-dominated solutions due to the larger scale of convection that hampers layer separation discussed in Chapter 3. The dipolar solutions at higher values of N_ρ are then only possible at higher values of Pm with increasing E (e.g. left top panel of Fig. 4.7, for $E = 10^{-3}$ and $Pm = 10$). For higher values of Pm, the average dipolarity is lower, which has also been observed by other authors (Sreenivasan and Jones 2011, Schrinner et al. 2012). At higher Pm, due to the lower magnetic diffusivity, the energy cascade leading to dissipation is less efficient and the smaller scales of the magnetic field prevail in the spectrum, with higher energy than the lower Pm cases. This effect of Pm on the dipolarity f_{dip} is seen in the top panels of Fig. 4.7 (**a.** and **b.**), where the dipole solutions are stable but at lower averaged values of f_{dip}. These two dipoles are $Pm = 10$, $E = 10^{-3}$, $N_\rho = 2$, $\chi_m = 95\%$ in panel **a.** and $Pm = 10$, $E = 3 \times 10^{-4}$, $N_\rho = 5$, $\chi_m = 80\%$ in panel **b.**. Another illustration of this effect of higher Pm is the case of $Pm = 5$, $E = 10^{-4}$, $N_\rho = 0$, $\chi_m = 90\%$ in panel **c.**.

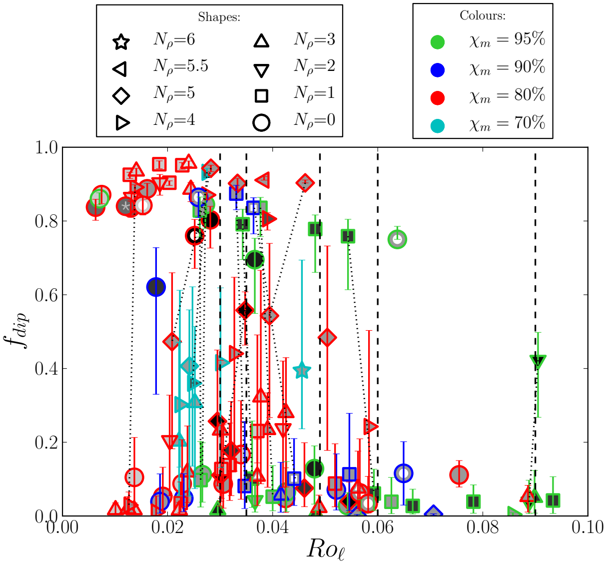

Figure 4.10: Dipolarity against the local Rossby number defined by Eq. (2.50). The symbols and colours have the same definition as in Fig. 4.6. The plot contains all the simulations in the five panels of Fig. 4.6, with a dashed line marking the value of $Ro_{\ell cr}$ for each E, which increases with E (see Fig. 4.11 and discussion in the text). This image was adapted from Duarte et al. (2013).

Figure 4.10 is also a compilation of the results in a plot of dipolarity against local Rossby number Ro_ℓ (similar to Fig. 4.6). This plot shows that the transition $Ro_{\ell cr}$ (dashed lines) between the two regimes depends on Ekman number. This is shown directly in a plot of $Ro_{\ell cr}$ against E in Fig. 4.11. The least squares fit done for the five values of $Ro_{\ell cr}$ shows a clear polynomial dependence on E, which does not agree with the results presented by Christensen and Aubert (2006) for models with aspect ratio $\eta = 0.35$, $N_\rho = 0$ and no-slip boundaries, though the reason for this is not yet understood. If we were to extrapolate this scaling law to Jupiter's $E_{♃} \approx 5 \times 10^{-19}$ (French et al. 2012), the transitional value would be $Ro_{\ell cr ♃} \approx 1.94 \times 10^{-5}$. Using the interior flow velocity estimated by Jones (2003) of $U_{♃} \approx 2 \times 10^{-3}$ m/s and Jupiter's angular velocity of $\Omega_{♃} \approx 1.76 \times 10^{-4}$ rad/s in Eq. 2.48, the prediction for the length scale of the flow is $\sim 0.85\%$ of the planetary radius.

In conclusion, dipolar dynamo action is possible. It can be conciliated with strong relative zonal flows when the weakly conducting layer is combined with a significant

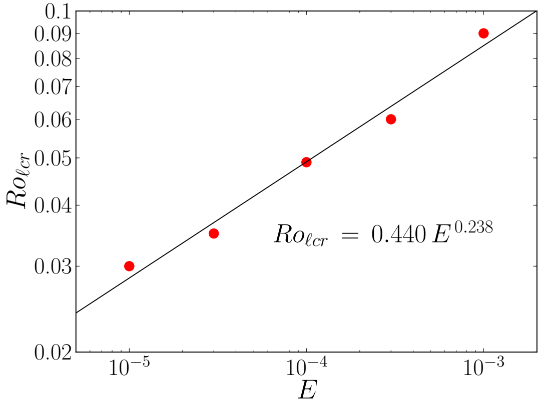

Figure 4.11: Critical local Rossby number $Ro_{\ell cr}$ plotted against Ekman number E. The values of $Ro_{\ell cr}$ correspond to the dashed lines of Fig. 4.10.

stratification. The required degree of stratification increases with Ekman number.

4.1.2 The role of zonal flows

The coexistence of dipolar and multipolar branches indicates a competition between zonal winds and dipolar magnetic fields already discussed in Chapter 3 (see also Gastine et al. 2012). The stronger Lorentz forces associated to the larger dipolar fields effectively compete with the Reynolds stresses responsible for driving the zonal winds. The zonal wind amplitude and the relative zonal wind energy thus remain typically small. Fierce zonal winds, on the other hand, seem to promote multipolar fields. This is at least the situation for $E = 10^{-4}$ and $\chi_m = 95\%$ or 90%. But why are stronger stratifications and/or larger magnetic Prandtl numbers required to yield dipole-dominated dynamo action for thicker weakly conducting outer layers?

Figure 4.12 illustrates the zonal flow structure and the poloidal magnetic field lines for different stratifications at $\chi_m = 95\%$ (middle row) and $\chi_m = 80\%$ (bottom row) for $E = 10^{-4}$. The top row shows non-magnetic cases and demonstrates that the inner retrograde jet decreases in amplitude when the stratification intensifies. This reflects the progressive outward concentration of the convective motions and thus of the Reynolds stresses driving the zonal flows (Chapter 3).

The dominance of Coriolis forces at this relatively low Ekman number enforces the Taylor-Proudman theorem and the intense zonal jets remain strongly geostrophic, i.e. variations in the direction of the rotation axis are much smaller than variations perpendicular to it. For the thinner weakly conducting layer (middle row in Fig. 4.12), the Lorentz forces associated with the stronger dipolar field at mild stratifications effectively suppress the zonal flows in the whole shell. For $N_\rho > 2$, the weaker multipolar fields created by the thin-shell dynamo allow the outer prograde jet to survive, albeit with a significantly

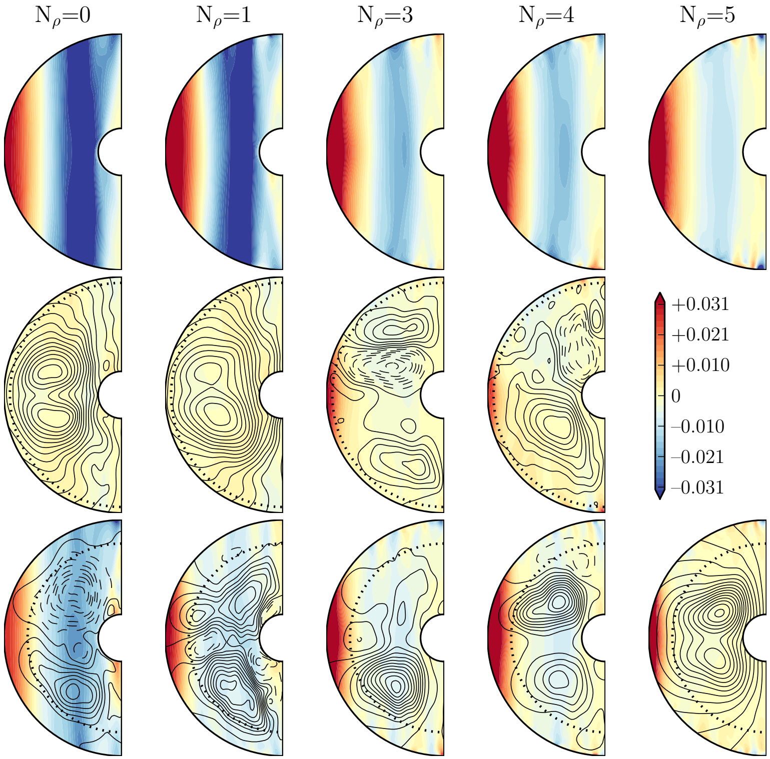

Figure 4.12: Azimuthal averages of the zonal component of the flow. Each column of three plots has a different N_ρ, namely 0, 1, 3, 4 and 5 from left to right. In the bottom and middle rows, the poloidal field lines are plotted on top of the zonal velocity contours in units of Rossby number $Ro = u/(\Omega r_o)$. The dotted line in the middle and bottom rows corresponds to $r_m = 95\%$ and $r_m = 80\%$, respectively. The top row shows the corresponding hydrodynamical solutions. This image was taken from Duarte et al. (2013).

reduced amplitude and a restricted width than in the non-magnetic simulations. The thickness of the weakly conducting layer now determines the width of the outer jet, confirming previous work by Heimpel and Gómez-Pérez (2011).

At $\chi_m = 80\%$ (lower row in Fig. 4.12), the zonal flows generally remain more energetic than for $\chi_m = 95\%$. Since these flows are largely geostrophic, the force balances on geostrophic cylinders (i.e. on cylinders aligned with the rotation axis) should be considered. The Lorentz forces now have a harder time to brake the zonal flows since they act in a significantly reduced volume. Dipole-dominated dynamo action only becomes possible when the retrograde inner zonal jet is already relatively weak in the non-magnetic simulations, which happens at stronger stratifications. The thin-shell dynamo mechanism generating the multipolar field for $\chi_m \geq 90\%$ does not apply here, since it would have to operate, at least partly, in the weakly conducting layer where the magnetic Reynolds number is now too low to support dynamo action. Instead, a strongly dipolar magnetic field is generated in the deeper interior where it does not interfere with the remaining prograde outer zonal jet.

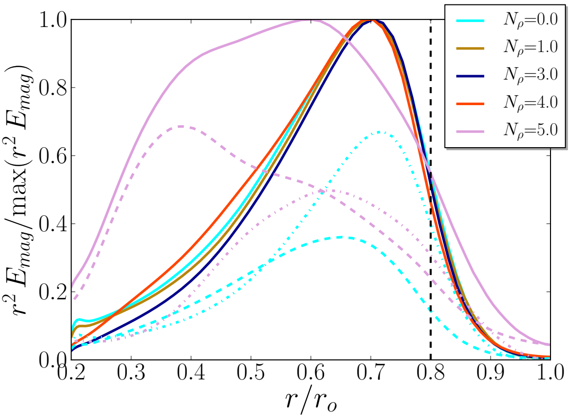

Figure 4.13: Radial profile of magnetic energy flux ($r^2\,E_{mag}$) averaged over time. The dashed black line is the location of $\chi_m = 80\%$. These results correspond to the red triangles and red dashed line from Fig. 4.4. The poloidal (dashed lines) and toroidal (dot-dashed lines) components are also shown for $N_\rho = 5$ and $N_\rho = 0$, with the corresponding colours. The magnetic energy fluxes are normalized by their maximum values. This image was taken from Duarte et al. (2013).

The change in the depth of the poloidal dynamo action is further illustrated by the radial profiles of magnetic energy shown in Fig. 4.13. Up to a stratification of $N_\rho = 4$, poloidal and toroidal magnetic energies have similar profiles and peak in the outer part of the conducting region around $r/r_o \simeq 0.7$. For $N_\rho = 5$, however, the profiles are different with a pronounced focus on deeper parts of the shell around $r/r_o = 0.4 - 0.6$. For $N_\rho \leq 4$, the toroidal magnetic field is larger than the poloidal, suggesting that the induction mechanism is different from the dipole-dominated case at $N_\rho = 5$ where the poloidal field is stronger.

At $\chi_m = 70\%$, the volume over which Lorentz forces can efficiently brake zonal winds is even further reduced. Dipolar solutions can only be found at even larger stratification than at $\chi_m = 80\%$ where the driving of the inner zonal jet is yet weaker.

The role of Lorentz forces in defeating zonal winds and thereby enabling dipole-dominated magnetic fields also offers an explanation why larger magnetic Prandtl numbers help. The reason likely is that larger Pm values lead to stronger magnetic fields and thus stronger Lorentz forces. We can also now interpret the highly time-dependent solutions with intermediate mean dipolarities. Here, the balance seems to be undecided (Fig. 4.3). Stronger Lorentz forces successfully suppress the zonal winds at times but never enough to establish the solution on the highly dipolar more stable branch. At other times, Reynolds stresses succeed in driving stronger zonal flows that mostly create a weaker multipolar magnetic field.

4.1.2.1 Influence of rigid outer boundary condition

To further test the theory that the zonal flows are decisive for the field geometry we ran a few $E = 10^{-4}$ cases with a no-slip outer boundary condition that largely prevents zonal flows from developing. The results are mixed and not entirely conclusive, which may have to do with the fact that other flow components are also affected by this change in boundary conditions. At $\chi_m = 95\%$, $N_\rho = 0$ and $Ra/Ra_{cr} = 23$, the no-slip boundary conditions indeed promote a dipole-dominated solution with weak zonal flows where we only find multipolar solutions with strong zonal flows for a free-slip outer boundary condition (green circles in Fig. 4.1, of which two have the same parameters with the exception of the outer mechanical boundary condition; stars mark the no-slip cases in this figure). The same positive effect was found for $\chi_m = 90\%$, $N_\rho = 0$ and $Ra/Ra_{cr} = 11.5$ (blue circles in Fig. 4.1). At $\chi_m = 90\%$, $N_\rho = 1$ and $Ra/Ra_{cr} = 5.2$, however, we find bistable cases for both types of boundary conditions (two blue squares in Fig. 4.1 with a star inside and joined by a dashed line). In the no-slip case, both the dipole-dominated and the multipolar solution have weak zonal flows. A free-slip outer boundary condition promotes dipolarity, but it is not a necessary condition to find this feature. Note that such a bistable case for no-slip conditions has already been reported by Christensen and Aubert (2006).

At $\chi_m = 80\%$, $N_\rho = 0$ and $Ra/Ra_{cr} = 23.0$, the suppression of the zonal flows by the no-slip condition is not sufficient to yield a dipole-dominated solution and the same is true at $\chi_m = 80\%$, $N_\rho = 3$ and $Ra/Ra_{cr} = 3.2$ or $Ra/Ra_{cr} = 4.3$ (all three cases with $Pm = 2$). In the latter two examples, the particular thin shell dynamo described in Chapter 3 (see also Gastine et al. 2012), rather than the stronger zonal flows, may be the reason for the multipolarity which could explain why the no-slip condition has no effect.

4.1.2.2 Higher conductivity decay

We also varied the electrical conductivity profile in a few cases. Increasing the exponential decay rate from $a = 9$ to $a = 25$ for two simulations at $\chi_m = 80\%$, one with $N_\rho = 3$ and the other $N_\rho = 5$, required a finer radial numerical grid and thus more expensive numerical simulations. The zonal flows in the weakly conducting layer were intensified in both cases, likely because of the further decreased weaker Lorentz forces there. The type of solution, however, remained unchanged.

We also tested a more realistic electrical conductivity profile that models the approximately linear decrease of electrical conductivity in the metallic layer and a steeper decrease at larger radii (grey profile in Fig. 2.3). At $\chi_m = 80\%$, $N_\rho = 5$ and $Ra/Ra_c = 9.3$ the solution is bistable for our standard conductivity profile. For the more realistic profile we found a clearly dipole-dominated solution at the same supercriticality but in a subcritical-type regime, i.e. the dynamo only survives if the initial condition for the magnetic field is already a strong axisymmetric dipole field. Figure 4.14 compares the radial profiles of the convective magnetic Reynolds number Rm_{conv} for both profiles (yellow lines and grey line). Being based on rms flows velocities that exclude zonal winds, Rm_{conv} is appropriate

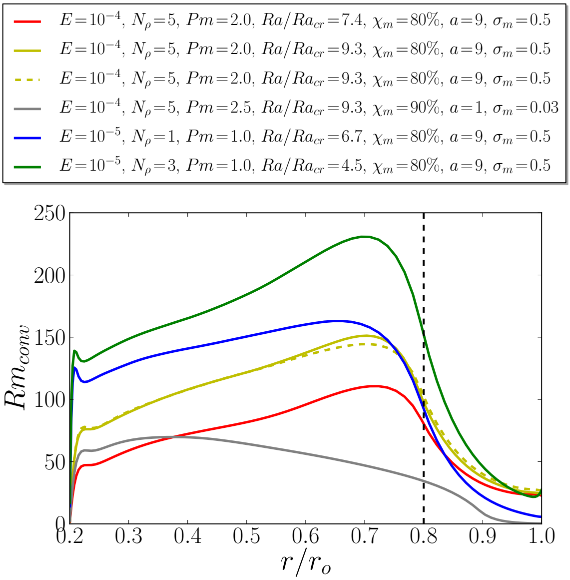

Figure 4.14: The radial profiles of convective magnetic Reynolds number averaged over time for the cases displayed in Fig. 4.12. The two additional yellow cases yield a higher *Ra* and bistability, at $N_\rho = 5$ and $E = 10^{-4}$. This image was taken from Duarte et al. (2013).

for characterizing poloidal magnetic field production. Numerical simulations suggest that a magnetic Reynolds number larger than 50 is usually required to support dynamo action (Christensen and Aubert 2006). For our standard electrical conductivity profiles, Rm_{conv} typically falls below this value for radii beyond $r/r_o = 0.85$ or 0.9. The linear decrease in the metallic layer, however, further reduces the convective Reynolds number which is already very low at depth. Rm_{conv} values larger than 50 are now restricted to the inner region of $r/r_o < 0.6$. A multipolar dynamo where the outer parts of the shell play a sizeable role thus becomes unlikely. In Jupiter, Rm_{conv} is generally significantly higher in the metallic region ($\sim 10^{-5}$, Jones 2003) and only decreases below the critical value for dynamo action in the molecular envelope. We therefore refrained from further exploring this profile since the decrease in magnetic Reynolds number artificially limits the dynamo region.

Figure 4.15 shows zonal flows and axisymmetric poloidal field lines for the dipole-dominated solutions at $E = 10^{-4}$ with the modified electrical conductivity profile (first panel from the left) and the standard profile (second panel). The poloidal fields are very similar and produced at greater depth in both cases. This explains why the low convective magnetic Reynolds number in the outer part of the shell has little impact on the dynamo mechanism for dipole-dominated solutions. Once more, the weaker Lorentz force in the outer layer allows for more vigorous zonal winds for the more realistic conductivity profile.

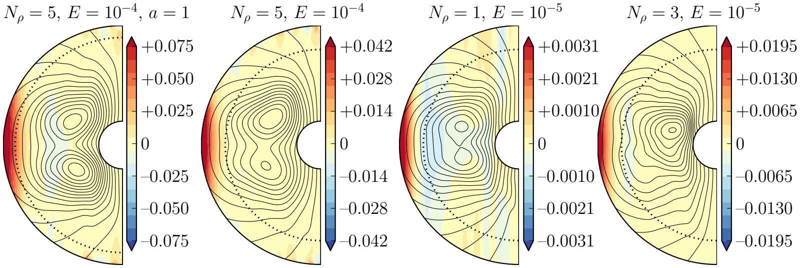

Figure 4.15: Azimuthal average of the zonal component of the flow. The cases displayed here are, from left to right: grey and red profiles of Fig. 4.14 with $E = 10^{-4}$, blue and green profiles of Fig. 4.14 with $E = 10^{-5}$. The poloidal field lines are plotted on top of the zonal velocity contours, where solid lines are positive and dashed are negative values. The dotted lines correspond to the value of χ_m. Zonal velocities are given in units of Rossby number calculated by $Ro = u/(\Omega r_o)$. This image was taken from Duarte et al. (2013).

4.1.2.3 Zonal flows at other Ekman numbers

How do the results at $E = 10^{-5}$ fit into the picture we outlined above? Figure 4.15 compares two $E = 10^{-5}$ cases at $N_\rho = 1$ (third panel from the left) and $N_\rho = 3$ (fourth panel) with the dipole-dominated solutions for the more realistic profile (first panel) and for our standard profile at $N_\rho = 5$ and $E = 10^{-4}$ (second panel, see also Fig. 4.12). The magnetic field and zonal flow structures are very similar in all cases. At both Ekman numbers, the relative amplitude of the retrograde jets decreases with increasing N_ρ. The absolute zonal flow amplitude, however, is significantly smaller in all lower Ekman number models. For example, the zonal flow Rossby number is $Ro_{zon} = 5.2 \times 10^{-3}$ in the $E = 10^{-5}$ / $N_\rho = 3$ case depicted in Fig. 4.15, but $Ro_{zon} = 1.4 \times 10^{-2}$ in the $E = 10^{-4}$ / $N_\rho = 5$ simulation in the same figure.

In non-magnetic free-slip simulations, the flow amplitude roughly scales with the modified Rayleigh number $Ra^\star = Ra\,E^2/Pr$, as it has been shown by Christensen (2002) for Boussinesq and Gastine and Wicht (2012) for anelastic models. For example, Gastine and Wicht (2012) suggest the dependence $Ro \approx 0.165\,{Ra^\star}^{1.06}$. This scaling describes an asymptotic behaviour for larger Rayleigh numbers where zonal flows clearly dominate so that $Ro \approx Ro_{zon}$. For the smaller Rayleigh numbers typically examined here, it may only serve as a rough estimate for the zonal flow amplitude. For the case of the second panel of Figure 4.15 ($E = 10^{-4}$), we have $Ra^\star = 0.4$ and the scaling predicts $Ro_{zon} \approx 6.2 \times 10^{-2}$. For the case of the fourth panel ($E = 10^{-5}$ and $Ra^\star = 0.04$) it predicts $Ro_{zon} \approx 5.4 \times 10^{-3}$. Both values are not too far from the numerical results $Ro_{zon} \approx 1.4 \times 10^{-2}$ and $Ro_{zon} \approx 5.2 \times 10^{-3}$, respectively, which suggests that the difference in $Ra^\star$ is indeed the main reason for the much weaker zonal flows at the lower Ekman number.

Because of the quadratic Ekman number dependence of $Ra^\star$, Ra has to be increased by two orders of magnitude to reach the same zonal flow amplitudes in the $E = 10^{-5}$ as in the $E = 10^{-4}$ cases. This leads to larger Ro_ℓ values and thus possibly multipolar fields (Heimpel and Gómez-Pérez 2011). The Rayleigh number increase from $Ra/Ra_{cr} = 10$ to $Ra/Ra_{cr} = 16.7$ at $N_\rho = 1$ already leads to a multipolar field while only doubling the zonal flow amplitude.

The similar Elsasser numbers in the dipole-dominated cases at both Ekman numbers indicate that the Lorentz forces also have comparable amplitudes. These forces have a much easier job to brake the systematically weaker zonal flows at $E = 10^{-5}$, allowing a dipole-dominated field to develop even at mild stratifications. The more extensive parameter study at $E = 10^{-4}$ suggests that stronger stratifications should allow for more vigorous outer jets while retaining dipole-dominated dynamo action.

4.1.3 Dynamo Mechanism

Figure 4.16 compares $\overline{B}_\phi$, Ω (Eq. 2.38) and MD (Eq. 2.39) for two $\chi_m = 80\%$ cases: a multipolar solution at $N_\rho = 3$ (left column) and dipole-dominated solution at $N_\rho = 5$ (right column). Both cases were depicted previously in Figs. 4.12 and 4.13. For the multipolar solution, the Ω-effect plays an important role, as demonstrated by the high degree of correlation with the azimuthal field over the shell. For the dipole-dominated solution, however, the Ω-effect is only strong in the weakly conducting region where it is effectively balanced by the large ohmic diffusion. The change in field geometry is thus once more coupled to a switch from an $\alpha\Omega$ or $\alpha^2\Omega$ mechanism at weaker stratifications to an α^2 mechanism at stronger density stratifications.

4.2 Conclusions

In this Chapter, we ran a suite of dynamo simulations with an electrical conductivity profile geared to combine the dynamics of the metallic and the molecular hydrogen layers of the gas giants in one integrated model. In most models, the conductivity is assumed to remain constant over the inner part of the shell representing the metallic hydrogen region. Beyond a relative radius of χ_m, it decays exponentially with radius, to model the molecular envelope. The use of the anelastic MHD code allowed us to also study the effects of density stratification. Free-slip outer boundary and no-slip inner boundary conditions seem appropriate for the gas giants and were used in the majority of our simulations.

In the previous Chapter, we explored the dynamo action for homogeneous electrical conductivity in an otherwise identical setup. Dipole dominated solutions were only found for mild stratifications and local Rossby numbers below $Ro_{\ell cr} = 0.08$. The respective solution branch is characterized by weak zonal winds and coexists with a second branch with weaker multipolar magnetic fields but stronger zonal winds at identical parameters. This indicates a competition between zonal winds and dipolar magnetic fields (Simitev and Busse 2009, Schrinner et al. 2012, Gastine et al. 2012). Translated to Jupiter and Saturn, these simulations would predict multipolar magnetic fields, should the observed zonal winds reach into the dynamo region. The strong stratification within the gas giants should also promote multipolar solutions.

We largely recover these results when the outer weakly conducting layer occupies only 5 or 10 percent in radius ($\chi_m = 95\%$ and $\chi_m = 90\%$). However, the critical local Rossby

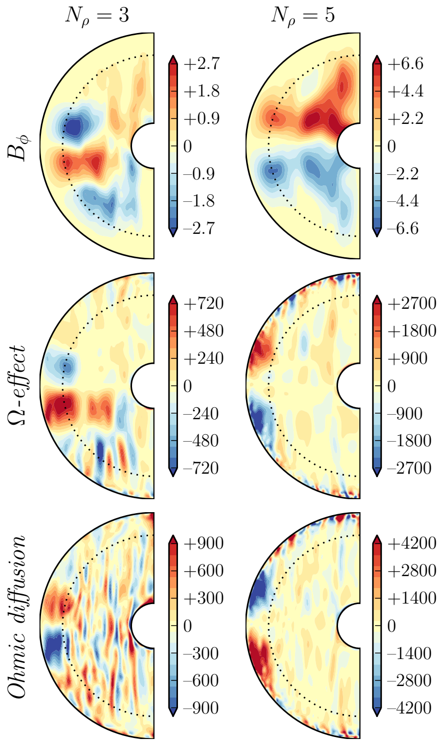

Figure 4.16: From top to bottom, azimuthal averages of the toroidal component of the magnetic field, production of the toroidal field by Ω-effect and ohmic diffusion. The three left panels correspond to $N_\rho = 3$, $Ra/Ra_{cr} = 4.3$ and the three right panels to $N_\rho = 5$, $Ra/Ra_{cr} = 7.4$, both cases belong to the red $\chi_m = 80\%$ line of Fig. 4.4. This image was taken from Duarte et al. (2013).

number, below which dipole-dominated solutions are possible, decreases to $Ro_{\ell cr} \approx 0.04$. Gómez-Pérez et al. (2010) already showed that even very thin weakly conducting outer layers promote multipolar magnetic field configurations. They speculate that the separation of the Ekman and Hartmann boundary layers may play a role in their models with no-slip boundaries, although this explanation is difficult to apply to the free-slip models predominantly explored here. More research is required to clarify this point in the future, specially concerning no-slip boundaries.

For a thicker weakly conducting outer layer covering the outer 20 or 30% in radius (χ_m = 80% or 70%), the volume over which the Lorentz forces can act to balance Reynolds stresses is more significantly reduced. The competition between zonal wind and stronger dipolar fields thus becomes even more of an issue. At an Ekman number of $E = 10^{-4}$, the mean zonal winds tend to be relatively strong even at low Rayleigh numbers. Dipole-dominated dynamo action is nevertheless possible in the deeper interior of strongly stratified models, where the zonal flows remain relatively weak even in the non-magnetic case. Alternatively, dipole-dominated solutions are found for larger magnetic Prandtl numbers which help to keep zonal flows at bay by increasing Lorentz forces. In the dipole-dominated solutions, the zonal winds are then mainly restricted to a fierce prograde jet that resides within the weakly conducting outer envelope.

At the lower Ekman number of $E = 10^{-5}$, dipole-dominated magnetic fields can even be maintained at weak stratifications because the zonal flow amplitudes are lower than at $E = 10^{-4}$. The peak velocity of Jupiter's equatorial jet is around $Ro_{ej} = 1.1 \times 10^{-2}$ (Vasavada and Showman 2005) and about $Ro_{ej} = 5.0 \times 10^{-2}$ for Saturn (Choi et al. 2009). For example, the $E = 10^{-4}$ case illustrated in Fig. 4.15 (second panel from the left) reaches $Ro_{ej} = 5.3 \times 10^{-2}$ which is somewhat too high for Jupiter. The $E = 10^{-5}$ simulation depicted in the same figure has $Ro_{ej} = 2.4 \times 10^{-2}$ at the lower stratification of $N_\rho = 3$. The amplitude of the equatorial jet decreases with Ekman number and increases with density stratification. We speculate that the higher stratifications within the gas giants may allow to reach appropriate zonal jet amplitudes at the much lower realistic Ekman number, around $E_J \sim 5 \times 10^{-19}$ (French et al. 2012), while retaining dipole-dominated dynamo action.

The number of zonal jets is much smaller in our simulations than for the gas giants. Also, the strong decrease in the zonal flow amplitude from the equatorial to the flanking jets, that is necessary to retain dipole-dominated dynamo action in our models, is not compatible with the observations for Jupiter. A dipolar configuration nevertheless seems possible should the higher latitude jets remain too shallow to interfere with the deeper dynamo process. The equatorial jet does not pose a problem in this respect because it can reside completely within the lower conductivity envelope.

An argument against deep reaching winds is that the associated strong Ω-effect and Ohmic dissipation may not be compatible with Jupiter's observed luminosity (Liu et al. 2008). A first analysis of our results confirms that the Ω-effect and associated Ohmic dissipation can be significant. Glatzmaier (2008) argues that the magnetic field may assume a configuration where the poloidal field lines are aligned with the rotation axis in regions of strong zonal flow shear. Since the shear is perpendicular to the rotation axis, this would minimize the Ω-effect and related Ohmic dissipation. Figure 4.15 illustrates that the field lines indeed approach such an alignment in the very outer part of the shell where the electrical conductivity is still important. The Ohmic dissipation nevertheless remains significant in all our simulations with strong zonal flows. Further investigation is necessary to quantify this effect and extrapolate it to the planetary situation.

Any problems related to ohmic dissipation and dipolar dynamo action would not be an issue when stronger zonal winds remain confined to a thin outer envelope with ($\chi_m \geq 96\%$), where the electrical conductivity remains small enough (Liu et al. 2008). In our simulations, however, all the stronger jets obey the Taylor-Proudman theorem and reach through the planet. Shallow jets have been found by Kaspi et al. (2009), who use a different anelastic approximation and a different internal heating mode. Further investigations are required to clarify which specific model features influence the depth on the zonal jets.

5 Scaling laws

5.1 Introduction

The parameters used in today's numerical models are still orders of magnitude far from the realistic values of fluid cores of astrophysical bodies. For example, numerical models work with values of Rayleigh number a few orders of magnitude too small, since planetary fluids are known to be much more turbulent and smaller scale (see Tab. 2.1 in Chapter 2). Such deficiency of the present computational models is compensated with much too high viscosity, translated into an Ekman number at least ten orders of magnitude too large for actual planetary values. This use of unrealistic parameters naturally makes us question the force balances of the numerical models compared to the force balances in planetary cores, since the viscosity might be playing a more important role in the models than in reality.

Most past studies of scaling laws were based on a magnetostrophic balance, i.e. comparable magnitude of Lorentz and Coriolis forces with an additional leading order contribution of buoyancy and negligible from inertia and viscosity (see the review of Christensen 2010). Such a balance would imply an Elsasser number (the ratio between Lorentz and Coriolis) of order unity, but a much broader range can be found in numerical models of the last decade. Christensen and Aubert (2006) propose scaling laws based on the energy required to maintain a magnetic field, i.e. the buoyancy power available to balance ohmic dissipation (Christensen and Aubert 2006).

Former studies like Christensen and Aubert (2006)'s were meant to model the geodynamo, by considering a Bousinesq approximation with no-slip boundaries. In these cases there is an absence of complex dynamical phenomena like the presence of the two-attractors (Simitev and Busse 2009, Schrinner et al. 2012, Gastine and Wicht 2012, Yadav et al. 2013a), that introduces a second possible force balance for the same set of parameters resulting in magnetic field amplitudes and morphologies different from the dipolar magnetic fields observed for planets like Earth, Jupiter and Saturn. This happens when simply applying free-slip boundary conditions to Boussinesq models. Yadav et al. (2013a) showed that it is already possible to clearly separate the two different solutions in two distinct scaling laws, of dipolar dynamos and multipolar dynamos.

In the present work and following Yadav et al. (2013b), radially varying parameters were added, namely the density and electrical conductivity of the fluid (see Chapters 3 and 4). The motivation for this set of data was described in the previous sections and in Gastine et al. (2012) and Duarte et al. (2013) and it is a first step towards more realistic models of the gas giants.

Following Yadav et al. (2013b), their same scaling laws are applied here for the full database in order to test them only on the dataset discussed in the previous two chapters. Yadav et al. (2013b) included part of this dataset in theirs and successfully matched the scaling laws, so the results presented in the next sections are simply a summary with a slight expansion of the dataset within the same parameter regimes.

5.2 Flow velocity

The non-dimensional power generated by buoyancy forces is given by

$$Pow = Ra^* \frac{\int_{r_i}^{r_o} \langle\, u_r \tilde{\rho}(r)\, g\, s \rangle\, r^2\, \mathrm{d}r}{\int_{r_i}^{r_o} \langle \tilde{\rho}(r) \rangle\, r^2\, \mathrm{d}r}, \tag{5.1}$$

where Ra^* is a modified version of the Rayleigh number independent of diffusivities due to the negligible role of viscous forces expected in planetary cores (Christensen and Aubert 2006),

$$Ra^* = Ra\, \frac{E^2}{Pr}, \tag{5.2}$$

where Ra, E and Pr are defined in Chapter 2.

Figure 5.1 shows how the Rossby number scales with a combination of power Pow and magnetic Prandtl number Pm for the results discussed in the previous Chapters. On the x-axis, the quantity is $Pow/Pm^{13/45}$, following the empirical scaling proposed by Yadav et al. (2013b) as a best fit. The thin black like surrounding the symbols marks the cases with homogeneous electrical conductivity discussed in Chapter 3 and the thicker outer line of colour shows the cases from Chapter 4 with a variable electrical conductivity profile that transitions to an exponential decay in the outer part of the shell at four different radii (cyan – 70%, red – 80%, blue – 90%, green – 95%). The Rossby number is this figure was calculated from the total flow inside the shell,

$$Ro = \frac{u}{\Omega\, d}, \quad \text{with} \quad u = \sqrt{\frac{3}{r_o^3 - r_i^3} \int_{r_i}^{r_o} \langle u^2 \rangle\, r^2\, \mathrm{d}r}\,. \tag{5.3}$$

The scatter in Fig. 5.1 is primarily due to the part of the flow velocity related to the zonal flows. This is clear when removing this component, which results in the flow velocity related to convective motions alone and it can be seen in Fig. 5.2. Here, only Ro_{conv} is plotted against the quantity $Pow/Pm^{13/45}$ and the scatter is greatly reduced. There is still a small offset for a group of cases with $N_\rho \geq 3.0$ and various variable electrical conductivity profiles, though also for some with homogeneous conductivity. For lack of a systematic trend, it is only possible to speculate about a less efficient quenching of the convective flow by the magnetic field, due to a large variety of magnetic field geometries.

The best linear fit shown in the plot of Fig. 5.2 is

$$Ro_{conv} = 1.99\, \frac{Pow^{0.43}}{Pm^{0.13}}, \tag{5.4}$$

which agrees well with the results of Yadav et al. (2013a) of $Ro_{conv} = 2.49\, Pow^{0.45}/Pm^{0.13}$ for a more diverse dataset, that includes also radius-dependent diffusivities, different aspect ratios and different mechanical boundary conditions.

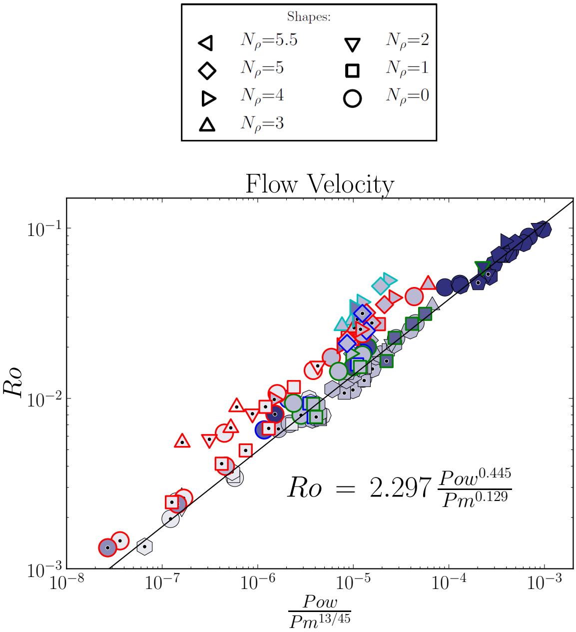

Figure 5.1: Total Rossby number versus buoyancy power with a dependence on $Pm^{13/45}$, following Yadav et al. (2013b). The colours of the outer lines of the symbols represent the different variable conductivity profiles: cyan – χ_m = 70%, red – χ_m = 80%, blue – χ_m = 90%, green – $\chi_m = 95\%$, thin black - homogeneous conductivity. The shapes of the symbols indicate different values of N_ρ, as described in the legend. The different shades of inner colour of the symbols correspond to a gradient of magnetic Prandtl number, where darker means higher values of Pm (maximum is $Pm = 10.0$ and minimum is $Pm = 1.0$). The black dot inside the symbols marks the stable dipole-dominated magnetic field solutions. The black line corresponds to a least squares polynomial fit applied to the data points and the resulting equation is given in the plot.

5.3 Magnetic Field

An exact balance of the two forces, Lorentz and Coriolis, would correspond to an Elsasser number of one, which is not something that is observed often and consistently in this work, even though it lives in the range of 0.1–10.0 (Stevenson 2003). This may be due to a number of aspects like a more complex action of the magnetic field on the convective motions, an eventual alignement between magnetic field and velocity or the balance of Coriolis force mostly by pressure gradients instead of electromagnetic forces. Additionally, the energetics of the dynamo process are not taken into account, thus a scaling law

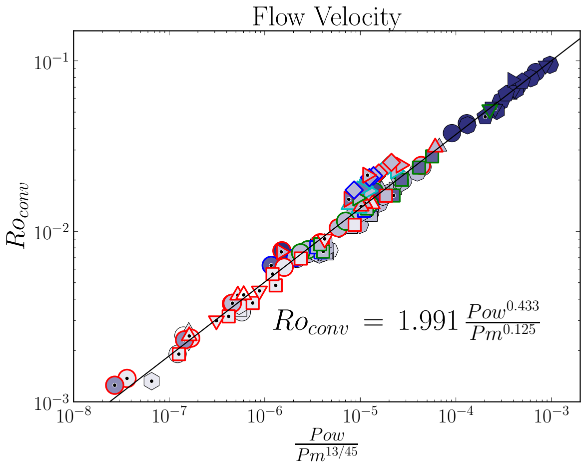

Figure 5.2: Convective Rossby number versus buoyancy power with a dependence on $Pm^{13/45}$, following Yadav et al. (2013b). The colours and shapes of the symbols and outer lines are the same as in Fig. 5.1. The black line corresponds to a least squares linear fit applied to the data points and the resulting equation is given in the plot.

based on Lorentz number alone, defined as

$$Lo = \frac{3}{(r_o^3 - r_i^3)} \int_{r_i}^{r_o} \left\langle \frac{\mathbf{B}^2}{\tilde{\rho}(r)} \right\rangle r^2 \, \mathrm{d}r, \tag{5.5}$$

is not sufficient, since it is necessary to take into account the amount of power available to be converted to magnetic energy and lost due to ohmic dissipation. This quantity is directly related to the magnetic field strength and geometry and may be represented by the ohmic fraction f_{Ohm}, which corresponds to the ratio of Ohmic dissipation to buoyancy power.

The Ohmic dissipation is the rate at which magnetic energy is dissipated per unit mass, given by

$$Ohm = \frac{E}{Pm} \frac{\int_{r_i}^{r_o} \langle \tilde{\lambda}(r) \, (\nabla \times \mathbf{B})^2 \rangle \, r^2 \, \mathrm{d}r}{\int_{r_i}^{r_o} \langle \tilde{\rho}(r) \rangle \, r^2 \, \mathrm{d}r} \tag{5.6}$$

and the amount of power generated by buoyancy and used to balance magnetic dissipation is then the fraction between Eqs. 5.6 and 5.1,

$$f_{Ohm} = \frac{Ohm}{Pow} = \frac{Pr}{Pm \, Ra \, E} \frac{\int_{r_i}^{r_o} \langle \tilde{\lambda}(r) \, (\nabla \times \mathbf{B})^2 \rangle \, r^2 \, \mathrm{d}r}{\int_{r_i}^{r_o} \langle u_r \, \tilde{\rho}(r) \, g \, s \rangle \, r^2 \, \mathrm{d}r}. \tag{5.7}$$

Once more, Fig. 5.3 follows the results of Yadav et al. (2013b), where two different scaling laws were found for dipole-dominated magnetic fields and for multipolar. The dipolar branch will be applied to Jupiter in the next section.

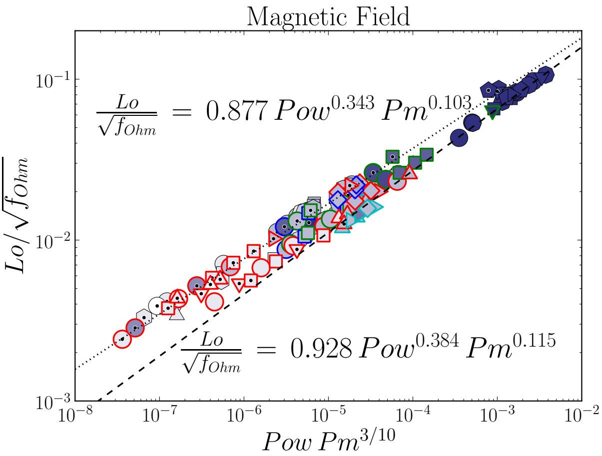

Figure 5.3: Lorentz number versus buoyancy power with a dependence on $Pm^{3/10}$, following Yadav et al. (2013b). The colours and shapes of the symbols and outer lines are the same as in Fig. 5.1. The black line corresponds to a least squares polynomial fit applied to the data points and the resulting equation is given in the plot.

5.4 Application to Jupiter

To complete this Chapter and conclude this work, it is important to see how the scaling laws for the flow velocity and the magnetic field developed by Yadav et al. (2013b) apply to Jupiter. The scaling laws obtained from fitting the data of Chapters 3 and 4 are the polynomial nondimensional relations displayed in Figs. 5.2 and 5.3,

$$Ro_{conv} = 1.991\,\frac{Pow^{0.433}}{Pm^{0.125}}, \tag{5.8}$$

$$\left.\frac{Lo}{\sqrt{f_{Ohm}}}\right|_{dip} = 0.877\,Pow^{0.343}Pm^{0.103}, \tag{5.9}$$

where only the convective part of the bulk flow velocity is calculated, since a scaling including the axisymmetric part of the toroidal flow introduces too much scatter to be reliable (see section 5.2).

A few simplifications still need to be done to determine actual planetary values from Eqs. 5.8 and 5.9, following Jones (2003). The multiplying factors 1.991 and 0.877 are approximated by 2 and 0.9, respectively and the exponents of Pow are replaced by the result of the fractions $0.433 \approx 3/7$ and $0.343 \approx 1/3$. Finally, the Pm dependence is dropped since its exponent is close to zero for both equations. Another reason to neglect the magnetic Prandtl number is the aim of the scaling laws presented in this Chapter of not accounting for diffusivities, since Pm is a ratio between thermal and magnetic. The simplified relations become

$$Ro_{conv} = 2\,Pow^{3/7} \Rightarrow U_{conv} = 2\,\Omega\,d\,Pow^{3/7}, \tag{5.10}$$

$$Lo_{dip} = 0.9\,Pow^{1/3} \Rightarrow B = 0.9\,Lo\,\Omega\,d\,\sqrt{\rho\mu_0}\,Pow^{1/3}, \tag{5.11}$$

where f_{Ohm} is often assumed unity, which would be the ideal case where the magnetic energy is much larger than the kinetic energy and the magnetic diffusivity is very high (Christensen and Aubert 2006).

The heat flux observed at the surface of Jupiter is 5.4 watt/m^2 (Guillot 2005), which gives a power of 8.3×10^{16} watt or, in dimensionless form (see section 5.2), 2.6×10^{-15}. The angular velocity is $\Omega_{♃} \approx 1.76 \times 10^{-4}$ rad/s and the convective shell thickness is $d_{♃} \approx 5.6 \times 10^7$ m. The latter is obtained by assuming aspect ratio $\eta = 0.2$, the value used throughout this thesis, and determining the thickness from $d_{♃} = (1 - \eta)\,R_{♃}$, where $R_{♃} = 6.99 \times 10^7$ m. Eq. 5.10 gives a convective flow velocity in the bulk of $U_{conv} \approx 11$ cm/s. Jones (2003) predicted a velocity in the interior of 0.2 m/s, thus the result from the scaling law shown here is acceptable. The observed meridional velocity at the surface is close to 2 orders of magnitude greater, though the uncertainty is great since values measured are of the same magnitude as the errors that affect the observations (Sánchez-Lavega et al. 2004). Nonetheless the difference might come from the fact that the scaling gives a mean value for the whole interior and it is known from the models described in the previous Chapters that a free-slip outer boundary tends to allow stronger flows to build at the surface.

The Lorentz number predicted from Eq. 5.11 and $Pow_{♃} = 2.6\times10^{-15}$ is $Lo_{dip\,♃} = 1.24\times10^{-5}$. Using now also the value of magnetic permeability for vacuum of $\mu_0 = 1.26 \times 10^{-6}$ N/A^2 and the average density of $\rho_{♃} = 1400$ kg/m^3, the magnetic field amplitude according to Eq. 5.11 is $B \sim 6.4$ mT, around one order of magnitude larger than the observed surface value of 0.4 mT (Khurana et al. 2004). Once again, the difference may arise due to the fact that the field is stronger in the interior and an average of the bulk is higher than the value outside the planet.

Summary and outlook

The interior of a gas giant planet is known to be mostly composed of hydrogen. The commonly accepted three-layer model consists of a small inner rocky core, an intermediate fluid hydrogen layer and an outer molecular hydrogen envelope. The high pressures and temperatures reached between 80 and 90% of the planetary radius result in a phase transition of hydrogen to a metallic state. The electrical conductivity, however, increases rapidly with depth due to the growing degree of ionisation. The transition to the metallic state happens at temperatures beyond the critical point and there is no abrupt change in electrical conductivity nor in any other property. The dynamo is thought to operate in the deeper regions, where the conductivity is large enough.

The density increase across the interior of the giant gas planets is estimated to be a few orders of magnitude. Many numerical models for the interior dynamics have nevertheless neglected the stratification for simplicity in a so-called Boussinesq approximation. This thesis and the related publications represent the first systematic explanation of the effects of density stratification in a planetary context.

The goal of this work is to systematically explore the effects of density stratification and electrical conductivity variations in numerical models. The anelastic version of the MHD code MagIC is used, which solves for convection and magnetic field generation in a rotating spherical shell. The anelastic approach assumes a nearly adiabatic stratification (which could be expected due to the efficient convective mixing), where convection induces variations in the thermodynamic variables that are much smaller than the values of the adiabatic background state. A big advantage of this approximation is that sound waves can be neglected, which could severely slow down numerical calculations due to their high speed relatively to the significantly slower convective motions.

Even when the density contrast (ratio between inner and outer boundary densities, ρ_i/ρ_o) is mild, it already affects the dynamics. The scale of convection decreases considerably with increasing density stratification across the shell radius. The entropy gradient in the outer part of the shell grows more rapidly, which also alters the location of the axial convective motions by moving them toward the outer boundary.

For the majority of the simulations a free-slip mechanical outer boundary condition is used which is more appropriate for gas planets than the rigid boundary used for terrestrial dynamos. The free-slip condition allows strong zonal winds to develop with the consequence that two distinct solution attractors can coexist at identical parameters. The dipolar attractor is characterized by a strong axial dipolar magnetic field with weak zonal flows. On the other hand, the multipolar attractor accommodates a weak multipolar magnetic field and strong zonal flows. Which attractor a numerical solution chooses depends on the initial magnetic field. The two attractor scenario only applies to mild density contrasts, however, typically below $\rho_i/\rho_o \sim 7$ when the convection takes place mostly attached to the inner boundary. At higher values, the convection columns are located at the outer boundary. Mean-field models showed that such a confinement prefers large non-axisymmetric fields. The dynamo is thus of the multipolar type and zonal flows are always strong.

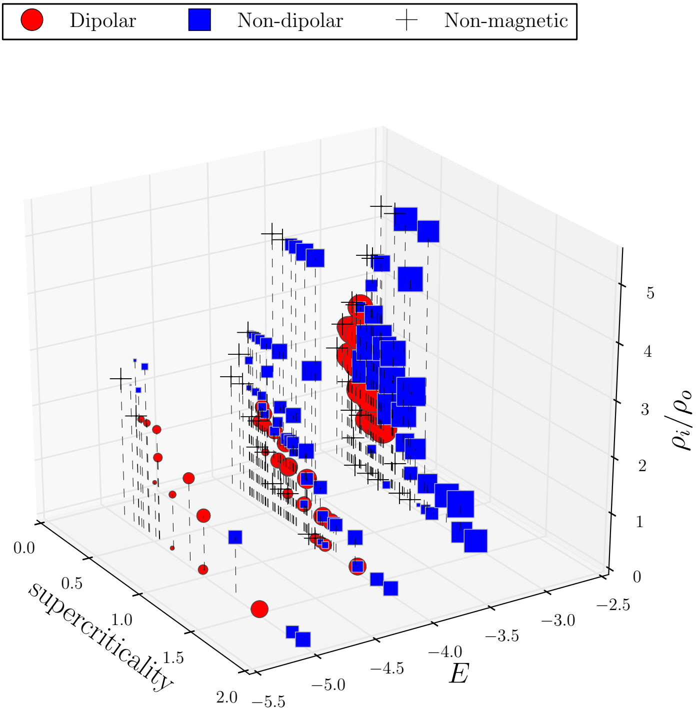

Figure 5.4: Density contrast versus supercriticality of the system, for different rotation rates, quantified by the Ekman number E, the ratio of viscous to Coriolis forces. The values of the axes are given in logarithmic scale, base 10 for x- and y- and base e for z-axes. The red circles correspond to dipole-dominated magnetic fields, the blue squares are multipolar fields and the crosses represent failed dynamos. This figure compiles Figs. 3.24, 3.7 and 3.27.

The ratio of inertia to Coriolis effects was used in the past to separate dipolar from multipolar dynamos. The former is dominated by columnar convection, i.e. the convective motions are almost two-dimensional, where the helical flow along the columns is responsible for generating a dipole-dominated magnetic field. In multipolar dynamos, inertia was significant in the force balance and due to higher turbulence the flow becomes less organized. This method of separating the two regimes was vastly used in the past, but it is found here that its applicability to anelastic models with free-slip boundary is

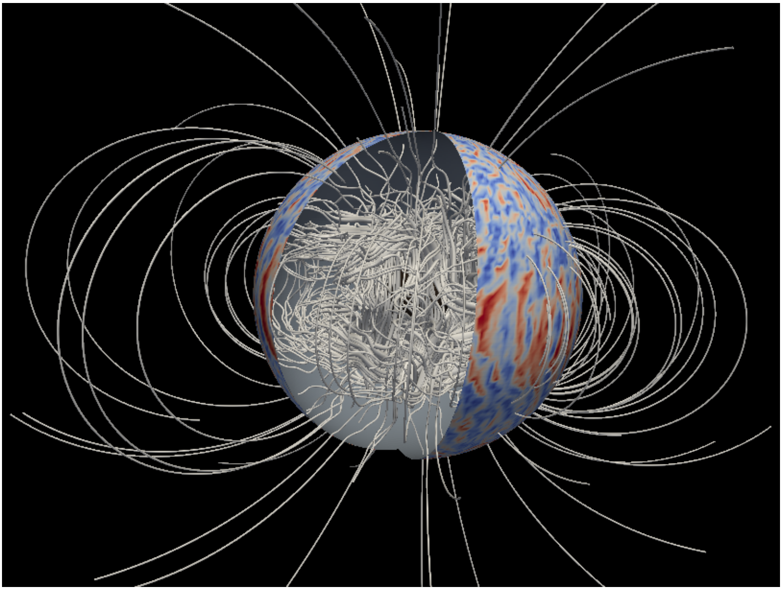

Figure 5.5: 3D rendering of a simulation with variable density and electrical conductivity along radius. The magnetic field lines in silver, where the radius of the tube is scaled by the magnitude of the magnetic energy. Contours of the surface velocity are shown where blue roughly represents retrograde and red prograde directions.

questionable since the density stratification and the mechanical boundary condition also play a role.

In a second step an electrical conductivity profile was introduced. The profile starts to matter when the thickness of the weakly conducting outer layer is at east 80% of the total shell. At contrasts in the range $\rho_i/\rho_o \approx 1 - 55$, the zonal flow driven by Reynolds stresses (result from non-linear inertial effects) and promoted by the free-slip outer boundary (where the magnetic field has now little to no influence) becomes strong enough to penetrate the inner conducting layer and play a dominant role in the dynamo mechanism. Such models are time-dependent, oscillating randomly between multipolar and dipolar dynamos. Increasing the density contrast further to ~ 150, with the same electrical conductivity gradient, revealed a more relevant setup for a gas giant where both the strong zonal winds and the dipolar field coexist. This is possible because the amplitude of the zonal flow in the bulk is found to become weaker with increasing density stratification even in non-magnetic models.

In such dipole-dominated models, the equatorial jet remains confined to the outer weakly conducting layer, while the dipolar dynamo resides in the inner conducting part. However, the higher latitude jets are weak. If these were stronger, they would likely cross the whole shell and inhibit the generation of a dipole-dominated dynamo.

Future work is required to expand the present database both to clarify the dependences on rotation and density gradients found in this thesis, as well as to explore the effects of other parameters. These may include the geometry of the domain, the shape of the gradients, the ratios of diffusivities, different driving mechanisms and different boundary conditions. The effects of radial dependencies for further properties may also be explored. As an example, if the thermal conductivity/diffusivity were to increase considerably outward, convection might be favoured near the inner boundary even at high density contrasts thus possibly allowing dipolar dynamo action to prevail independently of the stratification.

A Table of results

Table A.1: Summary of the time-averaged results:
- models 1-80: non-magnetic cases ($^*Rm$ is replaced by Re)
- models 81–240 and 365–405: homogeneous conductivity
- models 241–364: variable conductivity

BC=1: free-slip outer boundary
BC=2: no-slip outer boundary

Model	η	BC	N_ρ	E	Ra/Ra_{cr}	Pr	Pm_i	χ_m	σ_m	a	f_{dip}	SD_{dip}	Rm^*	Ro	Ro_ℓ	Λ	Λ_ℓ	Z
1	0.20	1	0.0	1.0E-3	4.0	1.0	0.0	–	–	–	–	–	18	1.82E-2	2.18E-2	–	–	0.29
2	0.20	1	3.0	1.0E-3	2.6	1.0	0.0	–	–	–	–	–	40	4.09E-2	1.07E-1	–	–	0.45
3	0.20	1	3.0	1.0E-3	2.9	1.0	0.0	–	–	–	–	–	51	5.19E-2	1.34E-1	–	–	0.47
4	0.20	1	0.5	1.0E-3	4.8	1.0	0.0	–	–	–	–	–	32	3.29E-2	6.35E-2	–	–	0.21
5	0.20	1	0.0	1.0E-4	23.0	1.0	0.0	–	–	–	–	–	672	3.36E-2	4.49E-2	–	–	0.84
6	0.20	1	1.0	1.0E-4	10.3	1.0	0.0	–	–	–	–	–	755	3.78E-2	5.96E-2	–	–	0.84
7	0.20	1	3.0	1.0E-4	4.3	1.0	0.0	–	–	–	–	–	644	3.23E-2	6.73E-2	–	–	0.84
8	0.20	1	3.0	1.0E-4	8.6	1.0	0.0	–	–	–	–	–	1473	7.37E-2	1.44E-1	–	–	0.86
9	0.20	1	4.0	1.0E-4	6.6	1.0	0.0	–	–	–	–	–	397	3.98E-2	1.07E-1	–	–	0.83
10	0.20	1	5.0	1.0E-4	7.4	1.0	0.0	–	–	–	–	–	328	3.28E-2	1.56E-1	–	–	0.73
11	0.20	1	5.0	1.0E-4	9.3	1.0	0.0	–	–	–	–	–	440	4.41E-2	1.84E-1	–	–	0.76
12	0.20	1	0.0	1.0E-5	6.3	1.0	0.0	–	–	–	–	–	284	2.86E-3	3.76E-3	–	–	0.90
13	0.20	1	1.0	1.0E-5	6.6	1.0	0.0	–	–	–	–	–	593	5.97E-3	8.23E-3	–	–	0.92
14	0.20	1	3.0	1.0E-5	4.5	1.0	0.0	–	–	–	–	–	1500	1.50E-2	2.00E-2	–	–	0.96
15	0.20	1	0.0	3.0E-6	25.4	0.1	0.0	–	–	–	–	–	2692	8.08E-3	9.15E-3	–	–	0.95
16	0.20	1	0.0	1.0E-3	2.0	1.0	0.0	–	–	–	–	–	10	1.06E-2	1.18E-2	–	–	0.22
17	0.20	1	0.0	1.0E-3	2.6	1.0	0.0	–	–	–	–	–	12	1.34E-2	1.28E-2	–	–	0.23
18	0.20	1	0.0	1.0E-3	3.3	1.0	0.0	–	–	–	–	–	15	1.61E-2	1.61E-2	–	–	0.31
19	0.20	1	0.0	1.0E-3	5.3	1.0	0.0	–	–	–	–	–	24	2.46E-2	3.53E-2	–	–	0.33
20	0.20	1	0.0	1.0E-3	6.6	1.0	0.0	–	–	–	–	–	31	3.14E-2	5.27E-2	–	–	0.27
21	0.20	1	0.5	1.0E-3	1.9	1.0	0.0	–	–	–	–	–	10	1.06E-2	1.26E-2	–	–	0.19

Continued on next page

Model	η	BC	N_ρ	E	Ra/Ra_{cr}	Pr	Pm_i	χ_m	σ_m	a	f_{dip}	SD_{dip}	Rm^*	Ro	Ro_ℓ	Λ	Λ_ℓ	Z
22	0.20	1	0.5	1.0E-3	4.8	1.0	0.0	–	–	–	–	–	29	3.24E-2	6.25E-2	–	–	0.23
23	0.20	1	1.0	1.0E-3	1.8	1.0	0.0	–	–	–	–	–	10	1.01E-2	1.27E-2	–	–	0.19
24	0.20	1	1.0	1.0E-3	2.2	1.0	0.0	–	–	–	–	–	12	1.28E-2	1.41E-2	–	–	0.16
25	0.20	1	1.5	1.0E-3	1.7	1.0	0.0	–	–	–	–	–	8	8.66E-3	1.44E-2	–	–	0.19
26	0.20	1	2.0	1.0E-3	1.3	1.0	0.0	–	–	–	–	–	8	8.37E-3	1.90E-2	–	–	0.11
27	0.20	1	2.5	1.0E-3	1.5	1.0	0.0	–	–	–	–	–	15	1.55E-2	4.42E-2	–	–	0.23
28	0.20	1	3.0	1.0E-3	1.8	1.0	0.0	–	–	–	–	–	14	2.04E-2	6.30E-2	–	–	0.30
29	0.20	1	3.0	1.0E-3	2.0	1.0	0.0	–	–	–	–	–	18	2.50E-2	7.09E-2	–	–	0.36
30	0.20	1	3.0	1.0E-3	2.7	1.0	0.0	–	–	–	–	–	44	4.43E-2	1.15E-1	–	–	0.45
31	0.20	1	4.0	1.0E-3	2.5	1.0	0.0	–	–	–	–	–	27	2.76E-2	1.09E-1	–	–	0.31
32	0.20	1	4.0	1.0E-3	2.8	1.0	0.0	–	–	–	–	–	22	3.59E-2	1.42E-1	–	–	0.31
33	0.20	1	5.0	1.0E-3	3.3	1.0	0.0	–	–	–	–	–	38	3.80E-2	2.19E-1	–	–	0.20
34	0.20	1	5.0	1.0E-3	4.5	1.0	0.0	–	–	–	–	–	54	5.43E-2	2.73E-1	–	–	0.26
35	0.20	1	0.0	1.0E-3	3.3	1.0	0.0	–	–	–	–	–	21	3.06E-2	5.14E-2	–	–	0.18
36	0.20	1	0.0	1.0E-3	7.9	1.0	0.0	–	–	–	–	–	35	3.82E-2	6.24E-2	–	–	0.23
37	0.20	1	0.0	1.0E-3	9.2	1.0	0.0	–	–	–	–	–	44	4.79E-2	7.72E-2	–	–	0.33
38	0.20	1	2.5	1.0E-3	1.8	1.0	0.0	–	–	–	–	–	24	2.51E-2	6.30E-2	–	–	0.35
39	0.20	1	3.0	1.0E-3	1.8	1.0	0.0	–	–	–	–	–	19	1.98E-2	6.19E-2	–	–	0.29
40	0.20	1	3.0	1.0E-3	2.2	1.0	0.0	–	–	–	–	–	29	2.95E-2	8.10E-2	–	–	0.38
41	0.20	1	3.0	1.0E-3	2.6	1.0	0.0	–	–	–	–	–	39	4.01E-2	1.08E-1	–	–	0.41
42	0.20	1	5.0	1.0E-3	11.2	1.0	0.0	–	–	–	–	–	117	1.18E-1	5.96E-1	–	–	0.17
43	0.20	1	5.0	3.0E-4	13.2	10.0	0.0	–	–	–	–	–	28	8.68E-3	9.67E-2	–	–	0.09
44	0.20	1	0.0	1.0E-4	3.4	1.0	0.0	–	–	–	–	–	24	2.51E-3	4.31E-3	–	–	0.43
45	0.20	1	0.0	1.0E-4	5.7	1.0	0.0	–	–	–	–	–	41	4.20E-3	6.57E-3	–	–	0.62
46	0.20	1	0.0	1.0E-4	6.9	1.0	0.0	–	–	–	–	–	52	5.34E-3	8.18E-3	–	–	0.67
47	0.20	1	0.0	1.0E-4	7.2	1.0	0.0	–	–	–	–	–	50	5.26E-3	1.11E-2	–	–	0.38
48	0.20	1	0.0	1.0E-4	7.5	1.0	0.0	–	–	–	–	–	59	6.06E-3	9.31E-3	–	–	0.69
49	0.20	1	0.0	1.0E-4	7.8	1.0	0.0	–	–	–	–	–	63	6.53E-3	9.98E-3	–	–	0.70

Continued on next page

Model	η	BC	N_ρ	E	Ra/Ra_{cr}	Pr	Pm_i	χ_m	σ_m	a	f_{dip}	SD_{dip}	Rm^*	Ro	Ro_ℓ	Λ	Λ_ℓ	Z
50	0.20	1	0.0	1.0E-4	8.0	1.0	0.0	–	–	–	–	–	65	6.76E-3	1.06E-2	–	–	0.69
51	0.20	1	0.0	1.0E-4	9.2	1.0	0.0	–	–	–	–	–	62	6.62E-3	1.97E-2	–	–	0.06
52	0.20	1	0.5	1.0E-4	3.6	1.0	0.0	–	–	–	–	–	30	3.06E-3	6.26E-3	–	–	0.51
53	0.20	1	0.5	1.0E-4	4.4	1.0	0.0	–	–	–	–	–	30	3.10E-3	6.15E-3	–	–	0.54
54	0.20	1	0.5	1.0E-4	5.1	1.0	0.0	–	–	–	–	–	55	5.61E-3	1.41E-2	–	–	0.46
55	0.20	1	1.0	1.0E-4	2.6	1.0	0.0	–	–	–	–	–	23	2.36E-3	5.73E-3	–	–	0.35
56	0.20	1	1.0	1.0E-4	3.1	1.0	0.0	–	–	–	–	–	34	3.43E-3	7.92E-3	–	–	0.55
57	0.20	1	1.5	1.0E-4	2.3	1.0	0.0	–	–	–	–	–	26	2.70E-3	8.23E-3	–	–	0.46
58	0.20	1	1.5	1.0E-4	2.7	1.0	0.0	–	–	–	–	–	43	4.39E-3	1.10E-2	–	–	0.60
59	0.20	1	2.0	1.0E-4	1.4	1.0	0.0	–	–	–	–	–	9	9.69E-4	3.42E-3	–	–	0.18
60	0.20	1	2.0	1.0E-4	1.9	1.0	0.0	–	–	–	–	–	26	2.67E-3	1.20E-2	–	–	0.35
61	0.20	1	2.5	1.0E-4	1.7	1.0	0.0	–	–	–	–	–	47	4.80E-3	1.85E-2	–	–	0.57
62	0.20	1	3.0	1.0E-4	2.2	1.0	0.0	–	–	–	–	–	77	7.71E-3	2.26E-2	–	–	0.73
63	0.20	1	5.0	1.0E-4	3.7	1.0	0.0	–	–	–	–	–	98	9.85E-3	9.59E-2	–	–	0.48
64	0.20	1	5.0	1.0E-4	4.7	1.0	0.0	–	–	–	–	–	142	1.42E-2	1.12E-1	–	–	0.55
65	0.20	1	2.0	1.0E-5	2.2	1.0	0.0	–	–	–	–	–	63	6.38E-4	4.55E-3	–	–	0.51
66	0.20	1	2.5	1.0E-5	1.6	1.0	0.0	–	–	–	–	–	729	7.30E-3	7.25E-3	–	–	0.00
67	0.20	1	0.0	1.0E-3	2.0	1.0	0.0	–	–	–	–	–	10	1.06E-2	1.18E-2	–	–	0.22
68	0.20	1	0.0	1.0E-3	2.6	1.0	0.0	–	–	–	–	–	12	1.34E-2	1.28E-2	–	–	0.23
69	0.20	1	0.0	1.0E-3	3.3	1.0	0.0	–	–	–	–	–	15	1.61E-2	1.61E-2	–	–	0.31
70	0.20	1	0.0	1.0E-3	5.3	1.0	0.0	–	–	–	–	–	22	2.42E-2	3.50E-2	–	–	0.31
71	0.30	1	0.0	1.0E-3	2.5	1.0	0.0	–	–	–	–	–	13	1.35E-2	1.64E-2	–	–	0.28
72	0.30	1	0.0	1.0E-3	5.1	1.0	0.0	–	–	–	–	–	24	2.50E-2	5.19E-2	–	–	0.27
73	0.30	1	0.0	1.0E-3	5.9	1.0	0.0	–	–	–	–	–	31	3.15E-2	6.75E-2	–	–	0.26
74	0.35	1	0.0	1.0E-3	2.8	1.0	0.0	–	–	–	–	–	14	1.49E-2	1.95E-2	–	–	0.29
75	0.35	1	0.0	1.0E-3	3.7	1.0	0.0	–	–	–	–	–	16	1.71E-2	3.42E-2	–	–	0.32
76	0.35	1	0.0	1.0E-3	4.7	1.0	0.0	–	–	–	–	–	24	2.44E-2	5.63E-2	–	–	0.29
77	0.35	1	0.0	1.0E-3	5.6	1.0	0.0	–	–	–	–	–	29	2.94E-2	7.44E-2	–	–	0.21

Continued on next page

Model	η	BC	N_ρ	E	Ra/Ra_{cr}	Pr	Pm_i	χ_m	σ_m	a	f_{dip}	SD_{dip}	Rm^*	Ro	Ro_ℓ	Λ	Λ_ℓ	Z
78	0.45	1	0.0	1.0E-3	2.2	1.0	0.0	–	–	–	–	–	11	1.14E-2	2.17E-2	–	–	0.28
79	0.55	1	0.0	1.0E-3	1.8	1.0	0.0	–	–	–	–	–	8	8.50E-3	2.67E-2	–	–	0.17
80	0.70	1	0.0	1.0E-3	1.5	1.0	0.0	–	–	–	–	–	6	6.09E-3	4.28E-2	–	–	0.01
81	0.20	1	0.0	1.0E-3	4.0	1.0	10.0	1.00	–	–	5.36E-3	9.16E-3	168	1.77E-2	2.04E-2	1.539	0.045	0.19
82	0.20	1	0.0	1.0E-3	7.9	1.0	10.0	1.00	–	–	1.14E-2	1.61E-2	385	3.87E-2	6.50E-2	0.425	0.011	0.28
83	0.20	1	0.0	1.0E-3	9.2	1.0	10.0	1.00	–	–	2.14E-2	2.67E-2	431	4.33E-2	7.66E-2	2.906	0.071	0.24
84	0.20	1	0.0	1.0E-3	10.6	1.0	10.0	1.00	–	–	1.59E-2	1.80E-2	435	4.70E-2	9.09E-2	5.673	0.126	0.16
85	0.20	1	0.0	1.0E-3	19.8	1.0	10.0	1.00	–	–	2.30E-2	2.43E-2	733	7.36E-2	1.56E-1	19.736	0.337	0.08
86	0.20	1	0.0	1.0E-3	26.4	1.0	10.0	1.00	–	–	1.93E-2	2.21E-2	885	8.89E-2	1.91E-1	27.421	0.408	0.07
87	0.20	1	0.0	1.0E-4	9.2	1.0	2.0	1.00	–	–	7.87E-1	9.38E-2	124	6.62E-3	1.97E-2	1.382	0.075	0.06
88	0.20	1	0.0	1.0E-4	10.3	1.0	2.0	1.00	–	–	7.75E-1	7.82E-2	141	7.10E-3	2.22E-2	1.871	0.097	0.06
89	0.20	1	0.0	1.0E-4	10.3	1.0	2.0	1.00	–	–	2.63E-1	1.61E-1	170	8.57E-3	2.16E-2	0.475	0.026	0.42
90	0.20	1	0.0	1.0E-4	11.5	1.0	2.0	1.00	–	–	8.17E-1	6.33E-2	141	7.58E-3	2.61E-2	2.328	0.121	0.05
91	0.20	1	0.0	1.0E-4	11.5	1.0	2.0	1.00	–	–	8.11E-2	7.31E-2	187	9.38E-3	2.66E-2	0.649	0.034	0.35
92	0.20	1	0.0	1.0E-4	23.0	1.0	2.0	1.00	–	–	8.78E-1	1.94E-2	244	1.31E-2	5.74E-2	5.446	0.222	0.04
93	0.20	1	0.0	1.0E-4	23.0	1.0	2.0	1.00	–	–	3.06E-2	3.04E-2	339	1.70E-2	6.22E-2	2.545	0.097	0.24
94	0.20	1	0.0	1.0E-4	34.5	1.0	2.0	1.00	–	–	2.88E-2	3.74E-2	449	2.25E-2	8.48E-2	4.482	0.140	0.22
95	0.20	1	0.0	1.0E-4	45.9	1.0	2.0	1.00	–	–	4.74E-2	5.59E-2	551	2.76E-2	1.02E-1	5.971	0.164	0.25
96	0.20	1	0.0	1.0E-5	4.8	1.0	1.0	1.00	–	–	9.39E-1	1.14E-3	96	1.01E-3	5.52E-3	0.149	0.012	0.10
97	0.20	1	0.0	1.0E-5	9.6	1.0	1.0	1.00	–	–	6.92E-1	8.51E-2	195	1.96E-3	1.46E-2	1.186	0.070	0.05
98	0.20	1	0.0	1.0E-5	33.1	1.0	1.0	1.00	–	–	8.69E-1	1.63E-2	332	3.32E-3	2.79E-2	4.908	0.219	0.03
99	0.20	1	0.0	1.0E-5	49.7	1.0	1.0	1.00	–	–	8.87E-1	1.72E-2	470	4.71E-3	4.27E-2	5.475	0.214	0.03
100	0.20	1	0.0	1.0E-5	66.3	1.0	1.0	1.00	–	–	7.94E-2	7.54E-2	732	7.33E-3	6.17E-2	3.721	0.124	0.06
101	0.20	1	0.0	1.0E-5	82.9	1.0	1.0	1.00	–	–	3.93E-2	2.55E-2	820	8.21E-3	7.09E-2	5.738	0.174	0.02
102	0.20	1	0.0	1.0E-5	9.6	1.0	0.5	1.00	–	–	7.81E-1	3.77E-2	123	2.48E-3	1.32E-2	0.469	0.033	0.03
103	0.20	1	0.5	1.0E-3	2.9	1.0	10.0	1.00	–	–	1.33E-2	1.70E-2	157	1.58E-2	1.95E-2	1.864	0.062	0.11
104	0.20	1	0.5	1.0E-3	6.7	1.0	10.0	1.00	–	–	2.70E-2	2.97E-2	459	4.61E-2	9.75E-2	5.777	0.140	0.18
105	0.20	1	0.5	1.0E-3	9.5	1.0	10.0	1.00	–	–	5.42E-2	6.24E-2	611	6.14E-2	1.42E-1	14.818	0.296	0.11

Continued on next page

Model	η	BC	N_ρ	E	Ra/Ra_{cr}	Pr	Pm_i	χ_m	σ_m	a	f_{dip}	SD_{dip}	Rm^*	Ro	Ro_ℓ	Λ	Λ_ℓ	Z
106	0.20	1	0.5	1.0E-3	14.3	1.0	10.0	1.00	–	–	4.11E-2	4.60E-2	815	8.18E-2	1.96E-1	26.379	0.442	0.07
107	0.20	1	0.5	1.0E-3	19.0	1.0	10.0	1.00	–	–	2.30E-2	2.81E-2	979	9.82E-2	2.36E-1	37.017	0.555	0.07
108	0.20	1	1.0	1.0E-3	2.6	1.0	10.0	1.00	–	–	6.11E-1	9.22E-2	172	1.74E-2	3.26E-2	10.624	0.392	0.06
109	0.20	1	1.0	1.0E-3	2.9	1.0	10.0	1.00	–	–	5.57E-1	8.19E-2	213	2.15E-2	4.28E-2	13.586	0.440	0.04
110	0.20	1	1.0	1.0E-3	3.6	1.0	10.0	1.00	–	–	4.64E-1	7.99E-2	276	2.77E-2	6.32E-2	19.753	0.569	0.04
111	0.20	1	1.0	1.0E-3	5.8	1.0	10.0	1.00	–	–	1.93E-2	2.80E-2	552	5.54E-2	1.37E-1	11.813	0.267	0.12
112	0.20	1	1.0	1.0E-3	7.3	1.0	10.0	1.00	–	–	1.43E-2	1.89E-2	680	6.82E-2	1.72E-1	16.593	0.333	0.10
113	0.20	1	1.0	1.0E-3	2.9	1.0	5.0	1.00	–	–	7.77E-1	6.04E-2	109	2.20E-2	4.69E-2	3.905	0.213	0.04
114	0.20	1	1.0	1.0E-3	4.4	1.0	5.0	1.00	–	–	2.06E-2	2.45E-2	191	4.26E-2	8.88E-2	0.801	0.031	0.31
115	0.20	1	1.5	1.0E-3	2.3	1.0	10.0	1.00	–	–	4.94E-1	8.66E-2	202	2.04E-2	4.50E-2	18.595	0.659	0.05
116	0.20	1	1.5	1.0E-3	2.8	1.0	10.0	1.00	–	–	3.64E-1	8.21E-2	282	2.93E-2	6.84E-2	31.021	0.835	0.05
117	0.20	1	1.5	1.0E-3	4.5	1.0	10.0	1.00	–	–	2.86E-1	6.37E-2	471	5.19E-2	1.44E-1	35.237	0.777	0.04
118	0.20	1	1.5	1.0E-3	5.7	1.0	10.0	1.00	–	–	5.76E-2	5.01E-2	702	7.05E-2	1.95E-1	23.730	0.475	0.09
119	0.20	1	2.0	1.0E-3	1.8	1.0	10.0	1.00	–	–	5.33E-1	1.02E-1	186	1.88E-2	5.12E-2	11.701	0.532	0.04
120	0.20	1	2.0	1.0E-3	2.2	1.0	10.0	1.00	–	–	3.76E-1	9.15E-2	276	2.78E-2	7.35E-2	27.856	0.868	0.05
121	0.20	1	2.0	1.0E-3	2.6	1.0	10.0	1.00	–	–	3.57E-1	6.42E-2	358	3.60E-2	1.03E-1	29.053	0.835	0.04
122	0.20	1	2.0	1.0E-3	3.5	1.0	10.0	1.00	–	–	2.53E-1	5.91E-2	533	5.36E-2	1.64E-1	31.009	0.745	0.04
123	0.20	1	2.0	1.0E-3	4.4	1.0	10.0	1.00	–	–	9.48E-2	6.68E-2	712	7.15E-2	2.15E-1	25.115	0.526	0.10
124	0.20	1	2.0	1.0E-3	6.6	1.0	10.0	1.00	–	–	3.76E-2	4.09E-2	1002	1.01E-1	2.92E-1	36.594	0.635	0.13
125	0.20	1	2.0	1.0E-3	2.2	1.0	5.0	1.00	–	–	6.12E-1	6.31E-2	139	2.80E-2	8.14E-2	7.424	0.443	0.03
126	0.20	1	2.0	1.0E-3	3.1	1.0	5.0	1.00	–	–	1.54E-2	2.05E-2	217	5.23E-2	1.29E-1	2.586	0.091	0.33
127	0.20	1	2.5	1.0E-3	1.7	1.0	10.0	1.00	–	–	6.32E-1	6.09E-2	174	2.20E-2	7.50E-2	6.927	0.346	0.01
128	0.20	1	2.5	1.0E-3	1.8	1.0	10.0	1.00	–	–	4.96E-1	5.65E-2	206	2.58E-2	8.37E-2	13.968	0.588	0.02
129	0.20	1	2.5	1.0E-3	2.2	1.0	10.0	1.00	–	–	4.00E-1	6.66E-2	271	3.41E-2	1.11E-1	21.024	0.724	0.02
130	0.20	1	2.5	1.0E-3	3.0	1.0	10.0	1.00	–	–	3.19E-1	6.64E-2	376	4.78E-2	1.59E-1	34.621	0.947	0.03
131	0.20	1	2.5	1.0E-3	3.7	1.0	10.0	1.00	–	–	5.13E-2	4.94E-2	694	6.96E-2	2.20E-1	19.199	0.435	0.15
132	0.20	1	2.5	1.0E-3	4.4	1.0	10.0	1.00	–	–	2.31E-2	2.39E-2	817	8.19E-2	2.62E-1	24.321	0.502	0.15
133	0.20	1	2.5	1.0E-3	2.6	1.0	5.0	1.00	–	–	2.06E-2	3.46E-2	191	4.83E-2	1.27E-1	5.355	0.067	0.36

Continued on next page

Model	η	BC	N_ρ	E	Ra/Ra_{cr}	Pr	Pm_i	χ_m	σ_m	a	f_{dip}	SD_{dip}	Rm^*	Ro	Ro_ℓ	Λ	Λ_ℓ	Z
134	0.20	1	2.5	1.0E-3	3.0	1.0	5.0	1.00	–	–	1.56E-2	2.03E-2	228	5.75E-2	1.57E-1	3.189	0.114	0.32
135	0.20	1	3.0	1.0E-3	2.2	1.0	10.0	1.00	–	–	5.71E-1	5.31E-2	298	2.99E-2	1.13E-1	11.037	0.466	0.01
136	0.20	1	3.0	1.0E-3	2.2	1.0	10.0	1.00	–	–	1.42E-2	1.58E-2	217	2.94E-2	9.46E-2	2.128	0.084	0.24
137	0.20	1	3.0	1.0E-3	2.6	1.0	10.0	1.00	–	–	4.76E-1	5.33E-2	374	3.76E-2	1.41E-1	17.318	0.628	0.02
138	0.20	1	3.0	1.0E-3	2.9	1.0	10.0	1.00	–	–	3.00E-2	3.29E-2	478	4.79E-2	1.64E-1	8.675	0.257	0.18
139	0.20	1	3.0	1.0E-3	2.7	1.0	5.0	1.00	–	–	1.90E-3	3.62E-3	225	4.51E-2	1.20E-1	0.180	0.008	0.44
140	0.20	1	3.0	1.0E-3	2.7	1.0	5.0	1.00	–	–	1.35E-3	1.58E-3	229	4.60E-2	1.25E-1	0.444	0.019	0.42
141	0.20	1	3.0	1.0E-3	2.9	1.0	5.0	1.00	–	–	1.81E-3	2.36E-3	254	5.11E-2	1.40E-1	0.904	0.037	0.40
142	0.20	1	3.5	1.0E-3	2.8	1.0	10.0	1.00	–	–	6.61E-3	8.39E-3	384	3.85E-2	1.40E-1	3.029	0.109	0.25
143	0.20	1	4.0	1.0E-3	3.1	1.0	10.0	1.00	–	–	6.12E-3	9.62E-3	411	4.12E-2	1.75E-1	3.814	0.140	0.22
144	0.20	1	4.0	1.0E-3	3.4	1.0	10.0	1.00	–	–	1.43E-2	1.27E-2	466	4.67E-2	1.98E-1	5.689	0.206	0.19
145	0.20	1	4.0	1.0E-3	6.3	1.0	10.0	1.00	–	–	7.13E-3	1.02E-2	836	8.38E-2	3.54E-1	18.913	0.478	0.15
146	0.20	1	5.0	1.0E-3	5.6	1.0	10.0	1.00	–	–	1.03E-2	1.31E-2	616	6.17E-2	3.41E-1	12.154	0.431	0.08
147	0.20	1	5.0	1.0E-3	8.9	1.0	10.0	1.00	–	–	1.04E-2	1.33E-2	919	9.20E-2	5.00E-1	13.849	0.369	0.11
148	0.20	1	0.5	1.0E-4	5.1	1.0	2.0	1.00	–	–	7.24E-1	9.77E-2	104	5.24E-3	1.90E-2	1.130	0.079	0.06
149	0.20	1	0.5	1.0E-4	7.3	1.0	2.0	1.00	–	–	8.03E-1	4.47E-2	149	7.51E-3	3.35E-2	2.721	0.168	0.05
150	0.20	1	0.5	1.0E-4	7.3	1.0	2.0	1.00	–	–	4.21E-2	4.69E-2	172	9.26E-3	3.81E-2	0.840	0.050	0.18
151	0.20	1	0.5	1.0E-4	10.9	1.0	2.0	1.00	–	–	8.51E-1	3.10E-2	202	1.12E-2	5.64E-2	4.967	0.247	0.05
152	0.20	1	0.5	1.0E-4	10.9	1.0	2.0	1.00	–	–	2.32E-2	2.39E-2	264	1.44E-2	6.26E-2	2.036	0.093	0.17
153	0.20	1	0.5	1.0E-4	13.1	1.0	2.0	1.00	–	–	7.43E-1	5.50E-2	296	1.49E-2	7.56E-2	4.560	0.200	0.04
154	0.20	1	0.5	1.0E-4	13.8	1.0	2.0	1.00	–	–	2.03E-2	2.52E-2	323	1.76E-2	7.74E-2	2.996	0.116	0.18
155	0.20	1	0.5	1.0E-4	14.5	1.0	2.0	1.00	–	–	6.34E-2	5.53E-2	332	1.82E-2	8.27E-2	3.272	0.126	0.15
156	0.20	1	0.5	1.0E-4	21.8	1.0	2.0	1.00	–	–	1.16E-2	1.35E-2	459	2.51E-2	1.08E-1	5.556	0.169	0.22
157	0.20	1	0.5	1.0E-4	7.3	1.0	1.0	1.00	–	–	1.80E-2	3.48E-2	99	9.93E-3	3.04E-2	0.244	0.020	0.43
158	0.20	1	0.5	1.0E-4	7.3	1.0	1.0	1.00	–	–	8.97E-1	2.98E-2	79	7.93E-3	3.84E-2	1.107	0.110	0.05
159	0.20	1	0.5	1.0E-4	7.3	1.0	1.5	1.00	–	–	8.39E-1	4.77E-2	114	7.66E-3	3.54E-2	1.891	0.143	0.05
160	0.20	1	0.5	1.0E-4	7.3	1.0	1.5	1.00	–	–	3.72E-2	4.71E-2	140	9.40E-3	3.56E-2	0.534	0.037	0.26
161	0.20	1	1.0	1.0E-4	3.1	1.0	2.0	1.00	–	–	9.20E-1	3.20E-2	68	3.46E-3	1.52E-2	0.353	0.041	0.03

Continued on next page

Model	η	BC	N_ρ	E	Ra/Ra_{cr}	Pr	Pm_i	χ_m	σ_m	a	f_{dip}	SD_{dip}	Rm^*	Ro	Ro_ℓ	Λ	Λ_ℓ	Z
162	0.20	1	1.0	1.0E-4	4.1	1.0	2.0	1.00	–	–	7.88E-1	6.17E-2	113	5.68E-3	2.79E-2	2.142	0.175	0.05
163	0.20	1	1.0	1.0E-4	5.2	1.0	2.0	1.00	–	–	8.08E-1	2.52E-2	132	7.52E-3	3.99E-2	3.593	0.255	0.04
164	0.20	1	1.0	1.0E-4	5.2	1.0	2.0	1.00	–	–	8.24E-1	3.38E-2	152	7.67E-3	4.16E-2	3.103	0.220	0.05
165	0.20	1	1.0	1.0E-4	7.8	1.0	2.0	1.00	–	–	7.64E-1	3.18E-2	223	1.27E-2	7.32E-2	5.511	0.283	0.05
166	0.20	1	1.0	1.0E-4	7.8	1.0	2.0	1.00	–	–	1.03E-1	9.43E-2	299	1.50E-2	7.60E-2	2.613	0.120	0.14
167	0.20	1	1.0	1.0E-4	10.3	1.0	2.0	1.00	–	–	3.18E-2	3.19E-2	396	1.98E-2	9.74E-2	3.755	0.140	0.17
168	0.20	1	1.4	1.0E-4	4.9	1.0	2.0	1.00	–	–	7.60E-1	5.86E-2	214	1.07E-2	6.63E-2	3.425	0.216	0.03
169	0.20	1	1.4	1.0E-4	6.1	1.0	2.0	1.00	–	–	7.04E-2	7.39E-2	304	1.52E-2	8.48E-2	2.792	0.130	0.12
170	0.20	1	1.5	1.0E-4	2.7	1.0	2.0	1.00	–	–	8.42E-1	6.01E-2	86	4.33E-3	2.60E-2	0.791	0.097	0.04
171	0.20	1	1.5	1.0E-4	3.1	1.0	2.0	1.00	–	–	8.66E-1	3.12E-2	94	5.50E-3	3.52E-2	1.197	0.129	0.04
172	0.20	1	1.5	1.0E-4	3.1	1.0	2.0	1.00	–	–	8.40E-1	4.05E-2	95	5.59E-3	3.56E-2	1.245	0.130	0.04
173	0.20	1	1.5	1.0E-4	3.8	1.0	2.0	1.00	–	–	7.97E-1	2.54E-2	138	8.17E-3	5.17E-2	2.400	0.187	0.04
174	0.20	1	1.5	1.0E-4	3.8	1.0	2.0	1.00	–	–	1.49E-1	8.67E-2	158	9.19E-3	5.20E-2	1.103	0.073	0.12
175	0.20	1	1.5	1.0E-4	5.0	1.0	2.0	1.00	–	–	3.61E-2	3.32E-2	220	1.28E-2	7.08E-2	1.865	0.098	0.15
176	0.20	1	1.5	1.0E-4	5.3	1.0	2.0	1.00	–	–	1.00E-1	8.27E-2	236	1.38E-2	7.72E-2	2.145	0.110	0.14
177	0.20	1	1.5	1.0E-4	5.7	1.0	2.0	1.00	–	–	9.31E-2	8.15E-2	257	1.50E-2	8.27E-2	2.305	0.110	0.16
178	0.20	1	1.5	1.0E-4	7.6	1.0	2.0	1.00	–	–	5.00E-2	3.96E-2	354	2.07E-2	1.19E-1	4.632	0.177	0.14
179	0.20	1	1.7	1.0E-4	3.1	1.0	2.0	1.00	–	–	8.09E-1	3.00E-2	137	6.91E-3	4.67E-2	1.628	0.155	0.04
180	0.20	1	1.7	1.0E-4	3.1	1.0	2.0	1.00	–	–	4.84E-2	4.75E-2	149	7.52E-3	4.48E-2	0.757	0.057	0.11
181	0.20	1	1.7	1.0E-4	4.1	1.0	2.0	1.00	–	–	4.32E-2	3.51E-2	226	1.13E-2	6.45E-2	1.333	0.080	0.17
182	0.20	1	1.8	1.0E-4	2.9	1.0	2.0	1.00	–	–	8.04E-1	4.06E-2	135	6.80E-3	4.64E-2	1.480	0.144	0.05
183	0.20	1	1.8	1.0E-4	2.9	1.0	2.0	1.00	–	–	4.60E-2	3.55E-2	145	7.32E-3	4.30E-2	0.677	0.053	0.14
184	0.20	1	2.0	1.0E-4	2.2	1.0	2.0	1.00	–	–	2.24E-2	1.60E-2	88	4.42E-3	2.35E-2	0.190	0.021	0.23
185	0.20	1	2.0	1.0E-4	2.2	1.0	6.0	1.00	–	–	6.52E-1	3.68E-2	247	4.12E-3	3.16E-2	1.745	0.113	0.02
186	0.20	1	2.0	1.0E-4	2.5	1.0	2.0	1.00	–	–	1.53E-2	1.61E-2	128	6.46E-3	3.78E-2	0.494	0.043	0.18
187	0.20	1	2.0	1.0E-4	2.5	1.0	6.0	1.00	–	–	3.70E-1	9.49E-2	429	7.17E-3	5.12E-2	7.833	0.317	0.02
188	0.20	1	2.0	1.0E-4	2.9	1.0	2.0	1.00	–	–	2.91E-2	4.55E-2	165	8.28E-3	4.94E-2	0.762	0.057	0.18
189	0.20	1	2.0	1.0E-4	Inf	4.0	4.0	1.00	–	–	8.52E-1	1.23E-2	77	1.94E-3	1.67E-2	0.534	0.034	0.02

Continued on next page

Model	η	BC	N_ρ	E	Ra/Ra_{cr}	Pr	Pm_i	χ_m	σ_m	a	f_{dip}	SD_{dip}	Rm^*	Ro	Ro_ℓ	Λ	Λ_ℓ	Z
190	0.20	1	2.0	1.0E-4	Inf	4.0	4.0	1.00	–	–	1.48E-5	3.54E-5	69	1.73E-3	1.30E-2	0.057	0.004	0.14
191	0.20	1	2.0	1.0E-4	2.9	1.0	6.0	1.00	–	–	4.74E-1	7.30E-2	515	8.62E-3	6.32E-2	8.669	0.335	0.02
192	0.20	1	2.0	1.0E-4	Inf	3.0	6.0	1.00	–	–	7.75E-1	3.38E-2	152	2.54E-3	2.15E-2	1.600	0.058	0.02
193	0.20	1	2.0	1.0E-4	Inf	3.0	6.0	1.00	–	–	5.61E-2	4.57E-2	150	2.51E-3	2.05E-2	0.685	0.022	0.03
194	0.20	1	2.0	1.0E-4	Inf	4.0	8.0	1.00	–	–	7.09E-2	6.35E-2	147	1.84E-3	1.54E-2	0.468	0.015	0.03
195	0.20	1	2.0	1.0E-4	4.3	1.0	2.0	1.00	–	–	6.57E-2	5.98E-2	300	1.50E-2	9.11E-2	2.450	0.123	0.17
196	0.20	1	2.0	1.0E-4	5.8	1.0	2.0	1.00	–	–	5.40E-2	4.44E-2	417	2.09E-2	1.31E-1	4.442	0.178	0.16
197	0.20	1	2.0	1.0E-4	2.9	1.0	1.0	1.00	–	–	1.17E-2	1.15E-2	87	8.80E-3	3.85E-2	0.234	0.027	0.42
198	0.20	1	2.5	1.0E-4	2.2	1.0	2.0	1.00	–	–	5.06E-3	5.32E-3	115	7.43E-3	4.43E-2	0.584	0.046	0.26
199	0.20	1	2.5	1.0E-4	3.3	1.0	2.0	1.00	–	–	5.04E-2	5.09E-2	222	1.42E-2	9.44E-2	1.957	0.112	0.20
200	0.20	1	3.0	1.0E-4	2.3	1.0	2.0	1.00	–	–	4.33E-3	4.49E-3	144	7.21E-3	3.99E-2	0.384	0.032	0.41
201	0.20	1	3.0	1.0E-4	2.4	1.0	2.0	1.00	–	–	3.27E-3	3.12E-3	112	7.82E-3	4.56E-2	0.506	0.041	0.37
202	0.20	1	3.0	1.0E-4	2.6	1.0	2.0	1.00	–	–	5.30E-3	5.96E-3	181	9.09E-3	5.90E-2	0.817	0.063	0.28
203	0.20	1	3.0	1.0E-4	2.8	1.0	2.0	1.00	–	–	9.84E-3	1.02E-2	202	1.01E-2	6.53E-2	1.033	0.070	0.29
204	0.20	1	3.0	1.0E-4	3.2	1.0	2.0	1.00	–	–	2.16E-2	3.12E-2	182	1.24E-2	9.42E-2	1.575	0.104	0.17
205	0.20	1	3.0	1.0E-4	4.3	1.0	2.0	1.00	–	–	4.53E-2	5.59E-2	373	1.87E-2	1.52E-1	3.380	0.184	0.11
206	0.20	1	3.0	1.0E-4	8.6	1.0	2.0	1.00	–	–	2.74E-2	3.03E-2	701	3.51E-2	2.56E-1	8.970	0.301	0.21
207	0.20	1	3.0	1.0E-4	2.8	1.0	10.0	1.00	–	–	7.00E-2	3.87E-2	1011	1.01E-2	8.84E-2	8.925	0.258	0.07
208	0.20	1	3.0	1.0E-4	2.1	0.1	1.0	1.00	–	–	6.42E-1	3.50E-2	294	2.95E-2	1.54E-1	12.515	0.581	0.09
209	0.20	1	5.0	1.0E-4	5.6	1.0	2.0	1.00	–	–	9.67E-4	5.18E-4	313	1.57E-2	1.41E-1	1.237	0.114	0.41
210	0.20	1	5.0	1.0E-4	6.1	1.0	2.0	1.00	–	–	4.52E-3	4.27E-3	334	1.68E-2	1.66E-1	1.751	0.139	0.33
211	0.20	1	5.0	1.0E-4	7.4	1.0	2.0	1.00	–	–	3.36E-2	1.46E-2	368	1.84E-2	2.23E-1	3.142	0.230	0.15
212	0.20	1	5.0	1.0E-4	9.3	1.0	2.0	1.00	–	–	2.31E-2	2.58E-3	438	2.19E-2	2.73E-1	4.044	0.253	0.09
213	0.20	1	4.0	3.0E-5	5.1	1.0	2.0	1.00	–	–	9.79E-4	1.56E-3	499	7.49E-3	1.19E-1	2.284	0.144	0.06
214	0.20	1	1.0	1.0E-5	3.3	1.0	1.0	1.00	–	–	9.60E-1	3.26E-3	58	5.89E-4	5.18E-3	0.058	0.011	0.05
215	0.20	1	1.0	1.0E-5	5.0	1.0	1.0	1.00	–	–	5.76E-1	3.53E-2	133	1.34E-3	1.68E-2	0.371	0.037	0.03
216	0.20	1	1.0	1.0E-5	10.0	1.0	1.0	1.00	–	–	6.99E-1	5.60E-2	356	3.57E-3	4.32E-2	2.091	0.119	0.02
217	0.20	1	1.0	1.0E-5	19.9	1.0	1.0	1.00	–	–	4.67E-2	3.98E-2	707	7.08E-3	8.13E-2	3.791	0.143	0.03

Continued on next page

Model	η	BC	N_ρ	E	Ra/Ra_{cr}	Pr	Pm_i	χ_m	σ_m	a	f_{dip}	SD_{dip}	Rm^*	Ro	Ro_ℓ	Λ	Λ_ℓ	Z
218	0.20	1	1.5	1.0E-5	3.6	1.0	1.0	1.00	–	–	6.68E-1	2.59E-2	134	1.35E-3	1.64E-2	0.568	0.057	0.04
219	0.20	1	1.5	1.0E-5	7.3	1.0	1.0	1.00	–	–	5.97E-1	1.93E-2	369	3.70E-3	4.46E-2	1.694	0.095	0.02
220	0.20	1	2.0	1.0E-5	2.5	1.0	1.0	1.00	–	–	8.33E-1	6.35E-3	87	8.76E-4	1.29E-2	0.134	0.032	0.15
221	0.20	1	2.0	1.0E-5	2.9	1.0	1.0	1.00	–	–	5.88E-1	2.33E-2	153	1.54E-3	2.35E-2	0.312	0.035	0.06
222	0.20	1	2.0	1.0E-5	3.6	1.0	1.0	1.00	–	–	3.72E-1	1.05E-1	213	2.27E-3	3.53E-2	0.597	0.052	0.03
223	0.20	1	2.0	1.0E-5	2.9	1.0	2.0	1.00	–	–	1.57E-1	3.08E-2	251	1.52E-3	2.59E-2	0.591	0.040	0.01
224	0.20	1	2.5	1.0E-5	2.0	1.0	1.0	1.00	–	–	4.37E-3	5.46E-3	117	1.17E-3	6.56E-3	0.010	0.002	0.72
225	0.20	1	2.5	1.0E-5	2.4	1.0	1.0	1.00	–	–	1.38E-2	1.66E-2	200	2.03E-3	2.46E-2	0.240	0.022	0.07
226	0.20	1	3.0	1.0E-5	2.3	1.0	1.0	1.00	–	–	5.27E-3	5.13E-3	394	3.97E-3	1.61E-2	0.160	0.007	0.03
227	0.20	1	3.0	1.0E-5	2.8	1.0	1.0	1.00	–	–	4.99E-2	2.56E-2	265	2.66E-3	4.85E-2	0.415	0.034	0.05
228	0.20	2	0.0	1.0E-3	5.3	1.0	10.0	1.00	–	–	1.67E-1	2.80E-2	253	2.54E-2	3.07E-2	7.014	0.162	0.06
229	0.20	2	3.0	1.0E-3	2.2	1.0	10.0	1.00	–	–	2.91E-1	6.22E-2	256	2.57E-2	7.15E-2	29.893	0.938	0.03
230	0.20	2	4.0	1.0E-3	3.1	1.0	10.0	1.00	–	–	4.11E-1	3.72E-2	309	3.09E-2	1.23E-1	18.906	0.714	0.01
231	0.20	2	0.0	1.0E-4	23.0	1.0	2.0	1.00	–	–	6.60E-1	3.72E-2	250	1.26E-2	5.04E-2	6.155	0.241	0.03
232	0.20	2	2.0	1.0E-4	2.2	1.0	2.0	1.00	–	–	6.94E-1	2.56E-2	111	5.58E-3	4.07E-2	0.767	0.100	0.01
233	0.20	2	2.0	1.0E-4	2.2	1.0	2.0	1.00	–	–	6.94E-1	2.56E-2	111	5.58E-3	4.07E-2	0.767	0.100	0.01
234	0.20	2	2.0	1.0E-4	2.9	1.0	2.0	1.00	–	–	6.32E-1	5.99E-2	166	8.37E-3	5.59E-2	2.547	0.210	0.03
235	0.20	2	3.0	1.0E-4	2.3	1.0	2.0	1.00	–	–	1.83E-2	3.95E-2	147	7.39E-3	3.44E-2	0.263	0.023	0.52
236	0.20	2	3.0	1.0E-4	2.4	1.0	2.0	1.00	–	–	4.20E-2	5.54E-2	166	8.32E-3	6.93E-2	0.703	0.066	0.03
237	0.20	2	3.0	1.0E-4	2.8	1.0	2.0	1.00	–	–	8.23E-2	1.01E-1	217	1.09E-2	8.90E-2	1.729	0.122	0.02
238	0.20	2	5.0	1.0E-4	7.4	1.0	2.0	1.00	–	–	3.87E-3	3.34E-3	303	1.52E-2	1.77E-1	2.147	0.138	0.08
239	0.20	2	5.0	1.0E-4	9.3	1.0	2.0	1.00	–	–	3.33E-2	5.29E-3	368	1.84E-2	2.15E-1	3.146	0.193	0.05
240	0.20	2	2.5	1.0E-5	2.0	1.0	1.0	1.00	–	–	2.63E-3	2.41E-3	127	1.28E-3	2.39E-2	0.058	0.006	0.03
241	0.20	1	0.0	3.0E-4	8.9	1.0	8.0	0.95	0.50	9	6.95E-1	6.85E-2	334	1.54E-2	3.75E-2	7.937	0.188	0.06
242	0.20	1	0.0	3.0E-4	10.7	1.0	8.0	0.95	0.50	9	1.28E-1	7.36E-2	437	2.00E-2	4.84E-2	4.117	0.097	0.27
243	0.20	1	0.0	1.0E-4	11.5	1.0	2.0	0.80	0.50	9	5.30E-2	5.81E-2	139	1.12E-2	2.02E-2	0.255	0.009	0.65
244	0.20	1	0.0	1.0E-4	11.5	1.0	10.0	0.80	0.50	9	8.03E-1	5.06E-2	402	8.07E-3	2.85E-2	6.480	0.108	0.09
245	0.20	1	0.0	1.0E-4	17.2	1.0	2.0	0.80	0.50	9	8.66E-2	1.09E-1	205	1.74E-2	3.51E-2	0.727	0.020	0.64

Continued on next page

Model	η	BC	N_ρ	E	Ra/Ra_{cr}	Pr	Pm_i	χ_m	σ_m	a	f_{dip}	SD_{dip}	Rm^*	Ro	Ro_ℓ	Λ	Λ_ℓ	Z
246	0.20	1	0.0	1.0E-4	23.0	1.0	2.0	0.80	0.50	9	4.78E-2	5.62E-2	275	2.40E-2	5.00E-2	1.178	0.027	0.62
247	0.20	1	0.0	1.0E-4	45.9	1.0	2.0	0.80	0.50	9	1.11E-1	3.64E-2	453	3.96E-2	8.87E-2	2.401	0.041	0.62
248	0.20	1	0.0	1.0E-4	10.3	1.0	2.0	0.90	0.50	9	3.88E-2	5.14E-2	130	8.98E-3	1.83E-2	0.262	0.012	0.57
249	0.20	1	0.0	1.0E-4	11.5	1.0	2.0	0.90	0.50	9	4.79E-2	5.07E-2	153	9.89E-3	2.31E-2	0.432	0.020	0.50
250	0.20	1	0.0	1.0E-4	23.0	1.0	2.0	0.90	0.50	9	7.06E-2	7.62E-2	269	1.84E-2	5.68E-2	1.857	0.061	0.38
251	0.20	1	0.0	1.0E-4	9.2	1.0	5.0	0.90	0.50	9	6.21E-1	1.81E-1	241	6.53E-3	1.84E-2	3.892	0.104	0.07
252	0.20	1	0.0	1.0E-4	11.5	1.0	2.0	0.95	0.50	9	8.45E-1	4.33E-2	130	7.97E-3	2.78E-2	1.709	0.087	0.04
253	0.20	1	0.0	1.0E-4	11.5	1.0	2.0	0.95	0.50	9	1.12E-1	8.10E-2	157	9.38E-3	2.62E-2	0.575	0.029	0.36
254	0.20	1	0.0	1.0E-4	17.2	1.0	2.0	0.95	0.50	9	6.49E-2	6.72E-2	235	1.44E-2	4.35E-2	1.236	0.051	0.37
255	0.20	1	0.0	1.0E-4	23.0	1.0	2.0	0.95	0.50	9	2.81E-2	2.98E-2	290	1.80E-2	5.67E-2	1.936	0.067	0.35
256	0.20	1	0.0	3.0E-5	21.4	1.0	1.0	0.80	0.50	9	1.05E-1	9.11E-2	127	6.25E-3	1.52E-2	0.193	0.009	0.64
257	0.20	1	0.0	3.0E-5	34.2	1.0	1.0	0.80	0.50	9	8.75E-2	8.82E-2	197	1.07E-2	2.68E-2	0.510	0.017	0.67
258	0.20	1	0.0	3.0E-5	51.3	1.0	1.0	0.80	0.50	9	1.67E-1	1.34E-1	262	1.46E-2	3.96E-2	0.977	0.026	0.66
259	0.20	1	0.0	3.0E-5	21.4	1.0	2.0	0.80	0.50	9	8.87E-1	2.04E-2	148	4.00E-3	2.08E-2	1.579	0.059	0.10
260	0.20	1	0.0	1.0E-5	7.2	1.0	1.0	0.80	0.50	9	8.71E-1	2.45E-2	90	1.46E-3	8.95E-3	0.324	0.020	0.11
261	0.20	1	0.0	1.0E-5	12.1	1.0	1.0	0.80	0.50	9	8.52E-1	2.69E-2	138	2.59E-3	1.94E-2	0.969	0.040	0.17
262	0.20	1	0.0	1.0E-5	7.2	1.0	3.0	0.80	0.50	9	8.38E-1	2.84E-2	246	1.33E-3	7.78E-3	1.664	0.049	0.11
263	0.20	1	0.0	1.0E-5	12.1	1.0	3.0	0.80	0.50	9	8.36E-1	2.06E-2	357	2.40E-3	1.98E-2	4.814	0.114	0.07
264	0.20	1	0.0	1.0E-5	7.2	0.1	1.0	0.80	0.50	9	9.14E-1	3.21E-2	240	4.05E-3	9.76E-3	1.620	0.025	0.39
265	0.20	1	0.0	1.0E-5	14.4	0.1	1.0	0.80	0.50	9	3.86E-1	1.92E-1	577	9.41E-3	1.81E-2	2.014	0.028	0.70
266	0.20	1	0.0	1.0E-5	5.8	1.0	1.0	0.95	0.50	9	8.61E-1	1.64E-2	98	1.16E-3	6.87E-3	0.214	0.016	0.06
267	0.20	1	2.0	1.0E-3	2.6	1.0	10.0	0.95	0.50	9	4.22E-1	8.43E-2	278	3.84E-2	1.12E-1	17.228	0.560	0.05
268	0.20	1	2.0	1.0E-3	2.6	1.0	10.0	0.95	0.50	9	3.81E-2	4.68E-2	293	4.08E-2	1.10E-1	3.871	0.135	0.23
269	0.20	1	2.0	1.0E-3	3.1	1.0	10.0	0.95	0.50	9	1.84E-2	2.52E-2	362	5.06E-2	1.36E-1	5.891	0.181	0.24
270	0.20	1	2.0	1.0E-3	3.5	1.0	10.0	0.95	0.50	9	1.96E-2	2.48E-2	423	5.96E-2	1.62E-1	8.005	0.223	0.24
271	0.20	1	1.0	3.0E-4	3.7	1.0	5.0	0.95	0.50	9	7.91E-1	4.70E-2	136	5.55E-3	3.68E-2	4.608	0.244	0.23
272	0.20	1	1.0	3.0E-4	3.7	1.0	5.0	0.95	0.50	9	1.01E-1	1.16E-1	161	1.24E-2	3.74E-2	0.986	0.048	0.22
273	0.20	1	1.0	3.0E-4	4.6	1.0	5.0	0.95	0.50	9	7.78E-1	3.92E-2	189	1.46E-2	5.39E-2	7.690	0.339	0.04

Continued on next page

Model	η	BC	N_ρ	E	Ra/Ra_{cr}	Pr	Pm_i	χ_m	σ_m	a	f_{dip}	SD_{dip}	Rm^*	Ro	Ro_ℓ	Λ	Λ_ℓ	Z
274	0.20	1	1.0	3.0E-4	4.6	1.0	5.0	0.96	0.60	9	2.69E-2	3.28E-2	234	1.79E-2	5.81E-2	1.955	0.081	0.21
275	0.20	1	1.0	3.0E-4	5.0	1.0	5.0	0.95	0.50	9	7.59E-1	5.13E-2	213	1.66E-2	6.15E-2	8.664	0.353	0.04
276	0.20	1	1.0	3.0E-4	5.0	1.0	5.0	0.95	0.50	9	6.09E-2	5.75E-2	257	1.98E-2	6.50E-2	2.305	0.092	0.20
277	0.20	1	1.0	3.0E-4	5.6	1.0	5.0	0.95	0.50	9	2.73E-2	3.44E-2	292	2.27E-2	7.45E-2	3.142	0.114	0.22
278	0.20	1	1.0	3.0E-4	6.5	1.0	5.0	0.95	0.50	9	3.88E-2	3.94E-2	350	2.74E-2	8.95E-2	4.302	0.136	0.26
279	0.20	1	1.0	3.0E-4	7.4	1.0	5.0	0.95	0.50	9	4.21E-2	5.11E-2	383	3.14E-2	1.08E-1	5.475	0.159	0.23
280	0.20	1	3.0	3.0E-4	2.5	1.0	5.0	0.95	0.50	9	6.45E-3	7.10E-3	153	1.75E-2	7.04E-2	1.082	0.071	0.38
281	0.20	1	3.0	3.0E-4	3.4	1.0	5.0	0.95	0.50	9	5.02E-2	6.05E-2	254	2.77E-2	1.38E-1	3.561	0.183	0.23
282	0.20	1	3.0	3.0E-4	2.1	1.0	8.0	0.95	0.50	9	1.68E-2	1.26E-2	167	1.24E-2	4.43E-2	0.517	0.032	0.47
283	0.20	1	5.0	3.0E-4	5.7	1.0	10.0	0.80	0.50	9	5.58E-1	4.99E-2	166	3.05E-2	2.45E-1	1.836	0.194	0.22
284	0.20	1	5.0	3.0E-4	3.1	1.0	10.0	0.80	0.50	9	1.65E-1	1.15E-1	172	3.20E-2	2.31E-1	0.832	0.082	0.32
285	0.20	1	5.0	3.0E-4	3.1	1.0	10.0	0.80	0.50	25	2.57E-1	1.85E-1	136	3.33E-2	2.18E-1	0.582	0.051	0.40
286	0.20	1	5.0	3.0E-4	3.4	1.0	5.0	0.80	0.50	25	1.77E-1	1.28E-1	90	3.84E-2	2.30E-1	0.288	0.034	0.45
287	0.20	1	5.0	3.0E-4	7.6	1.0	7.0	0.80	0.50	9	7.57E-2	7.99E-2	191	4.40E-2	2.87E-1	1.124	0.094	0.38
288	0.20	1	5.0	3.0E-4	4.4	1.0	10.0	0.80	0.50	9	3.97E-2	4.09E-2	331	4.46E-2	3.40E-1	2.493	0.174	0.24
289	0.20	1	1.0	1.0E-4	5.2	1.0	2.0	0.80	0.50	9	3.53E-2	4.23E-2	94	1.07E-2	2.84E-2	0.252	0.013	0.58
290	0.20	1	1.0	1.0E-4	10.3	1.0	2.0	0.80	0.50	9	8.79E-2	8.43E-2	224	2.73E-2	6.98E-2	1.172	0.033	0.65
291	0.20	1	1.0	1.0E-4	7.8	1.0	1.0	0.80	0.50	9	1.38E-1	1.05E-1	93	2.28E-2	4.02E-2	0.159	0.007	0.77
292	0.20	1	1.0	1.0E-4	5.2	1.0	2.0	0.90	0.50	9	8.74E-1	2.83E-2	103	7.76E-3	4.28E-2	1.881	0.140	0.06
293	0.20	1	1.0	1.0E-4	5.2	1.0	2.0	0.90	0.50	9	8.12E-2	1.08E-1	126	9.34E-3	4.05E-2	0.602	0.039	0.26
294	0.20	1	1.0	1.0E-4	7.8	1.0	2.0	0.90	0.50	9	1.13E-1	1.29E-1	203	1.58E-2	6.71E-2	1.491	0.070	0.30
295	0.20	1	1.0	1.0E-4	4.1	1.0	2.0	0.95	0.50	9	8.29E-1	4.76E-2	89	5.66E-3	2.91E-2	1.227	0.108	0.05
296	0.20	1	1.0	1.0E-4	4.1	1.0	2.0	0.95	0.50	9	9.74E-2	8.93E-2	103	6.48E-3	2.79E-2	0.399	0.031	0.21
297	0.20	1	1.0	1.0E-4	5.2	1.0	2.0	0.95	0.50	9	8.36E-1	3.49E-2	120	7.78E-3	4.35E-2	2.210	0.164	0.04
298	0.20	1	1.0	1.0E-4	5.2	1.0	2.0	0.95	0.50	9	5.24E-2	6.01E-2	145	9.27E-3	4.38E-2	0.754	0.049	0.18
299	0.20	1	1.0	1.0E-4	7.8	1.0	2.0	0.95	0.50	9	3.86E-2	4.81E-2	233	1.53E-2	7.15E-2	1.849	0.089	0.21
300	0.20	1	2.0	1.0E-4	2.9	1.0	2.0	0.95	0.50	9	4.20E-2	3.77E-2	106	8.32E-3	4.41E-2	0.503	0.044	0.28
301	0.20	1	3.0	1.0E-4	4.3	1.0	2.0	0.70	0.50	9	2.03E-1	2.01E-1	90	2.87E-2	7.72E-2	0.224	0.015	0.77

Continued on next page

Model	η	BC	N_ρ	E	Ra/Ra_{cr}	Pr	Pm_i	χ_m	σ_m	a	f_{dip}	SD_{dip}	Rm^*	Ro	Ro_ℓ	Λ	Λ_ℓ	Z
302	0.20	1	3.0	1.0E-4	4.3	1.0	6.0	0.70	0.50	9	3.07E-1	2.19E-1	241	2.67E-2	8.76E-2	1.035	0.041	0.71
303	0.20	1	3.0	1.0E-4	3.2	1.0	2.0	0.80	0.50	9	1.19E-1	1.03E-1	75	1.63E-2	4.97E-2	0.197	0.020	0.72
304	0.20	1	3.0	1.0E-4	4.3	1.0	1.0	0.80	0.50	9	3.23E-1	2.87E-1	79	2.80E-2	8.75E-2	0.165	0.018	0.73
305	0.20	1	3.0	1.0E-4	4.3	1.0	2.0	0.80	0.50	9	2.80E-1	1.80E-1	134	2.53E-2	9.35E-2	0.529	0.040	0.67
306	0.20	1	3.0	1.0E-4	3.2	1.0	6.0	0.80	0.50	9	2.33E-1	1.98E-1	214	1.45E-2	6.98E-2	1.420	0.085	0.52
307	0.20	1	3.0	1.0E-4	4.3	1.0	6.0	0.80	0.50	9	2.27E-2	2.52E-2	341	2.18E-2	1.25E-1	2.446	0.119	0.45
308	0.20	1	3.0	1.0E-4	8.6	1.0	2.0	0.80	0.50	9	5.25E-2	3.55E-2	257	4.66E-2	2.18E-1	2.164	0.105	0.55
309	0.20	1	3.0	1.0E-4	4.3	1.0	2.0	0.80	0.50	25	2.34E-1	1.37E-1	127	2.60E-2	8.47E-2	0.453	0.030	0.71
310	0.20	1	3.0	1.0E-4	3.2	1.0	2.0	0.90	0.50	9	5.64E-2	6.69E-2	123	1.36E-2	7.33E-2	0.563	0.056	0.45
311	0.20	1	3.0	1.0E-4	3.2	1.0	2.0	0.95	0.50	9	2.10E-2	2.04E-2	157	1.31E-2	8.62E-2	0.933	0.081	0.29
312	0.20	1	4.0	1.0E-4	6.6	1.0	2.0	0.70	0.50	9	3.02E-1	2.54E-1	92	3.68E-2	1.18E-1	0.172	0.014	0.78
313	0.20	1	4.0	1.0E-4	8.8	1.0	2.0	0.70	0.50	9	4.16E-1	2.40E-1	128	4.92E-2	1.49E-1	0.331	0.021	0.79
314	0.20	1	4.0	1.0E-4	6.6	1.0	4.0	0.70	0.50	9	9.32E-1	1.09E-2	118	2.91E-2	1.47E-1	1.717	0.144	0.61
315	0.20	1	4.0	1.0E-4	6.6	1.0	4.0	0.70	0.50	9	3.60E-1	2.45E-1	160	3.42E-2	1.28E-1	0.485	0.030	0.73
316	0.20	1	4.0	1.0E-4	4.4	1.0	2.0	0.80	0.50	9	1.07E-2	2.08E-2	69	1.80E-2	7.50E-2	0.072	0.014	0.71
317	0.20	1	4.0	1.0E-4	5.5	1.0	2.0	0.80	0.50	9	4.40E-1	2.76E-1	101	2.48E-2	1.16E-1	0.297	0.039	0.66
318	0.20	1	4.0	1.0E-4	5.5	1.0	4.0	0.80	0.50	9	8.06E-1	1.77E-2	155	2.04E-2	1.45E-1	1.672	0.180	0.43
319	0.20	1	4.0	1.0E-4	8.8	1.0	2.0	0.80	0.50	9	2.43E-1	2.26E-1	183	3.90E-2	1.96E-1	0.912	0.071	0.61
320	0.20	1	4.0	1.0E-4	5.5	1.0	2.0	0.95	0.50	9	4.07E-3	4.21E-3	168	1.83E-2	1.59E-1	1.185	0.093	0.27
321	0.20	1	5.0	1.0E-4	11.2	1.0	2.0	0.70	0.50	9	4.07E-1	3.06E-1	94	4.56E-2	2.14E-1	0.250	0.023	0.72
322	0.20	1	5.0	1.0E-4	7.4	1.0	2.0	0.80	0.50	9	9.02E-1	1.40E-2	69	2.22E-2	2.11E-1	0.643	0.172	0.38
323	0.20	1	5.0	1.0E-4	9.3	1.0	2.0	0.80	0.50	9	9.03E-1	8.03E-3	94	2.77E-2	2.63E-1	1.074	0.211	0.37
324	0.20	1	5.0	1.0E-4	9.3	1.0	2.0	0.80	0.50	9	5.43E-1	2.25E-1	110	3.18E-2	2.22E-1	0.470	0.070	0.56
325	0.20	1	5.0	1.0E-4	11.2	1.0	2.0	0.80	0.50	9	4.84E-1	2.74E-1	127	3.55E-2	2.79E-1	0.732	0.096	0.49
326	0.20	1	5.0	1.0E-4	7.4	1.0	2.0	0.80	0.50	25	9.43E-1	8.77E-3	58	2.59E-2	1.66E-1	0.319	0.072	0.60
327	0.20	1	5.0	1.0E-4	7.4	1.0	2.0	0.80	0.50	25	4.73E-1	2.35E-1	100	3.05E-2	1.45E-1	0.024	0.003	0.72
328	0.20	1	5.0	1.0E-4	7.4	1.0	2.0	0.90	0.50	9	1.18E-3	1.83E-3	140	2.10E-2	2.18E-1	0.735	0.097	0.31
329	0.20	1	5.0	1.0E-4	9.3	1.0	2.0	0.90	0.50	9	4.85E-3	2.27E-3	180	2.49E-2	2.60E-1	1.069	0.119	0.28

Continued on next page

Model	η	BC	N_ρ	E	Ra/Ra_{cr}	Pr	Pm_i	χ_m	σ_m	a	f_{dip}	SD_{dip}	Rm^*	Ro	Ro_ℓ	Λ	Λ_ℓ	Z
330	0.20	1	5.0	1.0E-4	9.3	1.0	2.5	0.90	0.03	1	9.63E-1	8.32E-3	49	3.15E-2	2.13E-1	0.468	0.105	0.57
331	0.20	1	5.5	1.0E-4	9.7	1.0	2.0	0.80	0.50	9	9.11E-1	9.77E-3	77	2.54E-2	3.01E-1	0.763	0.203	0.30
332	0.20	1	6.0	1.0E-4	34.1	1.0	2.0	0.70	0.50	9	3.94E-1	2.70E-1	172	7.02E-2	6.48E-1	0.927	0.060	0.53
333	0.20	1	1.0	3.0E-5	6.2	1.0	1.0	0.80	0.50	9	9.54E-1	1.06E-2	69	4.95E-3	2.68E-2	0.620	0.051	0.41
334	0.20	1	1.0	3.0E-5	7.5	1.0	1.0	0.80	0.50	9	9.51E-1	8.72E-3	88	6.66E-3	3.34E-2	0.848	0.057	0.48
335	0.20	1	1.0	3.0E-5	10.0	1.0	1.0	0.80	0.50	9	1.27E-1	9.78E-2	168	1.17E-2	3.98E-2	0.448	0.021	0.65
336	0.20	1	3.0	3.0E-5	2.8	1.0	1.0	0.80	0.50	9	1.68E-2	1.56E-2	62	1.20E-2	1.80E-2	0.038	0.006	0.78
337	0.20	1	2.0	3.0E-5	4.1	1.0	1.0	0.80	0.50	9	2.05E-1	1.36E-1	88	8.13E-3	2.98E-2	0.179	0.016	0.70
338	0.20	1	2.0	3.0E-5	6.8	1.0	1.0	0.80	0.50	9	2.37E-1	1.73E-1	172	1.55E-2	6.64E-2	0.464	0.029	0.66
339	0.20	1	3.0	3.0E-5	2.8	1.0	1.0	0.80	0.50	9	1.68E-2	1.56E-2	62	7.56E-3	1.80E-2	0.038	0.006	0.85
340	0.20	1	3.0	3.0E-5	3.7	1.0	1.0	0.80	0.50	9	1.59E-2	1.57E-2	85	1.12E-2	4.09E-2	0.116	0.014	0.78
341	0.20	1	3.0	3.0E-5	2.8	1.0	2.0	0.80	0.50	9	1.90E-2	2.14E-2	101	6.61E-3	2.17E-2	0.115	0.012	0.79
342	0.20	1	4.0	3.0E-5	4.6	1.0	2.0	0.80	0.50	9	8.91E-1	1.27E-2	95	9.69E-3	4.65E-2	0.365	0.066	0.78
343	0.20	1	4.0	3.0E-5	4.6	1.0	2.0	0.80	0.50	9	2.94E-2	2.75E-2	94	9.16E-3	3.80E-2	0.070	0.012	0.80
344	0.20	1	4.0	3.0E-5	5.6	1.0	2.0	0.80	0.50	9	8.71E-1	8.02E-3	119	9.85E-3	1.10E-1	1.039	0.159	0.41
345	0.20	1	1.0	1.0E-5	6.6	1.0	1.0	0.80	0.50	9	9.25E-1	8.83E-3	101	2.46E-3	1.93E-2	0.538	0.039	0.40
346	0.20	1	1.0	1.0E-5	10.0	1.0	1.0	0.80	0.50	9	9.04E-1	6.00E-3	145	4.14E-3	3.25E-2	1.406	0.071	0.41
347	0.20	1	1.0	1.0E-5	16.6	1.0	1.0	0.80	0.50	9	2.30E-1	2.00E-1	329	8.93E-3	4.78E-2	0.821	0.030	0.60
348	0.20	1	2.0	1.0E-5	3.6	1.0	1.0	0.80	0.50	9	8.64E-1	1.34E-2	84	2.61E-3	1.98E-2	0.234	0.025	0.54
349	0.20	1	2.0	1.0E-5	5.4	1.0	1.0	0.80	0.50	9	9.04E-1	2.68E-2	151	5.75E-3	2.78E-2	0.531	0.039	0.73
350	0.20	1	3.0	1.0E-5	2.3	1.0	1.0	0.80	0.50	9	2.06E-2	1.47E-2	70	3.20E-3	7.44E-3	0.006	0.001	0.91
351	0.20	1	3.0	1.0E-5	3.4	1.0	1.0	0.80	0.50	9	9.35E-1	9.74E-3	102	5.51E-3	2.52E-2	0.276	0.039	0.81
352	0.20	1	3.0	1.0E-5	4.5	1.0	1.0	0.80	0.50	9	8.86E-1	2.66E-2	141	6.72E-3	5.84E-2	0.675	0.076	0.61
353	0.20	1	3.0	1.0E-5	4.5	1.0	0.5	0.80	0.50	9	9.56E-1	7.27E-3	89	8.90E-3	4.64E-2	0.157	0.028	0.77
354	0.20	2	0.0	1.0E-4	11.5	1.0	10.0	0.80	0.50	9	7.60E-1	5.92E-2	395	7.84E-3	2.86E-2	6.728	0.119	0.03
355	0.20	2	0.0	1.0E-4	20.7	1.0	2.0	0.80	0.50	9	6.26E-2	9.18E-2	161	1.57E-2	6.36E-2	0.195	0.008	0.11
356	0.20	2	0.0	1.0E-4	23.0	1.0	2.0	0.80	0.50	9	3.40E-2	4.50E-2	177	1.71E-2	6.93E-2	0.232	0.009	0.09
357	0.20	2	0.0	1.0E-4	11.5	1.0	2.0	0.90	0.50	9	8.64E-1	2.48E-2	113	7.81E-3	2.79E-2	1.618	0.082	0.04

Continued on next page

Model	η	BC	N_ρ	E	Ra/Ra_{cr}	Pr	Pm_i	χ_m	σ_m	a	f_{dip}	SD_{dip}	Rm^*	Ro	Ro_ℓ	Λ	Λ_ℓ	Z
358	0.20	2	0.0	1.0E-4	23.0	1.0	2.0	0.90	0.50	9	1.16E-1	8.61E-2	241	1.66E-2	6.91E-2	0.525	0.022	0.10
359	0.20	2	0.0	1.0E-4	23.0	1.0	2.0	0.95	0.50	9	7.50E-1	3.53E-2	238	1.46E-2	6.45E-2	2.008	0.086	0.04
360	0.20	2	1.0	1.0E-4	5.2	1.0	2.0	0.90	0.50	9	8.36E-1	3.68E-2	110	8.35E-3	4.60E-2	2.103	0.146	0.04
361	0.20	2	1.0	1.0E-4	5.2	1.0	2.0	0.90	0.50	9	1.01E-1	9.06E-2	130	9.49E-3	5.28E-2	0.358	0.025	0.05
362	0.20	2	3.0	1.0E-4	3.2	1.0	2.0	0.80	0.50	9	1.08E-1	9.02E-2	89	1.40E-2	9.62E-2	0.198	0.020	0.23
363	0.20	2	3.0	1.0E-4	4.3	1.0	2.0	0.80	0.50	9	7.52E-2	7.68E-2	136	1.98E-2	1.38E-1	0.629	0.050	0.19
364	0.20	2	0.0	1.0E-5	12.1	1.0	1.0	0.80	0.50	9	8.42E-1	2.41E-2	141	2.53E-3	2.30E-2	0.948	0.042	0.03
365	0.20	1	0.0	1.0E-3	4.0	1.0	10.0	1.00	–	–	8.91E-3	8.01E-3	182	1.83E-2	2.02E-2	2.341	0.064	0.15
366	0.20	1	0.0	1.0E-3	7.9	1.0	10.0	1.00	–	–	1.14E-2	1.61E-2	385	3.87E-2	6.50E-2	0.425	0.011	0.28
367	0.20	1	0.0	1.0E-3	9.2	1.0	10.0	1.00	–	–	2.00E-2	1.57E-2	418	4.48E-2	7.52E-2	1.592	0.039	0.29
368	0.20	1	0.0	1.0E-3	10.6	1.0	10.0	1.00	–	–	1.59E-2	1.80E-2	435	4.70E-2	9.09E-2	5.673	0.126	0.16
369	0.20	1	0.0	1.0E-3	19.8	1.0	10.0	1.00	–	–	2.30E-2	2.43E-2	733	7.36E-2	1.56E-1	19.736	0.337	0.08
370	0.20	1	0.0	1.0E-3	26.4	1.0	10.0	1.00	–	–	1.93E-2	2.21E-2	885	8.89E-2	1.91E-1	27.421	0.408	0.07
371	0.30	1	0.0	1.0E-3	3.7	1.0	10.0	1.00	–	–	5.10E-4	1.21E-3	180	1.81E-2	2.80E-2	2.668	0.088	0.11
372	0.30	1	0.0	1.0E-3	6.8	1.0	10.0	1.00	–	–	2.71E-3	4.03E-3	369	3.70E-2	7.83E-2	0.352	0.011	0.28
373	0.30	1	0.0	1.0E-3	8.5	1.0	10.0	1.00	–	–	6.93E-3	6.91E-3	446	4.48E-2	1.06E-1	5.654	0.160	0.15
374	0.30	1	0.0	1.0E-3	11.9	1.0	10.0	1.00	–	–	1.43E-2	1.42E-2	584	5.86E-2	1.49E-1	12.848	0.300	0.09
375	0.35	1	0.0	1.0E-3	4.7	1.0	10.0	1.00	–	–	7.09E-1	7.78E-2	200	2.02E-2	4.58E-2	13.794	0.540	0.07
376	0.35	1	0.0	1.0E-3	7.5	1.0	10.0	1.00	–	–	2.92E-2	3.70E-2	426	4.29E-2	1.08E-1	3.493	0.114	0.22
377	0.45	1	0.0	1.0E-3	3.3	1.0	10.0	1.00	–	–	7.76E-1	7.56E-2	122	1.24E-2	3.52E-2	15.625	1.082	0.08
378	0.45	1	0.0	1.0E-3	4.4	1.0	10.0	1.00	–	–	6.70E-1	1.07E-1	180	1.82E-2	5.68E-2	18.932	1.042	0.08
379	0.45	1	0.0	1.0E-3	5.0	1.0	10.0	1.00	–	–	5.31E-1	7.79E-2	221	2.23E-2	6.95E-2	21.909	0.968	0.06
380	0.45	1	0.0	1.0E-3	5.3	1.0	10.0	1.00	–	–	4.91E-1	6.53E-2	243	2.44E-2	7.86E-2	19.876	0.863	0.06
381	0.45	1	0.0	1.0E-3	5.5	1.0	10.0	1.00	–	–	6.56E-3	8.97E-3	315	3.17E-2	1.04E-1	1.405	0.072	0.22
382	0.45	1	0.0	1.0E-3	6.6	1.0	10.0	1.00	–	–	6.73E-3	9.04E-3	404	4.05E-2	1.31E-1	3.611	0.151	0.16
383	0.55	1	0.0	1.0E-3	2.0	1.0	10.0	1.00	–	–	9.14E-1	1.24E-2	91	9.11E-3	4.10E-2	1.553	0.244	0.02
384	0.55	1	0.0	1.0E-3	2.8	1.0	10.0	1.00	–	–	6.26E-1	5.31E-2	109	1.09E-2	3.91E-2	16.637	1.378	0.04
385	0.55	1	0.0	1.0E-3	3.8	1.0	10.0	1.00	–	–	6.04E-1	4.01E-2	165	1.66E-2	6.78E-2	16.599	1.136	0.04

Continued on next page

Model	η	BC	N_ρ	E	Ra/Ra_{cr}	Pr	Pm_i	χ_m	σ_m	a	f_{dip}	SD_{dip}	Rm^*	Ro	Ro_ℓ	Λ	Λ_ℓ	Z
386	0.55	1	0.0	1.0E-3	4.3	1.0	10.0	1.00	–	–	5.23E-1	4.93E-2	197	1.98E-2	8.24E-2	17.758	1.097	0.04
387	0.55	1	0.0	1.0E-3	4.5	1.0	10.0	1.00	–	–	4.27E-1	3.56E-2	216	2.17E-2	9.18E-2	18.249	1.078	0.04
388	0.55	1	0.0	1.0E-3	4.8	1.0	10.0	1.00	–	–	4.18E-1	5.94E-2	234	2.34E-2	9.93E-2	19.106	1.068	0.04
389	0.55	1	0.0	1.0E-3	5.0	1.0	10.0	1.00	–	–	3.98E-1	5.53E-2	256	2.57E-2	1.12E-1	18.007	0.989	0.03
390	0.55	1	0.0	1.0E-3	5.3	1.0	10.0	1.00	–	–	3.69E-1	6.42E-2	276	2.77E-2	1.22E-1	18.533	0.982	0.03
391	0.55	1	0.0	1.0E-3	5.3	1.0	10.0	1.00	–	–	3.54E-3	3.93E-3	332	3.33E-2	1.43E-1	2.420	0.149	0.13
392	0.55	1	0.0	1.0E-3	5.8	1.0	10.0	1.00	–	–	4.56E-3	5.59E-3	372	3.73E-2	1.60E-1	3.846	0.218	0.11
393	0.55	1	0.0	1.0E-3	6.3	1.0	10.0	1.00	–	–	2.63E-2	2.67E-2	407	4.08E-2	1.74E-1	5.146	0.272	0.10
394	0.55	1	0.0	1.0E-3	7.5	1.0	10.0	1.00	–	–	6.26E-3	6.38E-3	484	4.86E-2	2.11E-1	9.118	0.427	0.06
395	0.70	1	0.0	1.0E-3	1.8	1.0	10.0	1.00	–	–	7.65E-1	5.12E-2	68	6.82E-3	4.59E-2	4.336	0.971	0.02
396	0.70	1	0.0	1.0E-3	2.2	1.0	10.0	1.00	–	–	7.08E-1	4.80E-2	84	8.47E-3	5.34E-2	7.972	1.401	0.03
397	0.70	1	0.0	1.0E-3	2.6	1.0	10.0	1.00	–	–	6.69E-1	2.56E-2	111	1.12E-2	7.09E-2	11.006	1.520	0.03
398	0.70	1	0.0	1.0E-3	2.9	1.0	10.0	1.00	–	–	4.86E-1	3.41E-2	135	1.36E-2	9.27E-2	10.342	1.273	0.02
399	0.70	1	0.0	1.0E-3	2.9	1.0	10.0	1.00	–	–	1.67E-2	2.11E-2	149	1.50E-2	1.15E-1	0.034	0.006	0.14
400	0.70	1	0.0	1.0E-3	3.2	1.0	10.0	1.00	–	–	4.01E-1	3.25E-2	172	1.73E-2	1.28E-1	8.296	1.015	0.01
401	0.70	1	0.0	1.0E-3	3.2	1.0	10.0	1.00	–	–	1.64E-5	2.80E-5	180	1.81E-2	1.40E-1	0.199	0.031	0.12
402	0.70	1	0.0	1.0E-3	3.7	1.0	10.0	1.00	–	–	1.36E-2	7.96E-3	228	2.29E-2	1.73E-1	0.564	0.078	0.11
403	0.70	1	0.0	1.0E-3	4.6	1.0	10.0	1.00	–	–	2.49E-3	2.17E-3	307	3.08E-2	2.19E-1	2.915	0.305	0.06
404	0.70	1	0.0	1.0E-3	6.2	1.0	10.0	1.00	–	–	1.93E-2	1.16E-2	413	4.14E-2	2.88E-1	8.199	0.641	0.03
405	0.70	1	0.0	1.0E-3	12.3	1.0	10.0	1.00	–	–	9.03E-3	5.49E-3	709	7.10E-2	5.06E-1	28.738	1.593	0.03

Bibliography

Atkinson, D. H., Ingersoll, A. P., Seiff, A., Aug. 1997. Deep winds on Jupiter as measured by the Galileo probe. Nature 388, 649–650.

Atkinson, D. H., Pollack, J. B., Seiff, A., Sep. 1998. The Galileo probe Doppler wind experiment: Measurement of the deep zonal winds on Jupiter. Journal of Geophysical Research 103, 22911–22928.

Aubert, J., Labrosse, S., Poitou, C., Dec. 2009. Modelling the palaeo-evolution of the geodynamo. Geophysical Journal International 179, 1414–1428.

Aurnou, J., Heimpel, M., Wicht, J., Sep. 2007. The effects of vigorous mixing in a convective model of zonal flow on the ice giants. Icarus 190, 110–126.

Bagenal, F., Dowling, T. E., McKinnon, W. B., 2004. Jupiter: the planet, satellites and magnetosphere.

Barthelmes, F., Jan. 2013. Definition of Functionals of the Geopotential and Their Calculation from Spherical Harmonic Models. Scientific Technical Report STR09/02.

Bassom, A. P., Kuzanyan, K. M., Sokoloff, D., Soward, A. M., Apr. 2005. Non-axisymmetric $\alpha^2\Omega$-dynamo waves in thin stellar shells. Geophysical and Astrophysical Fluid Dynamics 99, 309–336.

Braginsky, S. I., Roberts, P. H., 1995. Equations governing convection in earth's core and the geodynamo. Geophysical and Astrophysical Fluid Dynamics 79, 1–97.

Brown, B. P., Browning, M. K., Brun, A. S., Miesch, M. S., Toomre, J., Mar. 2010. Persistent Magnetic Wreaths in a Rapidly Rotating Sun. The Astrophysical Journal 711, 424–438.

Browning, M. K., Apr. 2008. Simulations of Dynamo Action in Fully Convective Stars. The Astrophysical Journal 676, 1262–1280.

Burke, B. F., Franklin, K. L., Jun. 1955. Observations of a Variable Radio Source Associated with the Planet Jupiter. Journal of Geophysical Research 60, 213–217.

Burton, M. E., Dougherty, M. K., Russell, C. T., Dec. 2010. Saturn's internal planetary magnetic field. Geophysical Research Letters 37, 24105.

Busse, F. H., Apr. 2002. Convective flows in rapidly rotating spheres and their dynamo action. Physics of Fluids 14, 1301–1314.

Busse, F. H., Simitev, R. D., Oct. 2006. Parameter dependences of convection-driven dynamos in rotating spherical fluid shells. Geophysical and Astrophysical Fluid Dynamics 100, 341–361.

Caillabet, L., Mazevet, S., Loubeyre, P., Mar. 2011. Multiphase equation of state of hydrogen from ab initio calculations in the range 0.2 to 5 g/cc up to 10 eV. Physical Review B 83 (9), 094101.

Cao, H., Russell, C. T., Wicht, J., Christensen, U. R., Dougherty, M. K., Sep. 2012. Saturn's high degree magnetic moments: Evidence for a unique planetary dynamo. Icarus 221, 388–394.

Chabrier, G., Saumon, D., Hubbard, W. B., Lunine, J. I., Jun. 1992. The molecular-metallic transition of hydrogen and the structure of Jupiter and Saturn. The Astrophysical Journal 391, 817–826.

Cho, J. Y.-K., Polvani, L. M., Jul. 1996. The Morphogenesis of Bands and Zonal Winds in the Atmospheres on the Giant Outer Planets. Science 273, 335–337.

Choi, D. S., Showman, A. P., Brown, R. H., Apr. 2009. Cloud features and zonal wind measurements of Saturn's atmosphere as observed by Cassini/VIMS. Journal of Geophysical Research (Planets) 114, 4007.

Christensen, U., Olson, P., Glatzmaier, G. A., Aug. 1999. Numerical modelling of the geodynamo: a systematic parameter study. Geophysical Journal International 138, 393–409.

Christensen, U. R., Nov. 2002. Zonal flow driven by strongly supercritical convection in rotating spherical shells. Journal of Fluid Mechanics 470, 115–133.

Christensen, U. R., May 2010. Dynamo Scaling Laws and Applications to the Planets. Space Science Reviews 152, 565–590.

Christensen, U. R., Aubert, J., Jul. 2006. Scaling properties of convection-driven dynamos in rotating spherical shells and application to planetary magnetic fields. Geophysical Journal International 166, 97–114.

Christensen, U. R., Schmitt, D., Rempel, M., Apr. 2009. Planetary Dynamos from a Solar Perspective. Space Science Reviews 144, 105–126.

Christensen, U. R., Wicht, J., Jul. 2008. Models of magnetic field generation in partly stable planetary cores: Applications to Mercury and Saturn. Icarus 196, 16–34.

Connerney, J. E. P., 1992. Doing more with Jupiter's magnetic field. In: Planetary Radio Emissions III. p. 13.

Dobler, W., Stix, M., Brandenburg, A., Feb. 2006. Magnetic Field Generation in Fully Convective Rotating Spheres. The Astrophysical Journal 638, 336–347.

Duarte, L. D. V., Gastine, T., Wicht, J., Sep. 2013. Anelastic dynamo models with variable electrical conductivity: An application to gas giants. Physics of the Earth and Planetary Interiors 222, 22–34.

Dziewonski, A. M., Anderson, D. L., Jun. 1981. Preliminary reference Earth model. Physics of the Earth and Planetary Interiors 25, 297–356.

Evonuk, M., Glatzmaier, G. A., May 2007. Modeling convection and zonal winds in giant planets. In: IAU Symposium. Vol. 239 of IAU Symposium. pp. 177–187.

Fortney, J. J., Baraffe, I., Militzer, B., 2010. Giant Planet Interior Structure and Thermal Evolution. pp. 397–418.

Fortney, J. J., Hubbard, W. B., Jul. 2003. Phase separation in giant planets: inhomogeneous evolution of Saturn. Icarus 164, 228–243.

Fortney, J. J., Hubbard, W. B., Jun. 2004. Effects of Helium Phase Separation on the Evolution of Giant Planets. In: The Search for Other Worlds. Vol. 713 of American Institute of Physics Conference Series. pp. 197–200.

Fortney, J. J., Nettelmann, N., May 2010. The Interior Structure, Composition, and Evolution of Giant Planets. Space Science Reviews 152, 423–447.

French, M., Becker, A., Lorenzen, W., Nettelmann, N., Bethkenhagen, M., Wicht, J., Redmer, R., Sep. 2012. Ab Initio Simulations for Material Properties along the Jupiter Adiabat. The Astrophysical Journal Supplement 202, 5.

Gastine, T., Duarte, L., Wicht, J., Oct. 2012. Dipolar versus multipolar dynamos: the influence of the background density stratification. Astronomy and Astrophysics 546, A19.

Gastine, T., Wicht, J., May 2012. Effects of compressibility on driving zonal flow in gas giants. Icarus 219, 428–442.

Gilman, P. A., Glatzmaier, G. A., Feb. 1981. Compressible convection in a rotating spherical shell. I - Anelastic equations. II - A linear anelastic model. III - Analytic model for compressible vorticity waves. The Astrophysical Journal Supplement 45, 335–388.

Glatzmaier, G. A., Aug. 2008. A note on “Constraints on deep-seated zonal winds inside Jupiter and Saturn”. Icarus 196, 665–666.

Gómez-Pérez, N., Heimpel, M., Wicht, J., Jul. 2010. Effects of a radially varying electrical conductivity on 3D numerical dynamos. Physics of the Earth and Planetary Interiors 181, 42–53.

Goudard, L., Dormy, E., Sep. 2008. Relations between the dynamo region geometry and the magnetic behavior of stars and planets. Europhysics Letters 83, 59001.

Guillot, T., Oct. 1999. Interior of Giant Planets Inside and Outside the Solar System. Science 286, 72–77.

Guillot, T., Jan. 2005. THE INTERIORS OF GIANT PLANETS: Models and Outstanding Questions. Annual Review of Earth and Planetary Sciences 33, 493–530.

Hammel, H. B., Rages, K., Lockwood, G. W., Karkoschka, E., de Pater, I., Oct. 2001. New Measurements of the Winds of Uranus. Icarus 153, 229–235.

Heimpel, M., Gómez-Pérez, N., Jul. 2011. On the relationship between zonal jets and dynamo action in giant planets. Geophysical Research Letters 38, 14201.

Heimpel, M. H., Aurnou, J. M., Al-Shamali, F. M., Gomez Perez, N., Jul. 2005. A numerical study of dynamo action as a function of spherical shell geometry. Earth and Planetary Science Letters 236, 542–557.

Helled, R., Guillot, T., Apr. 2013. Interior Models of Saturn: Including the Uncertainties in Shape and Rotation. The Astrophysical Journal 767, 113.

Hess, S. L. G., Bonfond, B., Zarka, P., Grodent, D., May 2011. Model of the Jovian magnetic field topology constrained by the Io auroral emissions. Journal of Geophysical Research (Space Physics) 116, 5217.

Holme, R., Bloxham, J., 1996. The magnetic fields of Uranus and Neptune: Methods and models. Journal of Geophysical Research 101, 2177–2200.

Hubbard, W. B., Macfarlane, J. J., Jan. 1980. Structure and evolution of Uranus and Neptune. Journal of Geophysical Research 85, 225–234.

Hubbard, W. B., Podolak, M., Stevenson, D. J., 1995. The interior of Neptune. In: Neptune and Triton. pp. 109–138.

Ingersoll, A. P., Cuzzi, J. N., Sep. 1969. Dynamics of Jupiter's cloud bands. Journal of Atmospheric Sciences 26, 981–985.

Jones, C., 2003. Dynamos in planets. In: Stellar Astrophysical Fluid Dynamics. pp. 159–176.

Jones, C. A., Boronski, P., Brun, A. S., Glatzmaier, G. A., Gastine, T., Miesch, M. S., Wicht, J., Nov. 2011. Anelastic convection-driven dynamo benchmarks. Icarus 216, 120–135.

Jones, C. A., Kuzanyan, K. M., Nov. 2009. Compressible convection in the deep atmospheres of giant planets. Icarus 204, 227–238.

Jones, C. A., Kuzanyan, K. M., Mitchell, R. H., Aug. 2009. Linear theory of compressible convection in rapidly rotating spherical shells, using the anelastic approximation. Journal of Fluid Mechanics 634, 291.

Kaspi, Y., Flierl, G. R., 2007. Formation of Jets by Baroclinic Instability on Gas Planet Atmospheres. Journal of Atmospheric Sciences 64, 3177.

Kaspi, Y., Flierl, G. R., Showman, A. P., Aug. 2009. The deep wind structure of the giant planets: Results from an anelastic general circulation model. Icarus 202, 525–542.

Khurana, K. K., Kivelson, M. G., Vasyliunas, V. M., Krupp, N., Woch, J., Lagg, A., Mauk, B. H., Kurth, W. S., 2004. The configuration of Jupiter's magnetosphere. In: Jupiter. The Planet, Satellites and Magnetosphere. pp. 593–616.

Lantz, S. R., Fan, Y., Mar. 1999. Anelastic Magnetohydrodynamic Equations for Modeling Solar and Stellar Convection Zones. The Astrophysical Journal Supplement 121, 247–264.

Li, L., Ingersoll, A. P., Huang, X., Jan. 2006. Interaction of moist convection with zonal jets on Jupiter and Saturn. Icarus 180, 113–123.

Lian, Y., Showman, A. P., Apr. 2008. Deep jets on gas-giant planets. Icarus 194, 597–615.

Lian, Y., Showman, A. P., May 2010. Generation of equatorial jets by large-scale latent heating on the giant planets. Icarus 207, 373–393.

Limaye, S. S., Mar. 1986. Jupiter - New estimates of the mean zonal flow at the cloud level. Icarus 65, 335–352.

Liu, J., Goldreich, P. M., Stevenson, D. J., Aug. 2008. Constraints on deep-seated zonal winds inside Jupiter and Saturn. Icarus 196, 653–664.

Lorenzen, W., Holst, B., Redmer, R., Mar. 2009. Demixing of Hydrogen and Helium at Megabar Pressures. Physical Review Letters 102 (11), 115701.

Lorenzen, W., Holst, B., Redmer, R., Nov. 2010. First-order liquid-liquid phase transition in dense hydrogen. Physical Review B 82 (19), 195107.

Lorenzen, W., Holst, B., Redmer, R., Dec. 2011. Metallization in hydrogen-helium mixtures. Physical Review B 84 (23), 235109.

Lowes, F. J., Apr. 1966. Mean-square values on sphere of spherical harmonic vector fields. Journal of Geophysical Research 71, 2179–2179.

Lowes, F. J., Mar. 1974. Spatial power spectrum of the main geomagnetic field, and extrapolation to the core. Geophysical Journal International 36, 717–730.

Moffatt, H. K., 1978. Magnetic field generation in electrically conducting fluids. In: Cambridge, England, Cambridge University Press, 1978. 353 p.

Morales, M. A., Schwegler, E., Ceperley, D., Pierleoni, C., 2010. Evidence for a first-order liquid-liquid transition in high-pressure hydrogen from ab initio simulations. Proceedings of the National Academy of Science 107, 12799–12803.

Nettelmann, N., Becker, A., Holst, B., Redmer, R., May 2012. Jupiter Models with Improved Ab Initio Hydrogen Equation of State (H-REOS.2). The Astrophysical Journal 750, 52.

Nettelmann, N., Holst, B., Kietzmann, A., French, M., Redmer, R., Blaschke, D., Aug. 2008a. Ab Initio Equation of State Data for Hydrogen, Helium, and Water and the Internal Structure of Jupiter. The Astrophysical Journal 683, 1217–1228.

Nettelmann, N., Redmer, R., Blaschke, D., Dec. 2008b. Warm dense matter in giant planets and exoplanets. Physics of Particles and Nuclei 39, 1122–1127.

Olson, P., Aug. 2011. Laboratory Experiments on the Dynamics of the Core. Physics of the Earth and Planetary Interiors 187, 139–156.

Olson, P., Christensen, U., Glatzmaier, G. A., May 1999. Numerical modeling of the geodynamo: Mechanisms of field generation and equilibration. Journal of Geophysical Research 104, 10383–10404.

Parker, E. N., Sep. 1955. Hydromagnetic Dynamo Models. The Astrophysical Journal 122, 293.

Porco, C. C., West, R. A., McEwen, A., Del Genio, A. D., Ingersoll, A. P., Thomas, P., Squyres, S., Dones, L., Murray, C. D., Johnson, T. V., Burns, J. A., Brahic, A., Neukum, G., Veverka, J., Barbara, J. M., Denk, T., Evans, M., Ferrier, J. J., Geissler, P., Helfenstein, P., Roatsch, T., Throop, H., Tiscareno, M., Vasavada, A. R., Mar. 2003. Cassini Imaging of Jupiter's Atmosphere, Satellites, and Rings. Science 299, 1541–1547.

Redmer, R., Mattsson, T. R., Nettelmann, N., French, M., Jan. 2011. The phase diagram of water and the magnetic fields of Uranus and Neptune. Icarus 211, 798–803.

Ridley, V. A., Sep. 2013. Jovimagnetic secular variation. Doctoral thesis, submitted.

Roberts, P., 2007. How MHD Transformed the Theory of Geomagnetism. In: Magnetohydrodynamics: Historical Evolution and Trends. Springer, p. 3.

Rotvig, J., Jones, C., 2002. Rotating convection-driven dynamos at low ekman number. Phys Rev E Stat Nonlin Soft Matter Phys 66 (5 Pt 2), 056308.

Ruzmaikin, A. A., Sokolov, D. D., Starchenko, S. V., Mar. 1988. Excitation of non-axially symmetric modes of the sun's mean magnetic field. Solar Physics 115, 5–15.

Salpeter, E. E., Apr. 1973. On Convection and Gravitational Layering in Jupiter and in Stars of Low Mass. The Astrophysical Journal 181, L83.

Sánchez-Lavega, A., Hueso, R., Pérez-Hoyos, S., García-Melendo, E., Rojas, J. F., Sep. 2004. Observations and Models of the General Circulation of Jupiter and Saturn. Lecture Notes and Essays in Astrophysics 1, 63–86.

Sánchez-Lavega, A., n., Rojas, J. F., Sada, P. V., Oct. 2000. Saturn's Zonal Winds at Cloud Level. Icarus 147, 405–420.

Sasaki, Y., Takehiro, S.-I., Kuramoto, K., Hayashi, Y.-Y., Oct. 2011. Weak-field dynamo emerging in a rotating spherical shell with stress-free top and no-slip bottom boundaries. Physics of the Earth and Planetary Interiors 188, 203–213.

Schrinner, M., Petitdemange, L., Dormy, E., Jun. 2011. Oscillatory dynamos and their induction mechanisms. Astronomy and Astrophysics 530, A140.

Schrinner, M., Petitdemange, L., Dormy, E., Jun. 2012. Dipole Collapse and Dynamo Waves in Global Direct Numerical Simulations. The Astrophysical Journal 752, 121.

Schrinner, M., Rädler, K.-H., Schmitt, D., Rheinhardt, M., Christensen, U. R., Apr. 2007. Mean-field concept and direct numerical simulations of rotating magnetoconvection and the geodynamo. Geophysical and Astrophysical Fluid Dynamics 101, 81–116.

Showman, A. P., Gierasch, P. J., Lian, Y., Jun. 2006. Deep zonal winds can result from shallow driving in a giant-planet atmosphere. Icarus 182, 513–526.

Simitev, R. D., Busse, F. H., Jan. 2009. Bistability and hysteresis of dipolar dynamos generated by turbulent convection in rotating spherical shells. Europhysics Letters 85, 19001.

Simitev, R. D., Busse, F. H., Apr. 2012. How Far can Minimal Models Explain the Solar Cycle? The Astrophysical Journal 749, 9.

Soderlund, K. M., Heimpel, M. H., King, E. M., Aurnou, J. M., May 2013. Turbulent models of ice giant internal dynamics: Dynamos, heat transfer, and zonal flows. Icarus 224, 97–113.

Soderlund, K. M., King, E. M., Aurnou, J. M., Jun. 2012. The influence of magnetic fields in planetary dynamo models. Earth and Planetary Science Letters 333, 9–20.

Sreenivasan, B., Jones, C. A., Feb. 2006. The role of inertia in the evolution of spherical dynamos. Geophysical Journal International 164, 467–476.

Sreenivasan, B., Jones, C. A., Dec. 2011. Helicity generation and subcritical behaviour in rapidly rotating dynamos. Journal of Fluid Mechanics 688, 5–30.

Sromovsky, L. A., Limaye, S. S., Fry, P. M., Sep. 1993. Dynamics of Neptune's Major Cloud Features. Icarus 105, 110–141.

Stanley, S., Mar. 2010. A dynamo model for axisymmetrizing Saturn's magnetic field. Geophysical Research Letters 37, 5201.

Stanley, S., Bloxham, J., Mar. 2004. Convective-region geometry as the cause of Uranus' and Neptune's unusual magnetic fields. Nature 428, 151–153.

Stanley, S., Bloxham, J., Oct. 2006. Numerical dynamo models of Uranus' and Neptune's magnetic fields. Icarus 184, 556–572.

Stanley, S., Glatzmaier, G. A., May 2010. Dynamo Models for Planets Other Than Earth. Space Science Reviews 152, 617–649.

Stellmach, S., Hansen, U., Nov. 2004. Cartesian convection driven dynamos at low Ekman number. Physical Review E 70 (5), 056312.

Stevenson, D. J., May 1980. Saturn's luminosity and magnetism. Science 208, 746–748.

Stevenson, D. J., 1982. Reducing the non-axisymmetry of a planetary dynamo and an application to Saturn. Geophysical and Astrophysical Fluid Dynamics 21, 113–127.

Stevenson, D. J., Mar. 2003. Planetary magnetic fields. Earth and Planetary Science Letters 208, 1–11.

Stevenson, D. J., Salpeter, E. E., Oct. 1977a. The dynamics and helium distribution in hydrogen-helium fluid planets. The Astrophysical Journal Supplement 35, 239–261.

Stevenson, D. J., Salpeter, E. E., Oct. 1977b. The phase diagram and transport properties for hydrogen-helium fluid planets. The Astrophysical Journal Supplement 35, 221–237.

Vasavada, A. R., Showman, A. P., Aug. 2005. Jovian atmospheric dynamics: an update after Galileo and Cassini. Reports on Progress in Physics 68, 1935–1996.

Wicht, J., Christensen, U. R., 2007. Numerical dynamo simulations. Treatise on Geophysics – Elsevier 8.

Williams, G. P., Aug. 1978. Planetary circulations. I - Barotropic representation of Jovian and terrestrial turbulence. Journal of Atmospheric Sciences 35, 1399–1426.

Yadav, R. K., Gastine, T., Christensen, U. R., Jul. 2013a. Scaling laws in spherical shell dynamos with free-slip boundaries. Icarus 225, 185–193.

Yadav, R. K., Gastine, T., Christensen, U. R., Duarte, L. D. V., Sep. 2013b. Consistent Scaling Laws in Anelastic Spherical Shell Dynamos. The Astrophysical Journal 774, 6.

Yoshimura, H., Nov. 1975. Solar-cycle dynamo wave propagation. The Astrophysical Journal 201, 740–748.

Yu, Z. J., Leinweber, H. K., Russell, C. T., Mar. 2010. Galileo constraints on the secular variation of the Jovian magnetic field. Journal of Geophysical Research (Planets) 115, 3002.

Publications and Presentations

Publications

First author

- Duarte, L. D. V., Gastine, T., Wicht, J., 2012, Anelastic dynamo models with variable electrical conductivity: an application to gas giants. Physics of the Earth and Planetary Interiors 222, 22-34.

Co-author

- Gastine, T., Duarte, L., Wicht, J., 2012, Dipolar versus multipolar dynamos: the influence of the background density stratification. Astronomy & Astrophysics 546, A19.
- Gastine, T., Morin, J., Duarte, L., Reiners, A., Christensen, U. R., Wicht, J., 2013, What controls the magnetic geometry of M dwarfs? Astronomy & Astrophysics 549, L5.
- Morin, J., Gastine, T., Duarte, L., Reiners, A., Christensen, U. R., Wicht, J., 2012, Does inertia determine the magnetic geometry of low-mass stars? SF2A-2012, 415-418.
- Yadav, R. K., Gastine, T., Christensen U. R., Duarte, L. D. V., 2013, Consistent scaling laws in anelastic spherical shell dynamos. Astronomy & Astrophysics 774-779.

Presentations

- AGU Fall Meeting, "Magnetic Field Generation and Zonal Flows in the Gas Giants" (poster), 9–13th December 2013, San Francisco, USA
- Nordita workshop, Differential Rotation and Magnetism across the HR Diagram, "Anelastic dynamo models with variable electrical conductivity: an application to gas giants" (talk), 19thApril – 3rdMay 2013, Stockholm, Sweden
- IMPRS Seminar, "Anelastic dynamo models with variable electrical conductivity: an application to gas giants" (talk), 19th December 2012, Katlenburg-Lindau, Germany

- AGU Fall Meeting, "Anelastic dynamo models with radially varying conductivity applied to the gas giants" (poster), 3rd–7th December 2012, San Francisco, USA
- 3rd PlanetMag Meeting, "Dynamo models with radially varying conductivity: application to the gas giants" (talk), 24–25th September 2012, Rostock, Germany
- SEDI meeting 2012, "Anelastic dynamo models with radially varying conductivity, an application to the gas giants" (poster), 1st–6th July 2012, Leeds, United Kingdom
- IMPRS Seminar, "Towards more realistic dynamo models of the Gas Giants" (talk), 2nd March 2012, Katlenburg-Lindau, Germany
- AGU Fall Meeting, "Anelastic Dynamo Model with Radially Varying Conductivity - an Application to the Gas Giants" (talk), 5–9th December 2011, San Francisco, USA
- 2nd PlanetMag Meeting, "Anelastic Dynamo Models with Radially Varying Conductivity - an Application to the Gas Giants" (talk), 18th–21st October 2011, Wernigerode, Germany
- Dynamo iGdR meeting, "Anelastic dynamo models with radially varying conductivity - An application to the Gas Giants" (poster), 12–17th September 2011, Cargèse, France
- IMPRS Seminar, "Explaining the simplicity of Saturn's magnetic field" (talk), 2nd March 2011, Katlenburg-Lindau, Germany
- 1st PlanetMag Meeting, "Dynamics and Magnetic Field Generation in Saturn" (poster), 19th–21st January 2011, Tutzing, Germany

Acknowledgements

I am deeply grateful to Dr. Thomas Gastine for his help and guidance. His daily support and advises allowed me to learn greatly about my work. His constant willingness to help was what gave me the opportunity to evolve and work better and faster. He also taught me a lot about basic skills, such as optimizing my computational resources and visualization of data. For this, I also want to thank Rakesh Yadav. His advises and our discussions truly improved the quality and efficiency of my daily work. Our discussions were always interesting and fruitful.

I would like to thank Dr. Johannes Wicht, the supervisor of my PhD thesis at the MPS for his support throughout these years. His guidance was crucial in the last year, which increased my knowledge greatly and improved significantly my writing skills and the structure of both this thesis and the article. These skills will stay with me for the rest of my life and career.

I also want to thank Prof. Dr. Ulrich Christensen for giving me the opportunity of joining the MPS planetary dynamo group and working on the gas giants. I thank Prof. Dr. Karl-Heinz Glaßmeier for accepting me as his PhD student in TU Braunschweig and for his very constructive criticism during our TAC (Thesis Advisory Committee) meetings. I also thank him for his support and help whenever I contacted him. I thank Prof. Dr. Andreas Hördt as well for his kindness and for accepting to be a member of my PhD defense committee.

I want to give a caring thank you to all the friends I had the pleasure to meet during my PhD in Germany, Neda, Megha, Yeon Joo, Nagaraju, Latha, Navdeep, Jayant, Sanjiv, Li, Jie, Juan, Wieland, Domenico, Kumiko, Nafiseh, Chemeda, Oksana and Eugene. I want to thank also our tennis, swimming, rowing, skating, badminton and movie club mates that proportioned some of the best memories that I take from my time in Germany. I will not forget any of them. Thank you all for teaching me so much about other cultures, many things that became part of my daily life.

I would like to thank my family for the support and specially for the help in my adaptation in the beginning, when everything was new to me. My parents and my brother accompanied me at the start of this journey and helped me prepare for it. This PhD thesis is dedicated to them. I want to also thank our neighbour Edith Menke in my country which played an important part in my decision to move to this country to carry out my PhD studies.

Finally, I thankfully acknowledge the financial support from the Deutsche Forschungsgemeinschaft (DFG) of the Special Priority Program 1488 and the Max-Planck-Institut für Sonnensystemforschung (MPS) in Katlenburg-Lindau, Germany. I also thank the International Max Planck Research School (IMPRS) at the Universities of Braunschweig and Göttingen for granting me this PhD fellowship which allowed me to work in Germany

on this project. I am specially grateful to Dr. Dieter Schmitt, the coordinator of the IMPRS during most of my PhD time, for the opportunity and for the care and support to all students.

All the images for visualization of the data were obtained with Python, many of the subroutines developed by Thomas Gastine. The 3D rendering images shown in the cover and in the Summary were done with Paraview. The MHD simulations were carried out using the MagIC code by Johannes Wicht with the anelastic approximation implemented by Thomas Gastine. The majority of the computations was done in the GWDG computer facilities in Göttingen, in the Norddeutscher Verbund für Hoch- und Höchstleistungsrechnen (HLRN) in Hannover and in the Max-Planck-Institut für Sonnensystemforschung.

Curriculum Vitae

Personal Information

Address: Max-Planck-Str. 2, 37191 Katlenburg-Lindau, Germany
Tel. (work): [+49] 5556 979 452
Tel. (home): [+49] 5556 979 281
Email: duarte@mps.mpg.de
Nationality: Portuguese
Date of Birth: March 19th, 1982

Education

PhD

TITLE: Anelastic dynamo models – an application to gas giants

INSTITUTE: Max-Planck-Institut für Sonnensystemforschung, Katlenburg-Lindau, Germany

SCHOOL: Technische Universität Braunschweig, Braunschweig, Germany

DATE: February, 2010 – February, 2014

Master's Degree (Post-Bologna)

TITLE: Astronomy and Astrophysics

SCHOOL: Faculdade de Ciências of the Universidade de Lisboa, Lisbon, Portugal

DATE: August, 2007 – December, 2009

FINAL AVERAGED-GRADE: 16 (out of 20)

DISSERTATION: Development of a circulation model and its application to Venus atmosphere (grade: 18 out of 20)

College Degree (Pre-Bologna)

TITLE: Aerospace Engineering

SCHOOL: Instituto Superior Técnico of the Universidade Técnica de Lisboa, Lisbon, Portugal

DATE: August, 2000 – February, 2007

FINAL AVERAGED-GRADE: 13 (out of 20)

DISSERTATION: Development of a package for Mathematica 5.0 for basic Orbital Mechanics calculations (grade: 18 out of 20)

Secondary Education

Title: General Education of the 1^{st} Grouping
School: Escola Secundária de Viriato – Viseu, Portugal
Date: August, 1997 – August, 2000
Final Averaged-Grade: 17 (out of 20)
Access exams Grade: 18 (out of 20)

Skills

Languages

My native language is Portuguese. I speak Portuguese and English fluently.

In addition, I studied French between 1994 and 1997 in school and I took a course of Russian for one year (1996/1997).

Computing

During my PhD studies in the Max-Planck Institute for Solar System Research, I learned the programming language Fortran 77 and I became familiar with the OpenMP paralellization technique, already implemented in the code that I used (MagIC code, by Johannes Wicht). I also worked with Python for data analysis and visualization.

During my Master's Dregree (2007) in Astronomy and Astrophysics, I learned the object-oriented programming language Java. I used the following programs: DS9, Source Extractor, PEGASE and MatLab (dissertation).

During my Engineering Degree I learned the programming languages C, C++, MatLab and Mathematica (+GUIKit). I used more extensively the following technical programs: Ansys, Catia, SolidWorks, TecPlot.

In 1995, I attended an initiation course in Windows in CESAE, in Viseu, Portugal.

Additional skills

I studied for seven years in the Conservatory of Music in Viseu, Portugal, between 1989 and 1996. During six of these years, I studied piano as well.

I practised Swimming with coaching for thirteen years (1987-2000, federated for one year), Tennis for four years with coaching (1996-2000), Shotokan Karate for one semester till yellow belt (in 2000) and eight years of Yoga in the Sivananda Yoga Centre in Lisbon (2001-2009).